2017

Effect of Surface Oxidation on the Mechanics of Carbon Nanotube Laden Interfaces

William Daniel Ivancic

EFFECT OF SURFACE OXIDATION ON THE MECHANICS OF CARBON NANOTUBE LADEN INTERFACES

WILLIAM DANIEL IVANCIC

Bachelor of Science in Chemical Engineering

Cleveland State University

May 2016

Submitted in Partial Fulfillment of Requirements for the Degree

MASTER OF SCIENCE IN CHEMICAL ENGINEERING

at the

CLEVELAND STATE UNIVERSITY

December 2017

We hereby approve this thesis for

William Daniel Ivancic

Candidate for the Master of Science in Chemical Engineering degree for the

Department of Chemical and Biomedical Engineering

and CLEVELAND STATE UNIVERSITY'S

College of Graduate Studies by

Thesis committee chairperson, Dr. Christopher Wirth
Department of Chemical and Biomedical Engineering
Cleveland State University

Date

Thesis committee member, Dr. Nolan Holland
Department of Chemical and Biomedical Engineering
Cleveland State University

Date

Thesis committee member, Dr. Jessica Bickel
Department of Physics
Cleveland State University

Date

Student's Date of Defense: December 8, 2017

EFFECT OF SURFACE OXIDATION ON THE MECHANICS OF CARBON NANOTUBE LADEN INTERFACES

WILLIAM DANIEL IVANCIC

ABSTRACT

Single and multi-walled carbon nanotubes (SWCNT & MWCNT) have been studied over the past three decades because of their excellent properties, including their mechanical strength and large electrical and thermal conductivities. Incorporating CNTs into phases necessary for use in consumer or industrial products has been challenging because of strong attractive interactions, heterogeneity, and lack of separation techniques for these nanomaterials. Moreover, there are further challenges incorporating CNTs into multiphase materials because of the many remaining open questions regarding the properties of an interface with CNTs adsorbed or nearby. In the present work, the mechanics and microstructure of a water/air interface laden with industrial grade MWCNTs was studied. Specifically, the properties of an interface laden with MWCNTs that were systematically modified via oxidation in nitric acid were measured. The duration of oxidation was varied, and the surface pressure of the nanotube laden interfaces was measured via a Langmuir-Blodgett trough and microbalance. The elasticity and film relaxation times for MWCNTs with varying extents of oxidation were measured and compared. Data suggests that film elasticity increased with increased surface oxidation. However, these measurements also revealed that elasticity increased with compression number, suggesting that surface oxidation may have had only an indirect effect on elasticity. Additionally, MWCNT films were observed with an optical microscope and SEM. Micrographs showed evidence of buckling in the films at low modification times. These data together suggest that the films

densify at higher modification times, pulling together due to capillary interactions brought on by stronger adsorption to the interface.

TABLE OF CONTENTS

LIST OF TABLES

LIST OF FIGURES

CHAPTER I

INTRODUCTION

Rising interest in the production of advanced materials has driven research in the field of colloidal and nanomaterials over the past few decades [1]. Creating films, foams, emulsions, and other multiphase materials with colloidal particles is an active area of research because these materials are regularly used in applications across many industries [2]. Generally, foams and emulsions are stabilized by surfactant, which is a small molecule having both hydrophilic "water-loving" and hydrophobic "water-hating" moieties. Although surfactant is a robust and regularly used molecule in consumer products and industrial processes, multiphase materials stabilized by surfactant often suffer from stability issues because of the dynamic adsorption/desorption process to/from an interface. As surfactant desorbs from an interface, multiphase materials, such as foams or emulsions, will ripen and destabilize. However, foams and emulsions stabilized by colloidal particles have been shown to possess much longer periods of stability than their surfactant stabilized counterparts [3, 4] because solid particles do not easily desorb from an interface.

Foams stabilized by silica nanoparticles were produced in my preliminary work by agitating vials filled with particles and a solution of ethanol and water (see **Fig. 1**). My

results showed that the interaction between particle chemistry and solution composition determines the wettability of the particle to the interface. In this case, the hydrophobic silica particles surround water droplets and prevent them from coalescence with other droplets at low ethanol concentration in the aqueous phase. As the ethanol concentration increased, the phase transitioned to a foam, as it became more favorable for the particles to pin at the interface between air and the aqueous phase. Finally, at high ethanol concentrations, the silica particles suspended in the solution, since the particles' affinity for the solution increased as the amount of water in the phase decreased.

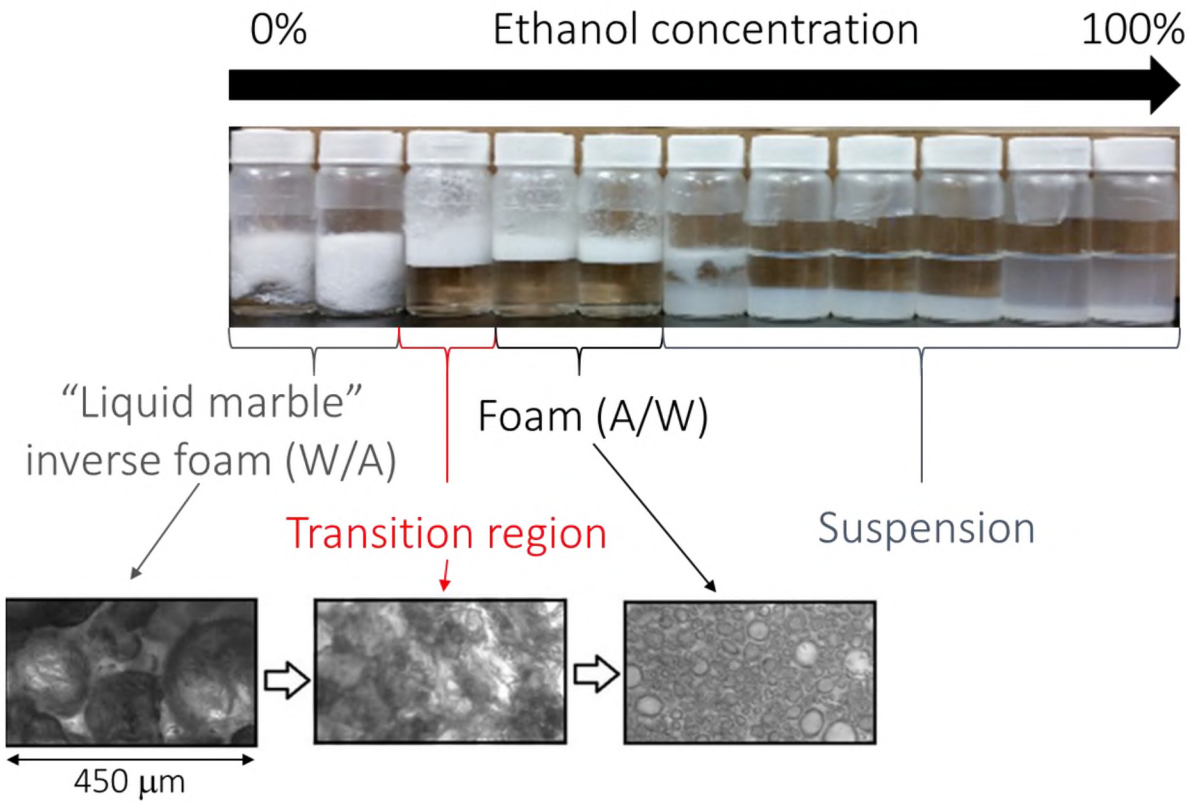

Figure 1: Silica particle stabilized multiphase materials. Ethanol and water mixtures with silica particles. Phase transition is evident from liquid marbles to foam to suspension both macroscopically (top) and microscopically (bottom).

The ease with which silica nanoparticle stabilized foams were produced is not necessarily repeated for other nanomaterials, such as industrial grade multi-walled carbon nanotubes. Carbon nanotubes are very small, extremely strong, thermally and electrically conductive particles [5]. They are shaped like hollow tubes with walls that are one atomic layer thick [5]. There are two broad families of carbon nanotubes (CNTs): single-walled carbon nanotubes (SWCNTs) and multi-walled carbon nanotubes (MWCNTs). SWCNTs are one individual tube of carbon molecules with diameters on the order of 1 nm [5]. MWCNTs are concentric cylinders of carbon molecules that vary in the number of layers of tubes. Their diameters range from 2 to 100 nm [5]. In addition, their lengths are much larger than their widths. Their properties would prove very useful in a macro-material, and they have been used as fillers for polymer composite materials for this reason [6]. Naively repeating the foaming steps for silica stabilized nanoparticle foams failed to produce foams stabilized by MWCNTs. In response to the need for creating multiphase materials stabilized by MWCNTs, the interfacial properties of an air/water interface laden with carbon nanotubes were studied.

The hypothesis driving the work described herein was: ***Surface oxidation of industrial grade MWCNT will alter the adsorption properties and resulting film elasticity of a MWCNT laden water/air interface.*** The work conducted to test this hypothesis sought to understand how CNTs adsorb to an interface and how these dynamics translate to the carbon nanotube microstructure at the air/water interface. Experiments were designed to monitor the difference between each sample once several samples of CNTs with varying degrees of oxidation had been produced. Interfacial properties like surface pressure and

elasticity were measured by spreading the samples onto an air and water interface in a Langmuir-Blodgett trough and probing the interface.

The main conclusions from this thesis were:

- Film buckling under the stress of compression is more prevalent in films comprised of CNTs with low modification times.
- As the duration of modification increases, the nanotubes adsorb to the interface more strongly, inducing capillary attractions between themselves.
- The CNT films become denser and stiffer with increasing modification due to the capillary interactions drawing them together.

CHAPTER II

LITERATURE REVIEW and THEORY

2.1 Colloidal particles at fluid/fluid interfaces

Colloidal particles vary in characteristic size from 0.01 μm to 10 μm. These particles are regularly found in consumer products, industrial processes, and advanced materials. Some examples of industries where colloidal particles play crucial roles are in the food, cosmetics, and petroleum industries. Food emulsions are often stabilized by protein [7] and emulsions in cosmetic products are often stabilized by colloidal particles [8]. Oil recovery is aided by the formation of ultra-stable Pickering emulsions using nanoparticles as the stabilizing agents [9]. Colloidal particles have often been integrated into multiphase materials that have fluid/fluid interfaces. For instance, emulsions (aqueous/oil) or foams (aqueous/air) regularly include some solid colloidal scale particles. These particles will often pin to an interface depending on the particle surface chemistry and the interface at which the particle finds itself [10]. Interfaces laden with colloidal particles may become more stable [3, 4]. This has led to further research into the mechanics of these particle laden interfaces and the multiphase materials produced with colloidal particles.

Multiphase materials like emulsions and foams require some stabilizing agent in them to prevent the collapse of the material due to lamellae or bubble coalescence. These materials are commonly stabilized by surface active agents (surfactants). Surfactants are molecules containing a hydrophilic head group and a hydrophobic tail group. The hydrophilic head group favors the water phase of the foam or emulsion, while the hydrophobic tail group favors the non-water phase [11]. These molecules will often adsorb and desorb to and from the interfaces in these emulsions and foams, moving into and out of the bulk fluid. As the emulsions or foams move toward equilibrium, the lamellae or bubbles coalesce until all of the phases separate [12].

Solid stabilized foams and emulsions, often called "Pickering" emulsions and foams are stabilized by the pinning of colloidal particles to interfaces in the material to prevent coalescence. The interfaces in Pickering emulsions and foams tend to be much more stable than their surfactant stabilized counterparts. Coalescence due to desorption of particles from the interface is mitigated because it is energetically favorable for particles with appropriate surface chemistries to pin at the interface. The surface chemistry of the particle affects the contact angle, a measure of wettability of the particles. It becomes more difficult to remove particles from the interface as they increase in size and as their contact angle approaches 90^{o} (see **Fig. 2**). Therefore, foams and emulsions stabilized by colloidal particles remain stable for long time scales, months to years long [3].

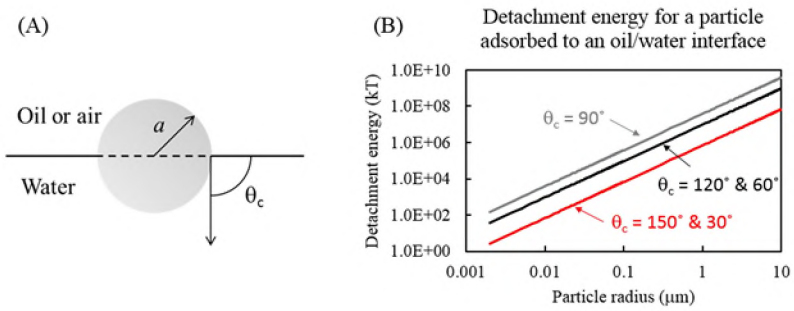

Figure 2: Reproduced from a proposal by Dr. Christopher Wirth. (A) is a colloidal particle pinned at an interface. (B) is a graph showing the energy required to detach a particle from an interface as a function of particle size and contract angle.

The wettability of a solid particle is central to determining whether or not the particles will pin to an interface. The contact angle is the angle, θ, made between the normal to the solid and liquid surfaces measured through the water [13] (see **Fig. 3**). For particles at an air and water interface, the contact angle can be visualized as follows:

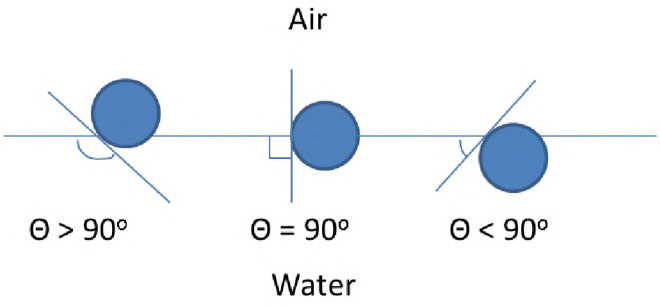

Figure 3: Schematic of particles at an interface with different contact angles. Left: Hydrophobic particle. Center: Particle of mixed hydrophobic and hydrophilic surface chemistry. Right: Hydrophilic particle.

The chemistry of the particles at the interface help determine the contact angle. For example, for a particle pinning at an air/water or oil/water interface, a hydrophobic particle will have a contact angle greater than 90^{o}, and will have a greater affinity for the air or oil phase, whereas a hydrophilic particle will have a contact angle less than 90^{o}, and a greater affinity for the water phase. A highly hydrophilic particle will tend to suspend in the aqueous phase, while a highly hydrophobic particle will tend to suspend in the oil phase (or sit on top of the interface for air). Thus, a particle with a very large ($>150^{o}$) or very small ($<30^{o}$) contact angle is unlikely to pin to the interface due to their strong affinities for their respective phases. However, a particle that has both hydrophilic and hydrophobic tendencies will have a contact angle closer to 90^{o}, increasing its likelihood to pin to the interface. Modifying the surface chemistry of a particle can therefor affect its ability to pin to an interface. Functionalization of particles by adding chemical groups to its surface is a common way to change the hydrophilic or hydrophobic tendencies of the particles, or even make them reactive [14].

In addition to surface chemistry, particle shape can also be tuned to achieve variation in particle adsorption properties. Anisotropic particles that pin to an interface will likely deform the interface, inducing aggregation of the particles. Particles pinned at an interface are drawn together by capillary interactions because the surface tries to minimize interfacial deformation [13]. Anisotropic particles create an excess in surface area when they deform the interfaces they pin to. In order to decrease that excess area, the particles are drawn to their closest neighbors, forming aggregates or assemblies [15]. This phenomena is often used to form special assemblies of anisotropic particles via self-assembly, like assemblies of colloidal cylinders or ellipsoids [15].

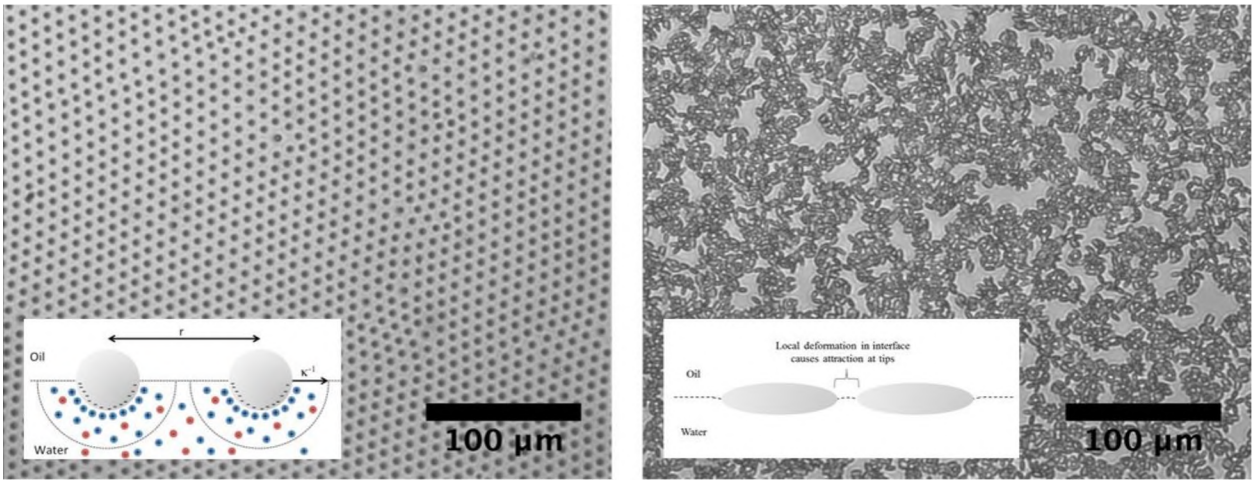

Figure 4: At left are colloidal spheres. No capillary attraction occurs between them. At right are ellipsoidal particles. Aggregation occurs here due to capillary interactions.

One example of an anisotropic particle is that of a carbon nanotube. As noted above, carbon nanotubes exhibit remarkable tensile strength and thermal and electrical conductivity properties [5, 16]. Implementing them in advanced material applications is a challenge however, due to the strong Van der Waals attractions these particles experience [17]. CNTs tend to flocculate because of these attractions, making it difficult to disperse them in liquids. In addition, CNTs are hydrophobic [18], adding an additional challenge to dispersing them in water. To combat flocculation and hydrophobicity, the surface chemistry can be altered by adding functional groups to the particle surface. Oxidation is a commonly used functionalization technique to modify CNTs because it adds polar groups to the surface, making the tubes more soluble in polar media [19]. Oxidation adds carboxylic groups to the surface of CNTs, adding some hydrophilic tendencies to the particles, and inducing electrostatic repulsion [20]. Although the dispersability of CNTs has been evaluated in the bulk for varying surface chemistries [21], little work has been

done identifying how these modifications impact the adsorption properties of CNTs to fluid/fluid interfaces. Further, as noted above, the surface chemistry of a particle will dramatically impact the adsorption energy of a solid particle to an interface.

2.2 Mechanics of interfacial films

A fluid-fluid interface is formed when two immiscible fluids meet. If this boundary remains clean, that is unpopulated by other molecules or particles, then the interface can be characterized by a single value for the surface tension at fixed temperature and pressure [22]. The surface tension of an interface is defined thermodynamically as the following [13]:

$$\sigma = (\partial F/\partial A)_{T,V,eq} \quad (1)$$

where σ is the surface tension, F is the Hemholtz Free Energy of the system, and A is the surface area. The subscript T, V, eq means that the system is at constant temperature and volume and that the system is in full internal equilibrium. One can physically understand the surface tension by picturing an interface. The figure below depicts an imaginary patch of a liquid surface, *ABCD*. The film exerts force on itself across the line *MM'*. If we consider the tension at the point *P* such that the line *MM'* passes through the point *P*, we can define the surface tension as the force along the line divided by the line's length.

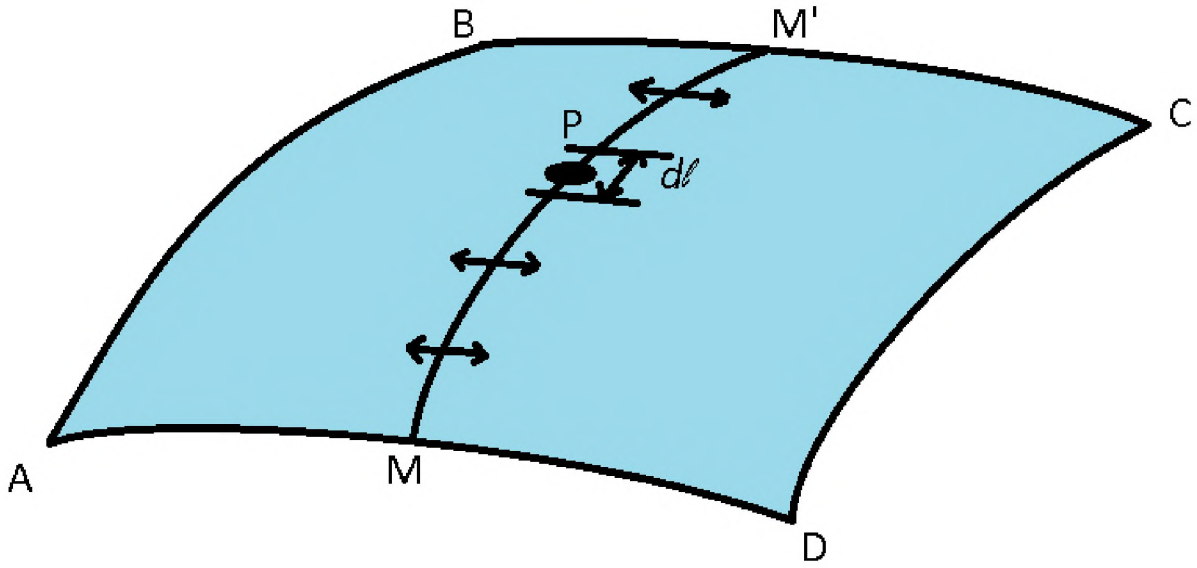

Figure 5: Example liquid surface *ABCD* is divided along the line *MM'* which passes through the point *P* [13].

We can define the surface tension by the following equation [13]:

$$\sigma = (dF/d\ell) \qquad (2)$$

where σ is the surface tension, F is the force across the line, and ℓ is the length of the line.

Once the interface becomes populated with molecules or particles that bridge the boundary between the two phases, the surface tension is not necessarily the value of the clean interface. Moreover, for certain systems, the value of the surface tension does not necessarily describe (in entirety) all the stresses at an interface [22]. In the 19th century, J.W. Gibbs showed that molecules and particles that pin to interfaces form microstructures that have a non-negligible effect on the interfacial properties due to the stresses they induce [23].

Investigating the relevant stresses of interfaces laden with particles can be accomplished by using the previously mentioned Langmuir-Blodgett trough. Langmuir-Blodgett troughs are devices that are used to measure interfacial properties. They are often used to assemble monolayers of anisotropic particles at interfaces, like nanorods, nanotubes, or nanosheets [24–26]. A liquid, usually water, is poured into the trough, with a surrounding gas, usually air, present. Onto the liquid surface, substances are placed between two movable barriers. The barriers can be closed to compress the film at the interface, thereby increasing the surface concentration of whatever substance is between the barriers. This device can be used to facilitate surface pressure measurements, particle depositions onto solid substrates, and scalable production of thin films [27]. Deposition of particles by the Langmuir-Blodgett technique onto a solid substrate is accomplished by dipping a substrate into the trough before placing particles at the interface, then withdrawing the substrate out through the particle laden interface [28]. The particles deposit onto the substrate as follows:

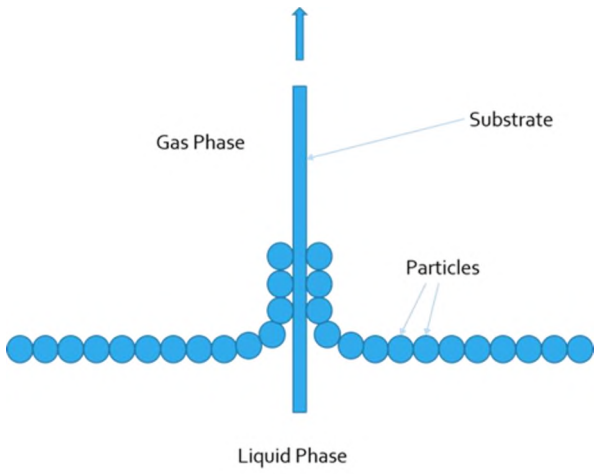

Figure 6: Schematic of a substrate being withdrawn from an interface with particles depositing onto it via the Langmuir method.

A Langmuir-Blodgett trough, a micro balance, and a Wilhelmy plate can be utilized for measuring surface pressure of a liquid/gas interface. The surface pressure is equal to the difference in surface tension between the "clean" interface, with no particles or molecules pinned there, and the "dirty" interface, laden with particles or molecules. It can be given by the following equation [29]:

$$\Pi = \sigma_0 - \sigma \tag{3}$$

where Π is the surface pressure, σ_0 is the surface tension of the "clean" interface, and σ is the surface tension of the "dirty" interface.

The Gibbs Elasticity is a measure of how well an interface can resist distortion. It is given by the equation [13]:

$$E_G = \frac{d\,\sigma}{d\ln(A)} \tag{4}$$

where E_G is the Gibbs Elasticity, σ is the surface tension, and A is the trough area. In experiments with a Langmuir-Blodgett trough and micro-balance, the surface pressure is recorded, not the surface tension. Decreases in the surface tension cause equivalent increases in the surface pressure. Therefore, the equation for Gibbs Elasticity can be rewritten in terms of surface pressure by replacing the change in the surface tension with the negative change in the surface pressure:

$$E_G = -\frac{d\,\Pi}{d\ln(A)} \tag{5}$$

where Π is the surface pressure as defined by equation (3).

The surface pressure of the interface is measured via the Langmuir-Blodgett trough in conjunction with a microbalance and Wilhelmy plate or rod. The surface pressure relates to the surface tension of the interface as prescribed in equation (3), wherein the surface pressure is equal to the difference between the surface tension of the clean interface and the surface tension of the interface laden with the foreign substance. When measuring surface pressure in this way, one must consider that the film will respond to the compressions. Changing the concentration of particles at the interface by compression affects the surface tension thermodynamically, but the physical compression affects the film mechanically. Therefore, the observed change in surface pressure due to a compression on a Langmuir-Blodgett trough is a combined effect of thermodynamics and microstructural stresses. In order to observe each part of this effect, stepwise compressions can be performed, allowing time for the film to relax after compressions. The initial spike in surface pressure during compression is a superposition of the microstructural and thermodynamic stresses, and comparing the new steady state surface pressure to the pre-compression surface pressure reveals the thermodynamic contribution (see **Fig.**7) [30, 31]. Surface pressure data plotted against the changing trough area yields graphs that can be used to determine the elasticity of the film, an important property for the stabilization of multiphase materials.

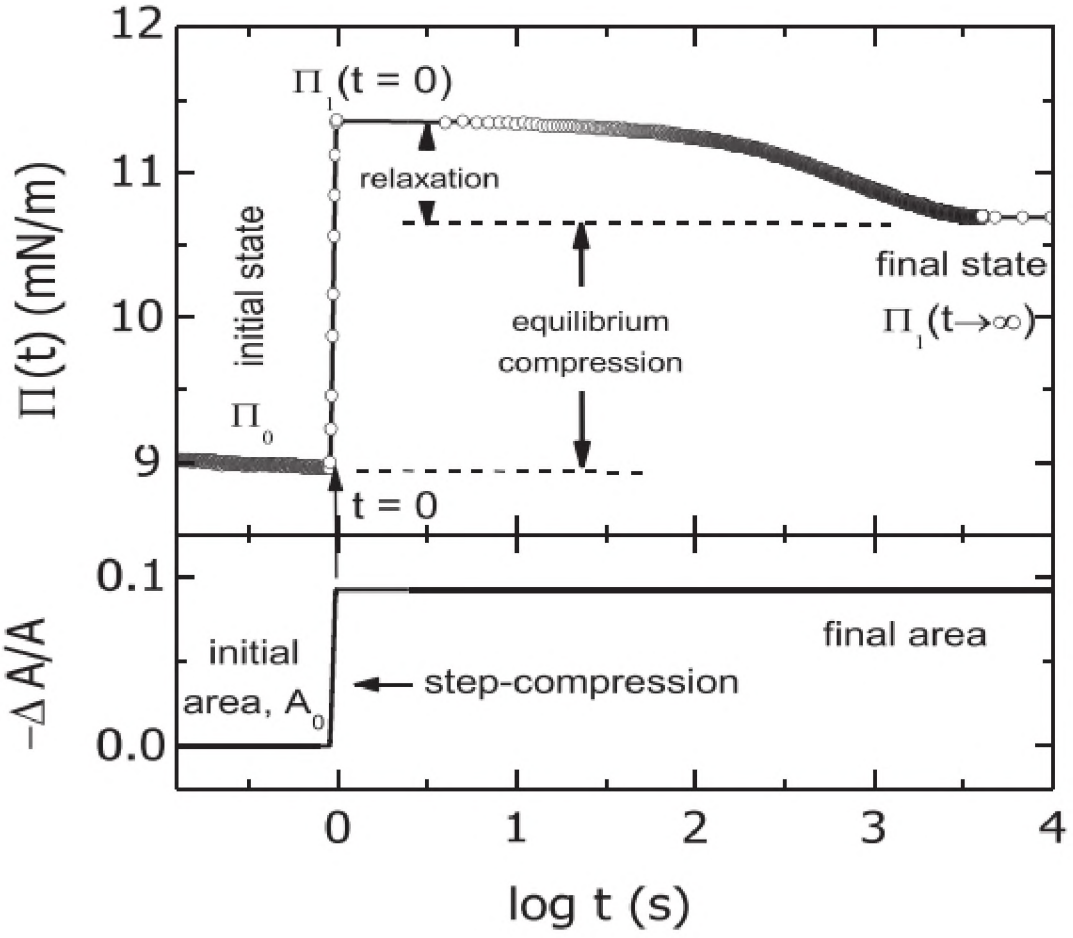

Figure 7: Mendoza, A. J., et al. "Particle Laden Fluid Interfaces: Dynamics and Interfacial Rheology" Advances in Colloid and Interface Science (2014). This figure represents a typical step compression experiment.

An example of work done on carbon based molecules at an interface is done by Diego Pradilla et al [32]. This work was to investigate the interfacial properties of Asphaltene molecules at an air/water and an water/oil interface [32]. Surface pressure isotherms were recorded by utilizing a Langmuir-Blodgett trough, and they were used to determine film

phase behavior and film elasticity. In addition, a technique called pendant drop analysis was used for surface tension measurement [32]. Using the data from their experiments, they were able to conclude that there was some aggregation occurring at both the air/water and water/oil interfaces. A work more closely associated with my own is that of Anson Ma et al [33]. This work investigates the difference between the behavior of carbon nanotubes that have been functionalized and carbon nanotubes with no functionalization at an air/water interface [33]. They found that aggregation was more prevalent in non-functionalized tubes, and that the functionalized CNTs formed aligned films under high compressions, resembling 3D liquid crystal structures [33]. My work builds upon this previous work by taking an in depth look into varying degrees of functionalization of industrial grade, multi-walled carbon nanotubes, and how these different tubes behave at an air/water interface. The film microstructures are observed with both optical microscopy and scanning electron microscopy to bolster recorded data with some physical meaning. Film elasticity is determined for all samples to understand the effect of varying degrees of oxidation on elasticity. Finally, a physical explanation of how the degrees of oxidation affect the films properties and microstructure, supported by the collected data, is given.

CHAPTER III

EXPERIMENTAL PROCEDURE AND INSTRUMENTATION

3.1 Procedure for preparation of CNT samples

Nitric acid is commonly used as an oxidative acid in the modification of carbon nanotubes [34]. This is usually performed to purify CNTs, exfoliate the tubes, or make them more soluble in water [19]. To study the effect of oxidation on the interfacial properties of MWCNTs from NanoLabs, samples of CNTs that had undergone oxidation for different durations had to be prepared. **Figures 8** and **9** show the experimental apparatus. A hot water bath was prepared at 60.0°C, monitored by a thermocouple in the bath. The bath was situated on a Fisher Scientific Isotemp hot plate with magnetic stir bar capabilities. A 250 mL double-necked round bottom flask was placed into the bath, and filled with ~200 mL of nitric acid. A glass condenser was fitted to the vertical neck of the flask, and supported by a clamp attached to a ring stand sitting next to the hot plate. A magnetic stir bar was added to the nitric acid through the angled neck of the flask, and the stirring mechanism was switched on.

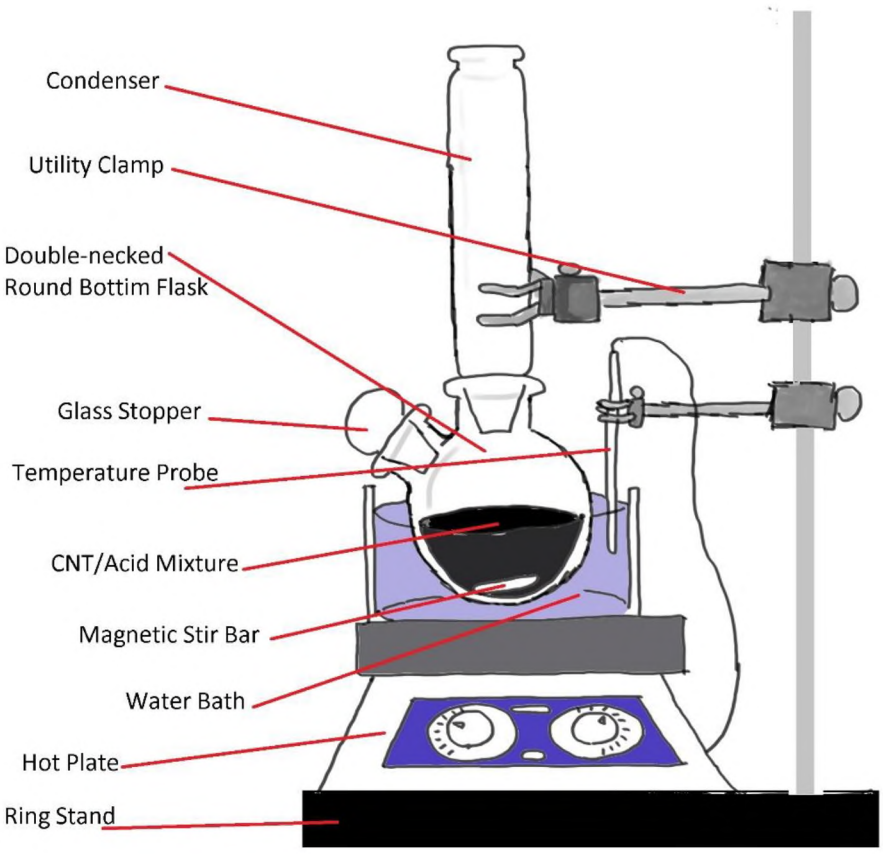

Figure 8: Schematic drawing of the apparatus used to modify MWCNTs via oxidation in nitric acid.

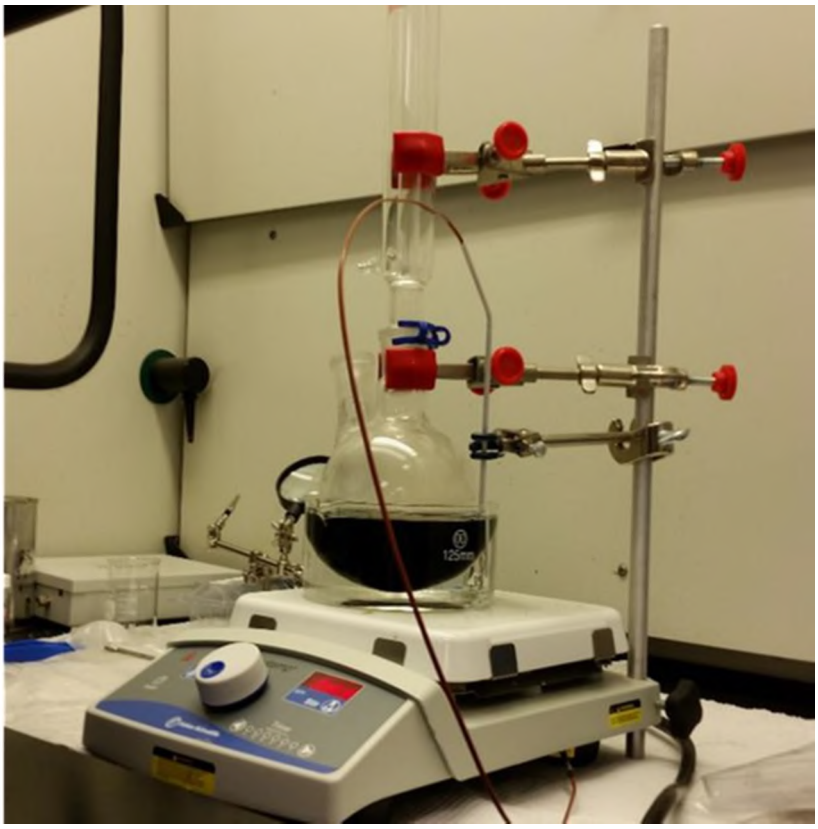

Figure 9: Photograph of the apparatus used to modify MWCNTs via oxidation in nitric acid.

1.0 grams of MWCNTs are added to the flask through the angled neck of the flask. A glass stopper then plugs the angled neck of the flask. Once the MWCNTs were added, a timer was started. After ~40 minutes, 1 hour, 2 hours, 4 hours, and 6 hours, ~20 mL of the nitric acid and CNT mixture was removed through the angled neck of the flask with a glass pipet, and delivered into a glass vacuum filter. Ultra-pure water was used to wash the CNTs in the filter, and remove excess nitric acid until a neutral pH was detected in the filter by Micro Essential Lab Hydrion pH paper. Ultra-pure (UP) water is filtered and purified with UV radiation by a Thermo Scientific MicroPure apparatus, until a resistivity

of 18.20 mΩ*cm is measured. The wet, oxidized nanotubes were placed into scintillation vials without caps to dry in the Fisher Scientific Isotemp oven.

Samples of between 0.099 and 0.113 wt% CNTs (see **Table 4** in Appendix A) in a 50 volume % isopropyl alcohol and 50 volume % ultra-pure water mixture were created by mixing equal volumes of IPA and UP water, then measuring out ~10 grams of the mixture into a scintillation vial, and adding ~0.01 grams of CNTs. After the components were all present in the vial, they were mixed via tip sonication with a Fisher Scientific Sonic Dismembrator for 5 minutes at 50% power. The vials were then capped and stored for later use. Before any sample was used, it was sonicated in a Fisher Scientific Ultrasonic Bath for ~2 minutes to break up any flocculation that may have occurred while it was not being used.

3.2 Procedure for measurement of surface pressure versus area

A NIMA Technology Langmuir-Blodgett Trough was utilized to measure the surface pressure at a CNT laden, water and air interface.

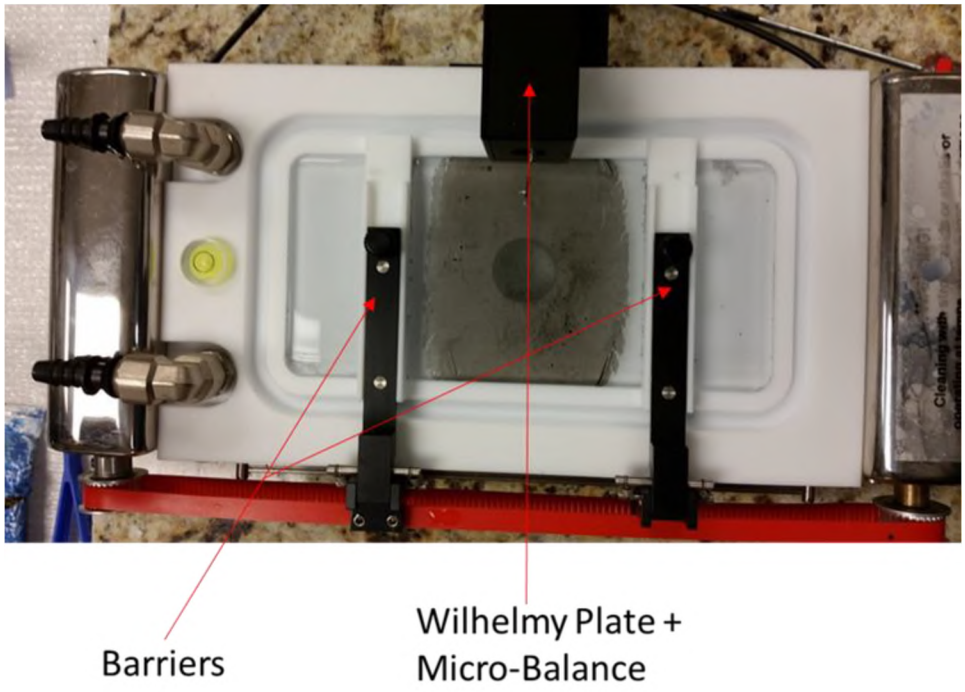

Figure 10: A NIMA Langmuir-Blodgett trough with a MWCNT laden interface. Reading the surface pressure is a microbalance and Platinum rod of diameter 0.020 inches.

After thorough washing of the trough and barriers with ethanol and acetone, and several rinses with ultra-pure water the trough was filled with 70.0 mL of UP water, and the barriers were coupled to the belt and placed at the interface such that the area between them was 75 cm^2. The NIMA software was booted up, and the micro-processor interface which connects the trough and sensors to the computer through serial cables was powered on. Attached to the processor is a microbalance used to measure the surface pressure via the Wilhelmy plate method. In lieu of a paper Wilhelmy plate, a 0.020-inch diameter platinum wire was utilized. The wire was lightly rinsed in ethanol, then fired with a Bunsen burner for 15 to 20 seconds. The clean wire was then hung from the

microbalance. Before lowering the wire into the clean water interface, the pressure reading on the computer screen was zeroed. To make sure the wire was properly cleaned, and that the interface is clean, the wire is then dipped into the water, and the pressure reading is checked against the tabulated value for surface tension of water at ambient temperature, between 71.20 and 72.75 mN/m [35]. If it reads a value close to the surface pressure of clean water at the ambient temperature, +/- 1 mN/m the reading is zeroed. If it is not, the trough is rinsed again, and the wire is washed and fired again until the surface pressure for clean water is with 1 mN/m of the accepted value. Keep in mind that the accepted value for the surface pressure of water in this case should be about -72 mN/m because the device is subtracting the surface tension of water from the zeroed surface tension measured before the platinum wire was dipped into the interface. Next, 300 μL of CNT in IPA and UP water suspension was placed dropwise at the interface between the barriers. Drops were placed in all different areas of the interface to ensure that the film was as uniform as possible. Data acquisition was initiated, and the barriers were compressed such that the area decreased at a rate of 7 cm^2/min. This is because the trough width is 7 cm, thus the barriers move laterally at a rate of 1 cm/min relative to one another. The barriers compress and expand at this speed for 3 cycles. The data recorded was the surface pressure as measured by the microbalance versus the change in trough area as recorded by the trough's barrier positions. Because the mechanical compressions of the barriers are not perfectly identical for each experiment, the total number of data points varies slightly from experiment to experiment.

3.3 Procedure for stepwise compressions

Stepwise compressions were performed to identify and separate contributions to the surface stress. Steady state surface pressures for each incremental change in trough area would show how the film responds thermodynamically to the increases in surface concentration. The sharp increases in surface pressure just after the compression ends indicates the film's response to the stress on compression. The new steady state surface pressure after compression and relaxation compared to the steady state surface pressure before compression yields the thermodynamic response of the interface. These responses give insight into the dynamics of the film in both stressed and relaxed states. The trough was set up the same way as previous experiments, but this time, after beginning data acquisition and spreading of CNTs on the interface, the barriers were compressed from 75 cm^2 to 70 cm^2, and allowed to relax for 30 minutes. After this relaxation, another compression increment of 5 cm^2 was performed with another thirty-minute relaxation period, and so on until a trough area of 25 cm^2 was reached and the final thirty minutes were allowed for relaxation. This procedure was performed for all samples of varying degree of oxidation.

The trough was set up in the same manner as the stepwise procedure to study the relaxation time for a total film relaxation, with the barriers at 75 cm^2 and CNTs spread on the interface. Once data acquisition was started, the barriers were closed to 70 cm^2. Then, the film was allowed to relax overnight.

3.4 Procedure for optical microscopy imaging

A custom, 3D printed trough with identical dimensions in terms of length, width, and depth as the NIMA trough, but designed to fit onto the optical microscope stage under the objectives was designed. After testing the trough to ensure it was water-tight, it was implemented to view the CNT laden air/water interface with an optical microscope. The trough was printed with a Makerbot 3D printer.

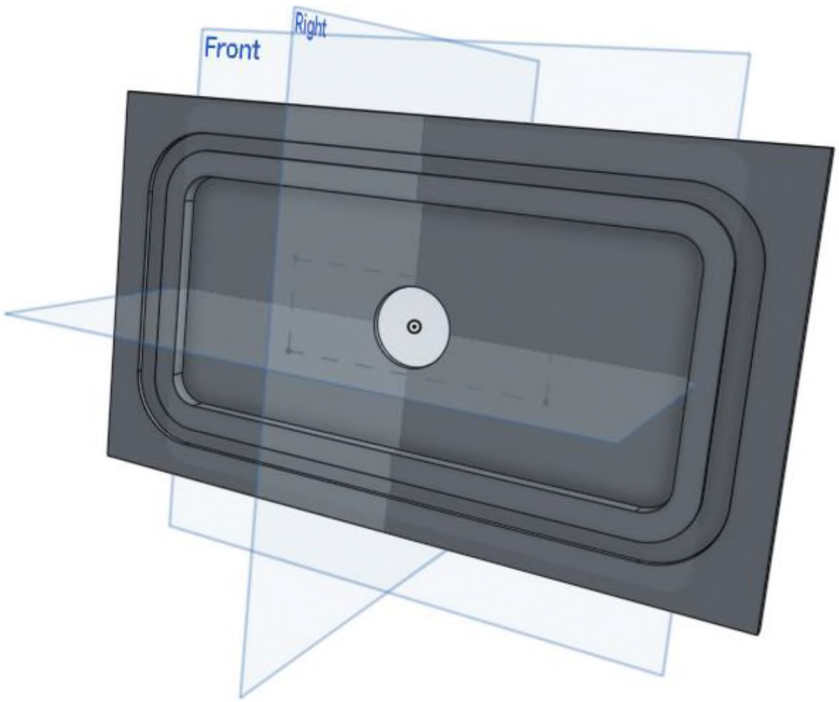

Figure 11: 3D CAD drawing of the printed trough using the online CAD program Onshape.

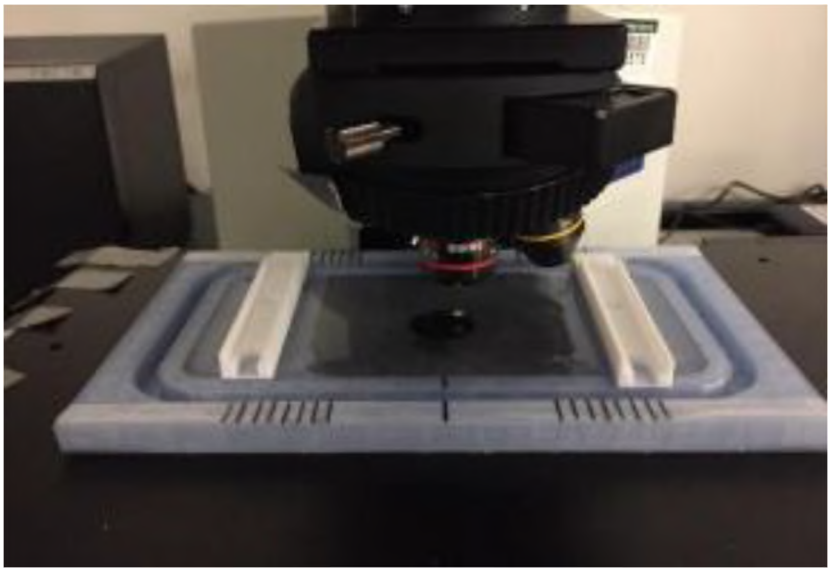

Figure 12: The 3D printed trough designed to fit into the microscope stage under the microscope objectives. The Teflon coated barriers used for film compression are borrowed from the NIMA trough.

Snapshots and videos were recorded using CellSense dimensions software in conjunction with an Olympus optical microscope and mounted Hamamatsu Orca R2 digital camera. The barriers from the NIMA tough were used with this trough to compress the interface. The barriers were moved by hand to marked locations on the trough corresponding to 5 cm^2 incremental changes in trough area. Snapshots were taken at each area from ~75 cm^2 to ~25 cm^2.

3.5 Procedure for SEM imaging

The films can be more closely observed via a Scanning Electron Microscope by depositing the CNT film from the air/water interface onto a silicon substrate from

University Wafer. First, the silicon wafer is dipped into the clean water surface on the Langmuir-Blodgett trough. Then, the CNTs are added to the interface. Finally, the barriers are compressed to desired trough areas, at which point the dipped substrate is withdrawn, and the trough is cleaned and reset. This is repeated until depositions have been done for each desired trough area. The substrates are then observed via the SEM to look closely at the microstructure.

3.6 Procedure for Electrophoretic Mobility measurement

Electrophoresis is the movement of particles suspended in a motionless liquid due to an imposed electric field [36]. This phenomenon can be observed using a device to apply an electric field and measure the velocity of particles moving in the liquid. This observed velocity is called the electrophoretic mobility. The presence of chemical groups on the nanotubes' surfaces can be confirmed by measuring electrophoretic mobility for the different modification times. The concentration of tubes has to be small for the Zetasizer to effectively measure electrophoretic mobility, so the ~0.1 wt% CNT mixtures were diluted into ~0.01 wt% mixtures by adding 1.0 grams of the ~0.1 wt% mixture to 9.0 grams of ~50 vol% isopropyl alcohol in water solution. The tip sonicator is used for 5 minutes at 50% amplitude just as it is used for making the ~0.1 wt% CNT mixtures. Next, the samples are placed in a centrifuge to pull out much of the tubes, leaving behind a translucent grey liquid comprised of isopropyl alcohol, water, and a very small concentration of CNTs. Using a 3 mL syringe, 1.0 mL of the liquid is pushed into a Malvern Zeta cell, and placed in the Zetasizer. Set up the Zetasizer program to measure zeta potential, and start the measurement. Export the data for electrophoretic mobility.

To ensure the presence of surface groups on the MWCNTs, electrophoresis was utilized to determine if the tubes of different modification times had varying electronegativity. With the use of a Malvern Zetasizer, the electrophoretic mobility for samples of each modification time was determined. A more negative mobility indicates a higher concentration of carboxyl groups present. Therefore, longer modification times should have more negative electrophoretic mobilities than shorter modification durations.

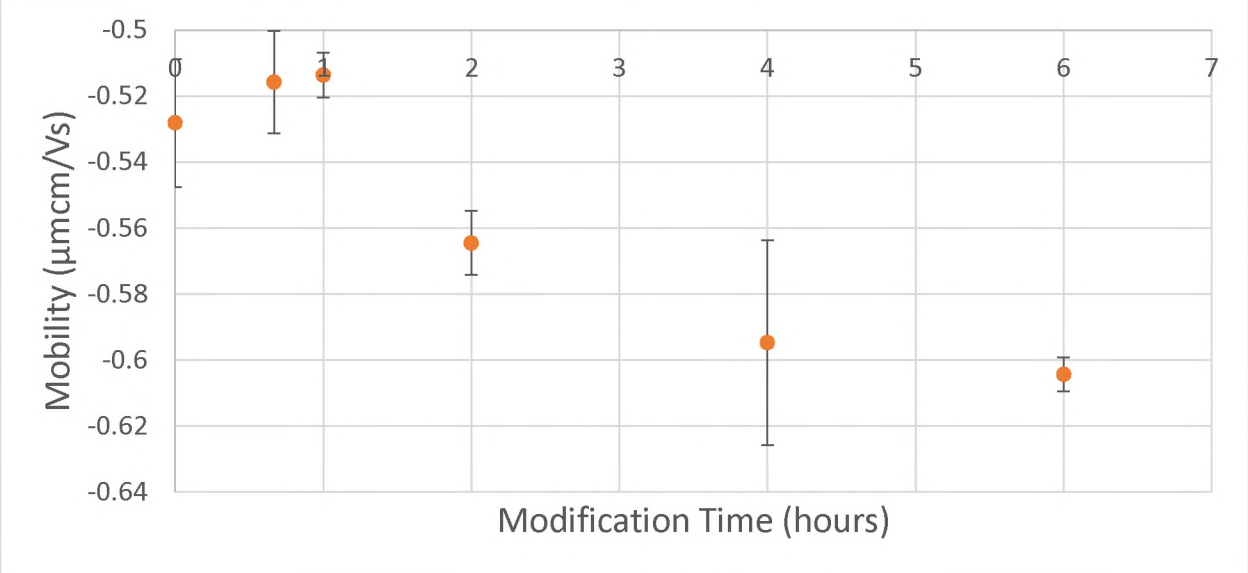

Figure 13: Electrophoretic ability of MWCNT samples plotted against those samples corresponding modification times.

Indeed, the trend for electrophoretic mobility is that the longer the tubes were modified for, the more negative their mobility was. This provides evidence that functional groups are present in varying degrees on the surfaces of the CNTs, corresponding to the modification times.

CHAPTER IV

RESULTS AND DISCUSSION

4.1 Introduction

This section contains the discussion of acquired data and results from the performed experiments. Once the multi-walled carbon nanotubes (MWCNTs) were oxidized for different durations and sorted accordingly, they were used for several experiments to compare how each sample responded to compression at an air/water interface. In addition, coarse particle size and structure, as well as microstructure of the films was observed through optical microscopy and scanning electron microscopy.

4.2 Imaging with Scanning Electron Microscopy

Initially, Scanning Electron Microscopy (SEM) was utilized to determine if surface oxidation had a significant effect on structure of individual MWCNT particles. MWCNT films were deposited onto silicon wafers by submerging the substrate into the air/water interface before placing particles at the interface. Then, withdrawing the substrate from the interface after the film had been compressed to a desired area (see **Fig. 6**). Two films were deposited for each sample; one at the smallest area considered for these experiments, 25

cm^2, and the other near the critical areas, defined later, for the specific films, $35cm^2$ for any modified tubes, and 40 cm^2 for unmodified tubes.

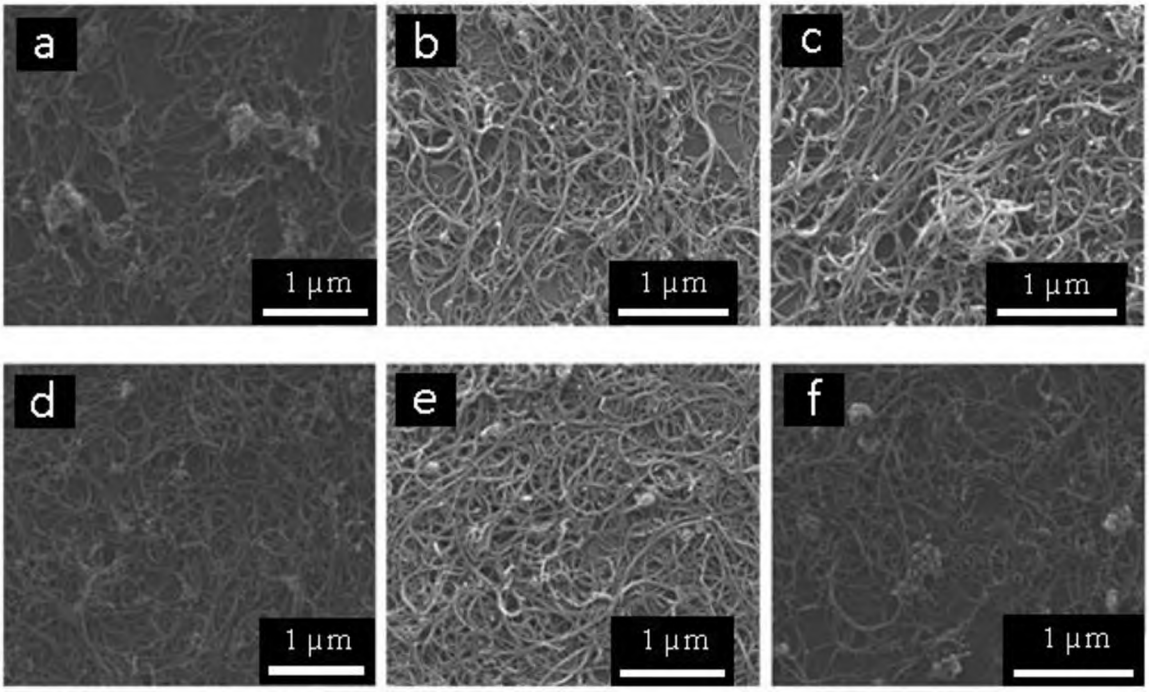

Figure 14: Scanning Electron Microscopy images of MWCNT films compressed to their critical areas. CNTs are modified for different durations as follows: a) No modification b) ~40 minutes c) ~1 hour d) ~2 hours e) ~4 hours f) ~6 hours.

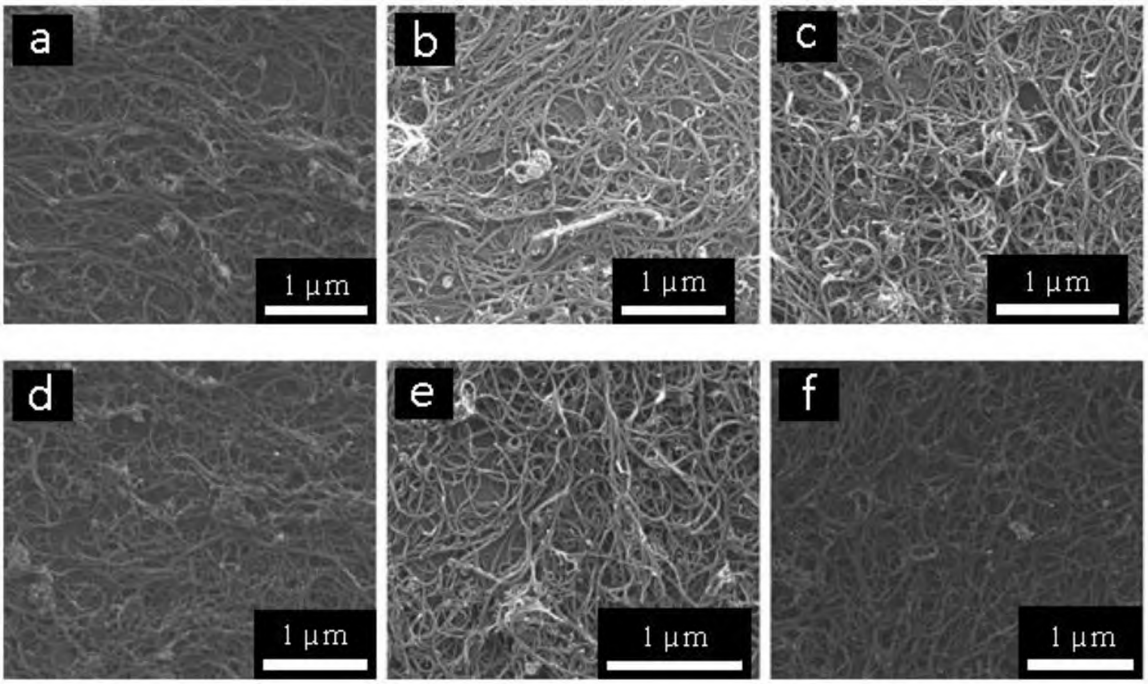

Figure 15: Scanning Electron Microscopy images of MWCNT films compressed to 25 cm^2. CNTs are modified for different durations as follows: a) No modification b) ~40 minutes c) ~1 hour d) ~2 hours e) ~4 hours f) ~6 hours.

The SEM micrographs shown in **Figures 14** & **15** show the industrial grade MWCNT films were heterogeneous, with most particles grouped with others in bundles. In addition, individual MWCNTs were not observed to be physically altered by the oxidation process. Bundling in these samples likely originated from the strong Van der Waals attraction between MWCNTs in addition to capillary attraction during SEM sample preparation. Particles deposited on a substrate and dispersed in an evaporating fluid will experience capillary attraction when the fluid level reaches the particles. As will be described later in this document, particles that locally deform an interface will experience attraction to

minimize that local deformation (i.e. minimize the energy associated with that deformation).

Figures 14 & 15 also reveal the microstructure of the deposited film. Small patches of alignment appear in the images, though there does not appear to be a correlation between the patchy alignment and trough area or modification time. Layers of tubes appear in the microstructure instead of a single monolayer. The layers are not discreet. The tubes dip in and out of other layers, weaving tangles of tubes that overlap in different places. This makes determining the thickness of the films in terms of number of layers difficult.

4.3 Film formation, densification, and mechanics of the MWCNT film

Surface pressure versus trough area data was collected to understand the interfacial properties of the films spread on the air/water interfaces. Three-cycle compressions of MWCNT films of varying degrees of oxidation were performed on a Langmuir-Blodgett trough. The surface pressure was recorded via a micro balance and Pt wire, and plotted against the trough area.

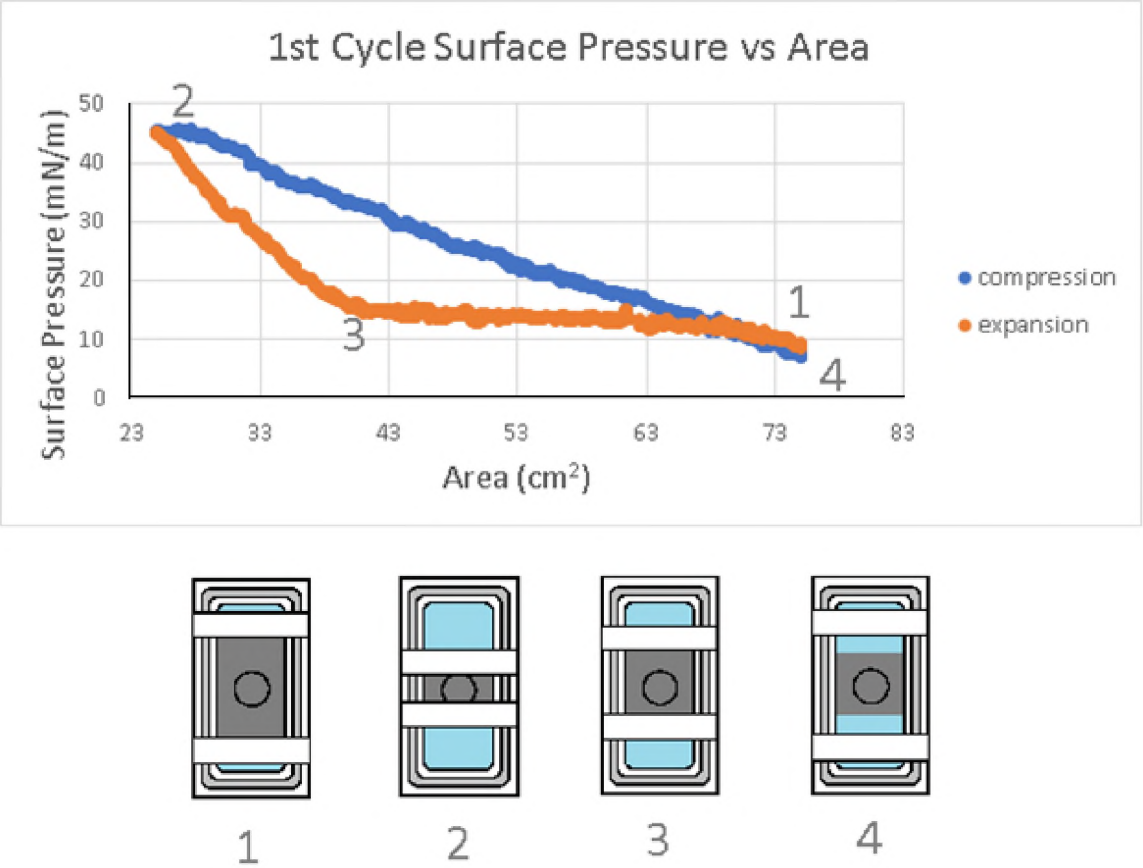

Figure 16: Surface Pressure vs trough area data for the initial compression cycle for unmodified MWCNTs at the interface of air and water at room temperature. The numbering on the graph corresponds to the numbers beneath the trough schematics, indicating the state of the trough at the indicated places on the graph.

Figure 16 shows the surface pressure as a function of area. At point (1), the MWCNTs were initially spread evenly over the trough's area between the barriers. The material filled the available area at this initial state. Next, the barriers were closed to initiate the first compression. The surface pressure increased monotonically as the surface concentration of MWCNTs increased. The slope of the surface pressure vs. area has a steady slope because

the film is in constant contact with the barriers. Point (2) is the location of minimum surface area and maximum surface concentration of MWCNTs. At (2), the motion of the barriers reverses, allowing the film to expand as the barriers expand to increase the available interfacial area. The steep slope at the beginning of the expansion moving from position (2) to position (3) occurred while the film was in contact with the barriers. At position (3) in **Fig.16** the film detaches itself from the barriers as they expand at the critical area, A_c (see **Fig. 17**). The slope of surface pressure vs. ln(A) was flat once the interfacial area increased beyond the critical area because the film was no long attached to the barriers, thereby relieving any compressive strain felt by the film.

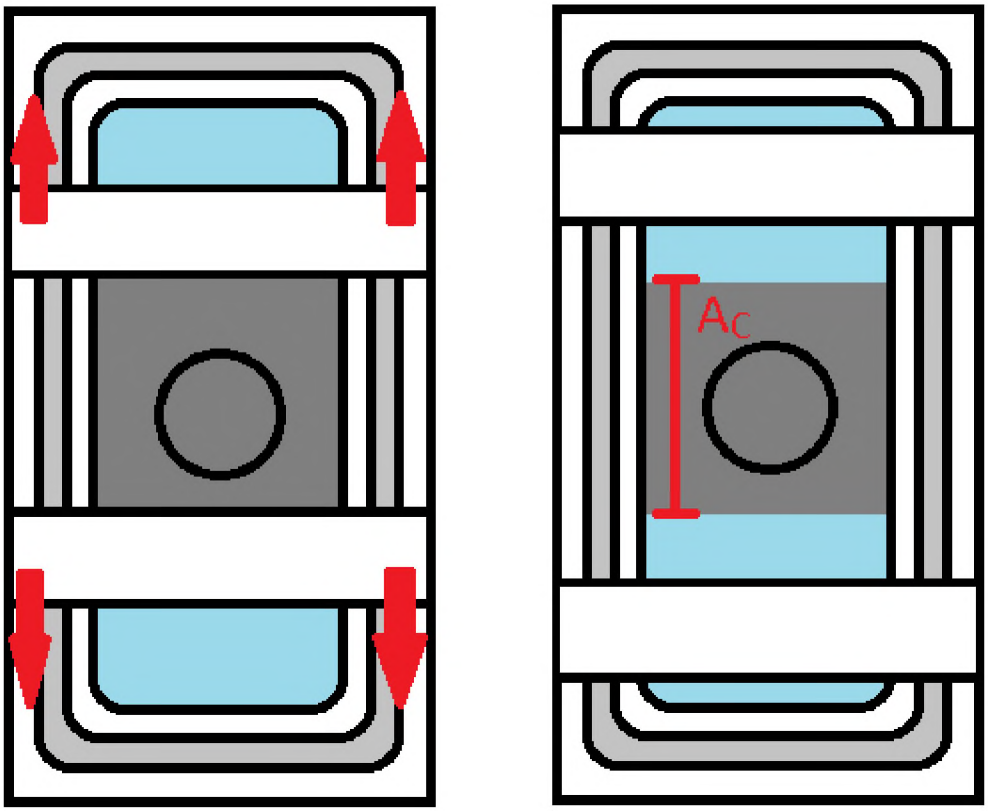

Figure 17: Schematic drawing depicts the barriers expanding, and the film detaching from the barriers at the critical area, A_c.

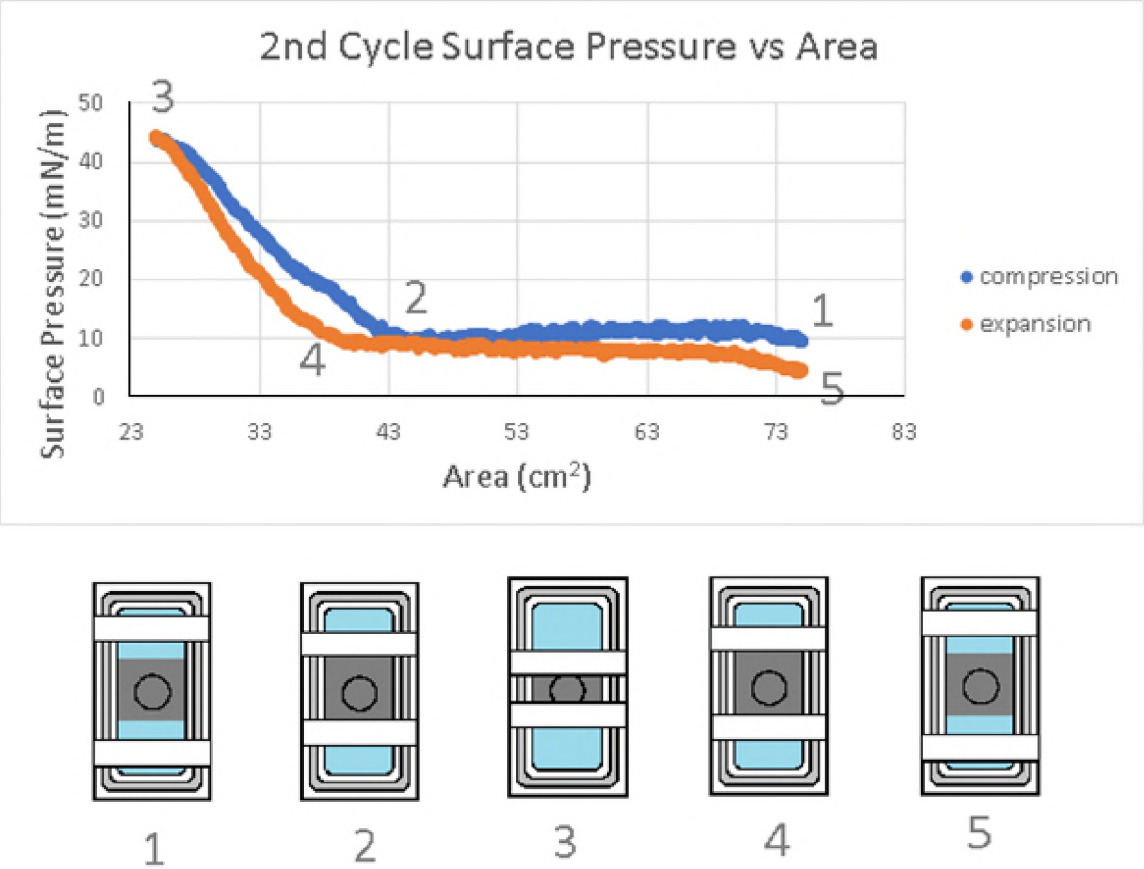

Figure 18: Surface Pressure vs trough area data for the second compression cycle for unmodified MWCNTs at the interface of air and water at room temperature.

The compression part of the subsequent cycles does not have the steady slope as in the initial cycle since the film has detached from the barriers. This is due to the film not springing back to its original state of full trough coverage after the first cycle. The new initial state for the second and third cycles of compression is the same as the final state of the first compression. It is indicated as position (1) in **Fig. 18**. The shallow slopes between positions (1) and (2) and between positions (4) and (5) in **Fig. 18** occur when the film is not in contact with the barriers, and the steep slopes between positions (2) and (3) and between positions (3) and (4) in **Fig. 18** are when the film is in contact with the barriers.

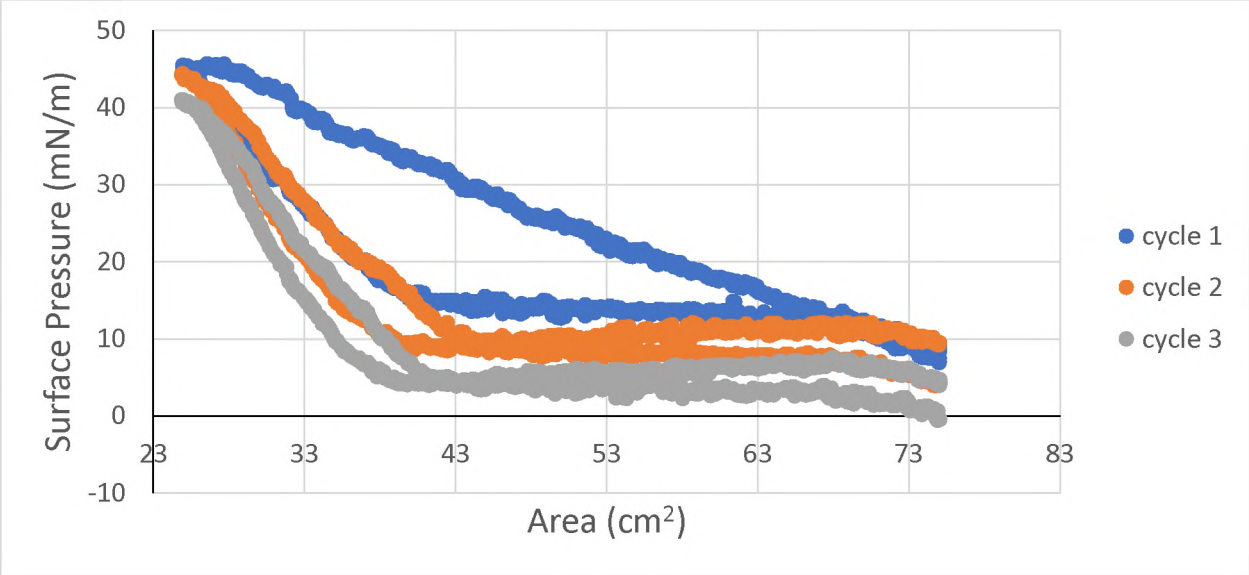

Figure 19: Surface Pressure vs trough area data for all three compression cycles for unmodified MWCNTs at the interface of air and water at room temperature.

Figure 19 depicts the surface pressure vs area data for a full three-cycle compression experiment. Results summarized above show a strong relationship between critical area and surface pressure. The critical area for each sample is summarized **Table 1**. Note that the critical area corresponds to a critical surface concentration. The surface concentration increased as the trough area decreased and the film was compressed. The surface concentration Γ is given by:

$$\Gamma = m_{CNT}/A_{Trough} \qquad (6)$$

where m_{CNT} is the mass of carbon nanotubes added to the interface and A_{Trough} is the trough area. The mass of CNTs added to the interface can be calculated for each sample from the density of the mixture of IPA, water, and CNTs, the exact weight percent of CNTs in the mixture, and the volume of mixture added to the interface. The critical compression

ratio is then the equal to the quotient of the critical and initial surface concentrations, which is equal to the quotient of the initial and critical trough area:

$$\frac{\Gamma_C}{\Gamma_o} = critical\ compression\ ratio \tag{7}$$

where Γ_C is the critical surface concentration and Γ_o is the initial surface concentration. The critical compression ratio indicates the extent of densification within the film; a larger value of Γ_C corresponds to a denser film. The critical compression ratio will have a minimum value of 1 because the critical area could not have been > 1 in the experiments described herein.

mod time (hrs)	Critical area (cm^2)
0	40.02
0	45.07
0.6667	38.05
0.6667	38.54
1	39.69
1	38.54
2	35.55
2	34.92
4	32.43
4	34.43
6	32.50
6	32.76

Table 1.

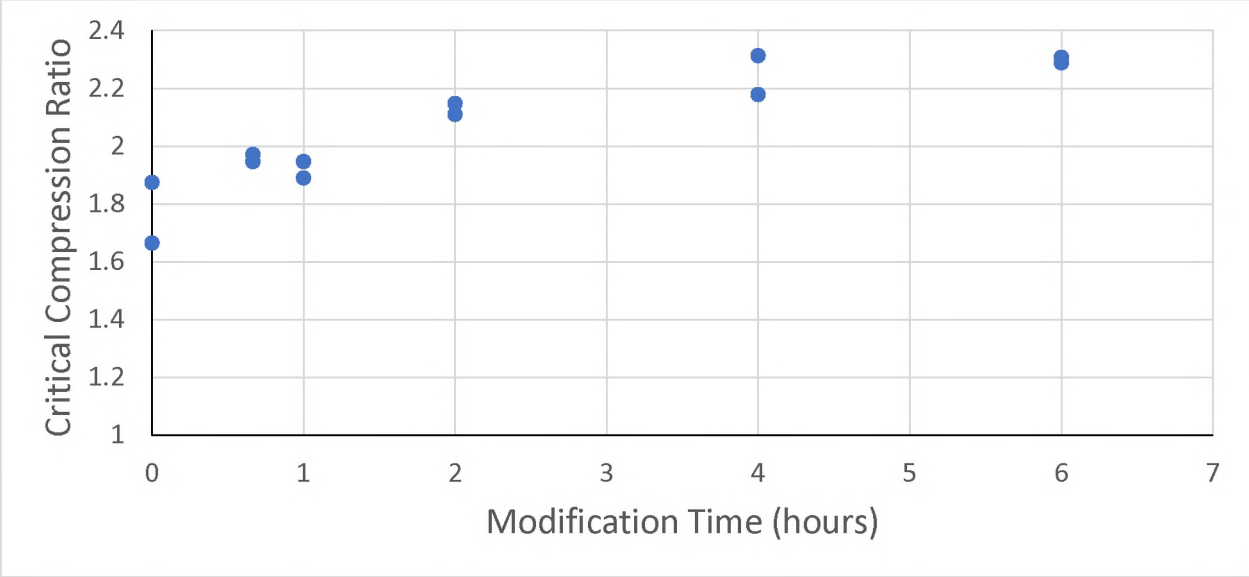

Figure 20: The critical compression ratio is plotted on the y-axis against modification time plotted on the x-axis. The data for critical area is taken from the room temperature data points in table 1.

Figure 20 shows the critical compression ratio plotted as a function of modification time. Recall that the critical area was defined on the expansion cycle. Data summarized in **Figure 20** shows that the critical compression ratio increased with increasing modification time, implying that densification of the film increased with increasing oxidation.

4.4 Elastic Response of Interface

The value of the slope of the surface pressure vs ln(A) can be used to calculate the Gibbs elasticity of the MWCNT laden interface. Elasticity is an important property for the stability of multiphase materials. The x-axis was placed in a natural log scale so that the slope would be in the correct for to calculate the elasticity via equation (5).

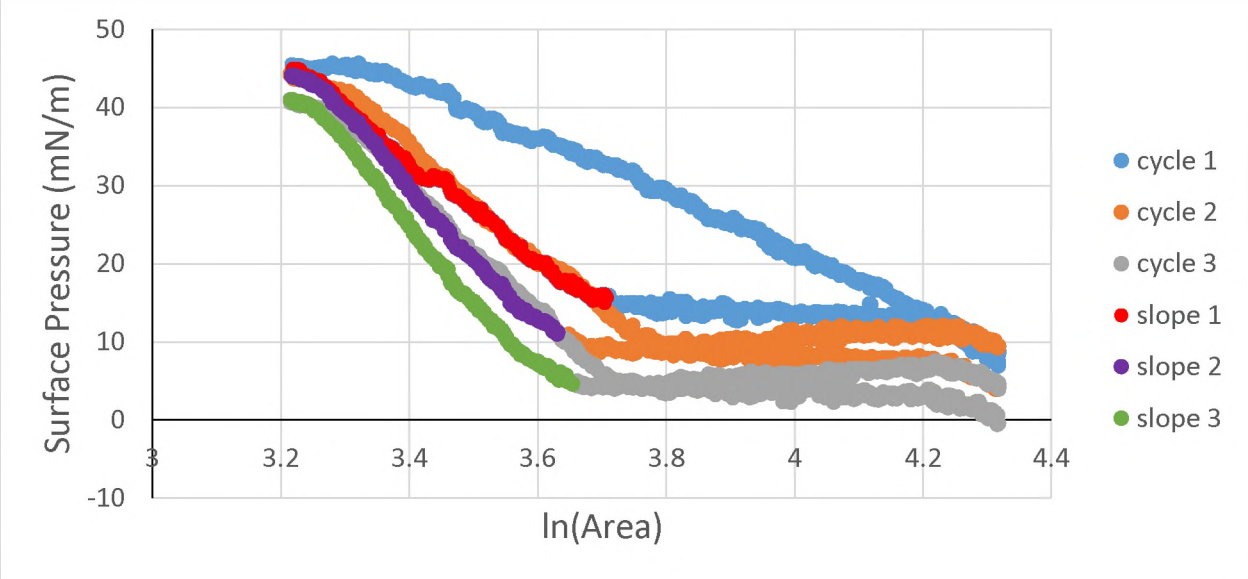

Figure 21: Surface Pressure vs the natural log of the trough area data for all three compression cycles for unmodified MWCNTs at the interface of air and water at room temperature. The slopes of the graph during expansion are highlighted by different colors.

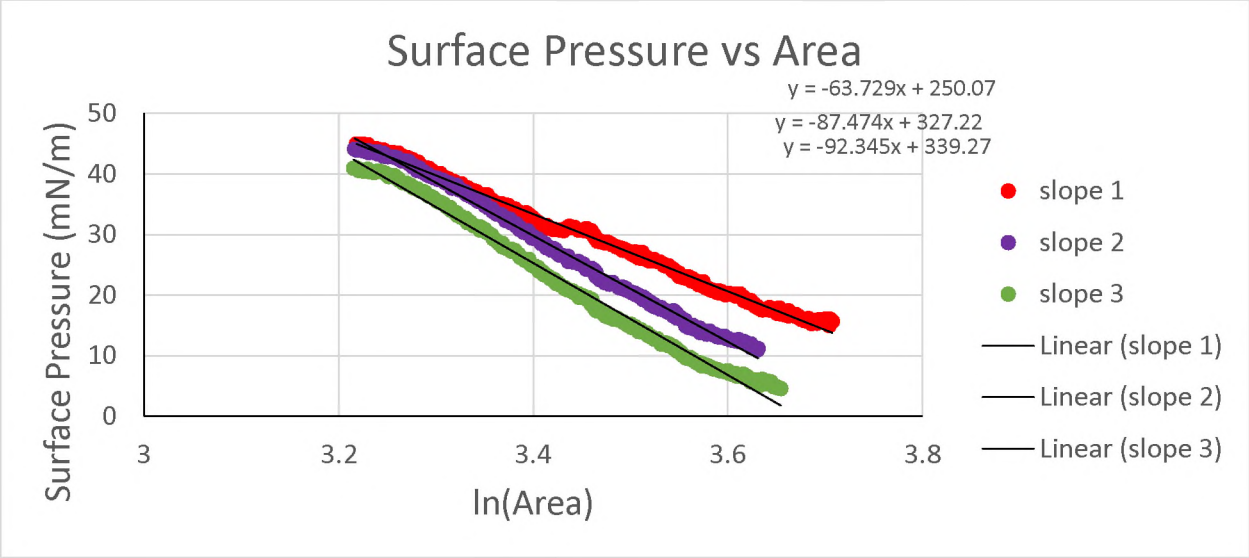

Figure 22: The slopes during expansion are isolated here, and trendlines and equations are assigned to each of them.

Figure 21 shows each compression of the surface pressure measurements for unmodified MWCNTs. Three cycles of compressions were performed for each modification time. As noted earlier, the steep slopes associated with each compression cycle at small values of ln(A) correspond to the dilatation of the flocculated film of MWCNTs. The slope can be expressed as $\frac{d\,\Pi}{d\,\ln(A)}$ which is equivalent to -E_G according to equation (5). The sections of the data from which the slopes would be determined were isolated from the rest of the data, and a linear trendline was plotted via Microsoft Excel (see **Fig. 22**). Repeating this process for each sample of different modification duration yields different slopes. Each slope is recorded in Table 2 below. Gibbs Elasticity is calculated by multiplying the slopes by -1. They are tabulated below in Table 2.

E_{Gibbs}:

Mod t (hrs)	Cycle 1 (mN/m)	Cycle 2 (mN/m)	Cycle 3 (mN/m)
0	63.73	87.47	92.35
0.66667	73.60	89.19	98.40
1	60.00	74.78	85.86
2	88.40	99.71	112.92
4	83.11	97.16	112.29
6	93.38	108.91	133.25

Table 2.

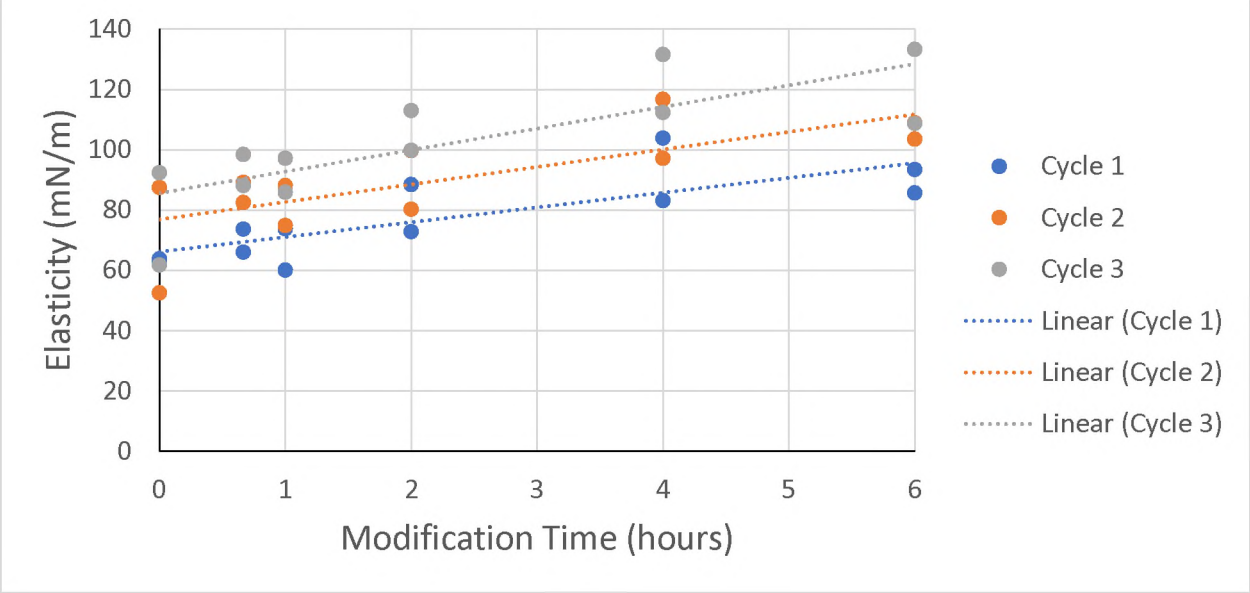

Figure 23: The film elasticity for four trials of compressions, two at room temperature and two temperature controlled experiments at 25°C, is plotted on the y-axis against the duration of modification in hours on the x-axis.

The trend in **Figure 23** shows that the Gibbs elasticity tends to increase as the oxidation time increases. Therefore, with increasing oxidation duration the films become both denser and more stiff. The denser packing of the films with longer modification times may contribute to the higher elasticities observed for these films. The relationship between film densification and elasticity is more evident when plotting the elasticity against the critical compression ratio (see **Fig. 24**). High critical compression ratios correspond to lower critical areas.

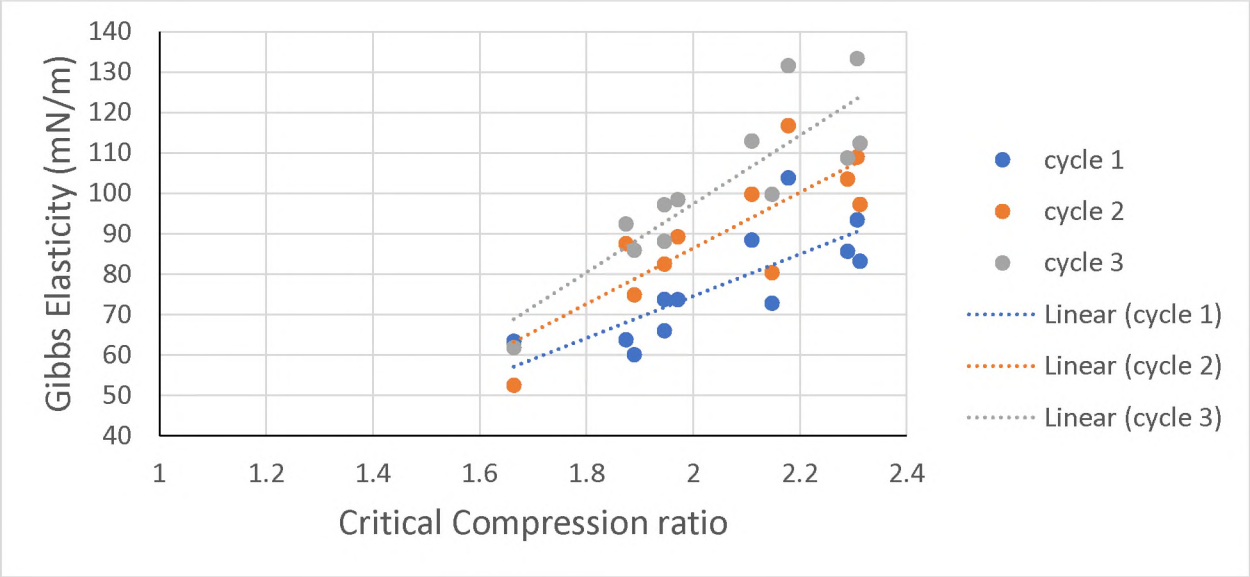

Figure 24: Gibbs Elasticity plotted as a function of the critical compression ratio. Elasticity tends to increase as the critical compression increases.

The Gibbs elasticity increases with a corresponding increase in critical compression ratio further supporting the idea that a denser film is also a stiffer film. In addition, this elasticity increases with each subsequent cycle of compression. This implies that the

action of compressing the film aids in the densification of the films and causes higher Gibbs elasticities.

4.5 Optical Microscopy image analysis

A 3D printed replica of the Langmuir-Blodgett trough used for surface pressure measurements was utilized for viewing the microstructure under an optical microscope. It was printed with the same length, width, and depth as the original trough, but thin enough to fit beneath the microscope objectives, and fit snuggly into the microscope stage. Films comprised of unmodified tubes and tubes of two-hour and six-hour oxidation times were used for this image analysis. Snapshots were taken in the second cycle of compression for the films, therefore the range of areas worth comparing is from 40 cm^2 down to 25 cm^2, as 40 cm^2 is near the films' critical areas at which most films detached from the barriers during expansion in the first cycle (see **Fig. 16** position (3)).

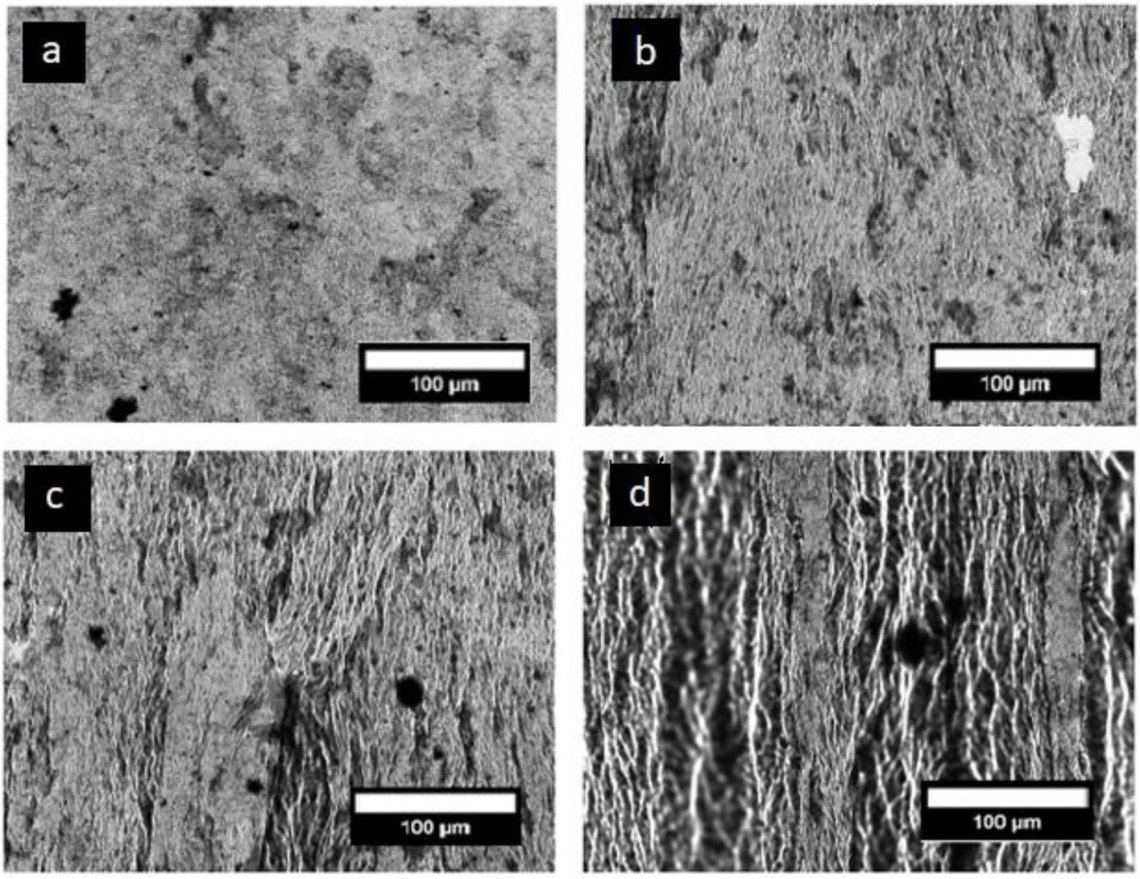

Figure 25: Unmodified CNT film at different stages of compression. Trough areas: a) 40 cm^2 b) 35 cm^2 c) 30 cm^2 d) 25 cm^2.

Figure 25 shows the progression of the film microstructure under increasing compression. Trough area decreases steadily from image a to image d.

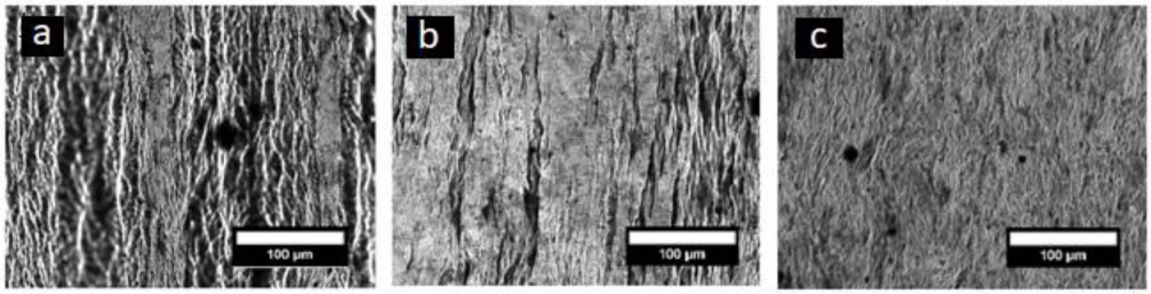

Figure 26:CNT films of various modification durations at a trough area of 25 cm^2. Modification durations: a) Unmodified b) 2 hours c) 6 hours.

Some images taken at low trough areas (maximum compression) contain sections of the image that are out of focus (see **Fig. 25** (d) and **Fig. 26** (a) and (b)). These sections indicate buckling in the film [37]. **Figure 26** shows that buckling in the film is more prevalent in films with low modification durations since there are more sections out of focus for the unmodified film than the 2 hour modified film, and more out of focus sections in the 2 hour modified film than the 6 hour modified film. This agrees with the critical area and Gibbs elasticity data. The denser, stiffer films are more difficult to deform. Therefore, buckling occurs less frequently in films with longer modification times.

4.6 Stepwise compressions and total film relaxations

The surface pressure changes due to the thermodynamic changes brought on by changing surface concentration, and by the microstructural surface stresses imposed by the physical compression action. Investigation of these individual components of the surface stress is accomplished through step compressions with allotted time between compressions

for the film to relax to a steady state. The steady state values between compressions would be used to get the true surface pressure isotherm, since the effect on the surface pressure in that scenario would depend only on the thermodynamic change due to changing surface concentration of particles.

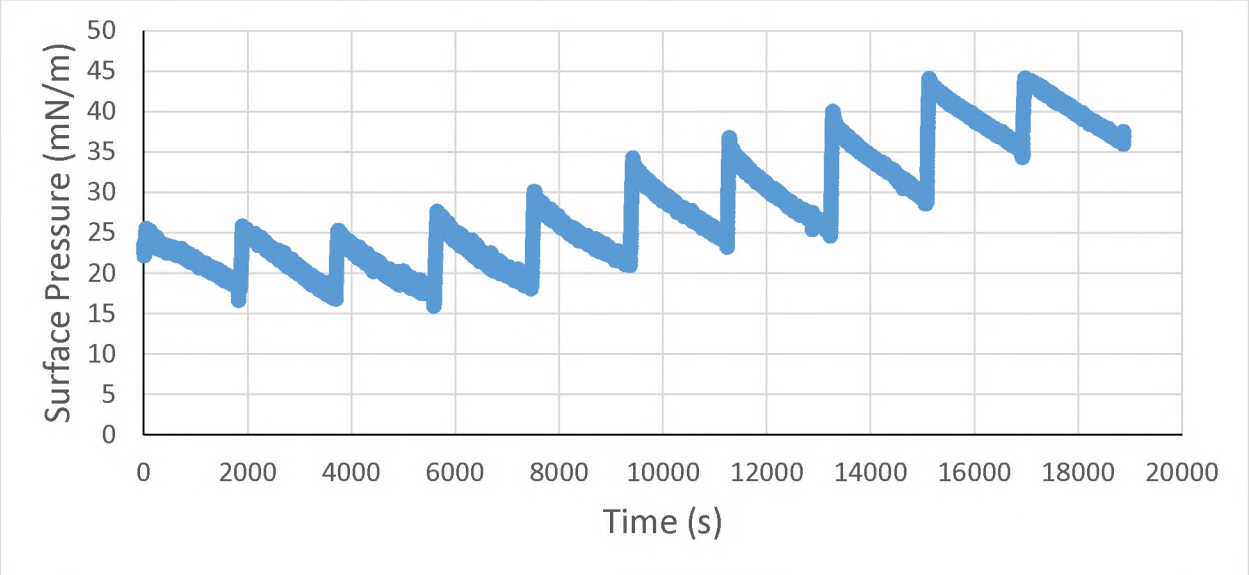

Figure 27: Stepwise compression of a film of unmodified MWCNTs. Every 1800 seconds (30 minutes), a step down of 5 cm^2 in trough area would occur.

Figure 27 shows the surface pressure vs time data for compressions performed in 5cm^2 increments with 30 minutes between compression steps. These stepwise compressions were performed for each modification time. The difference in the steady state surface pressures from one compression to the next is the thermodynamic component of the stress. The initial spike in surface pressure is due to the physical microstructural surface stresses. Interfacial rheology experiments can be used to further analyze these responses, but that is beyond the scope of this work. Unfortunately, the 30 minutes allocations between

compression steps did not allow enough time for the film to relax such that the surface pressure reached a new equilibrium steady state value.

To find the timescale at which the film has relaxed fully, compressions were performed with a single 5 cm^2 change and allowed to sit until the surface pressure value no longer changed.

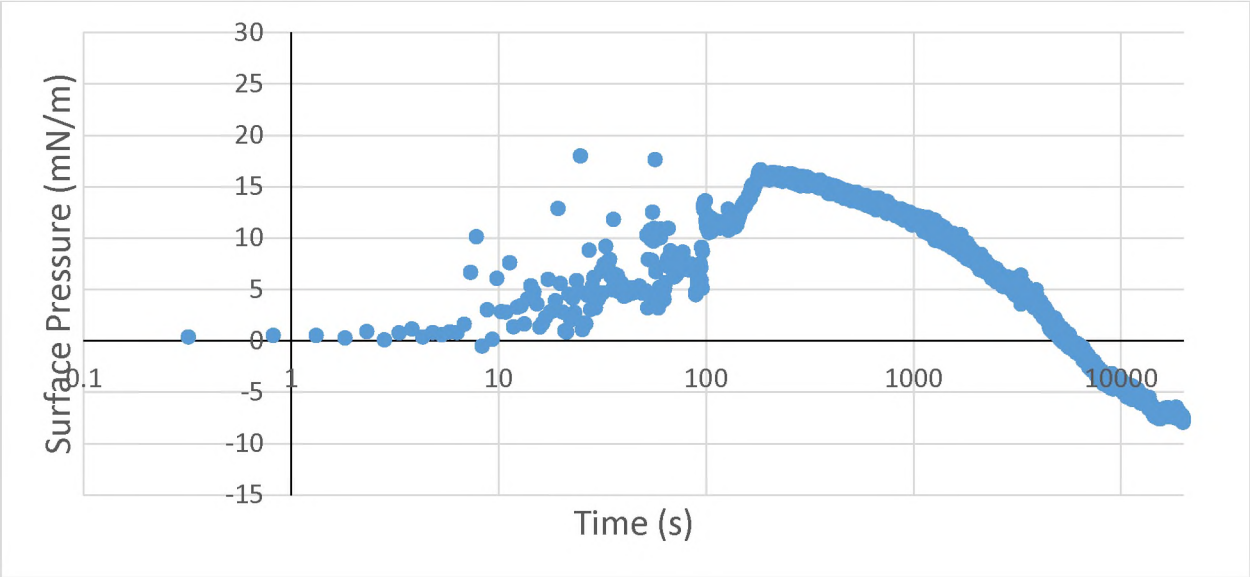

Figure 28: A semi-log plot of a film of unmodified MWCNTs compressed from 75 cm^2 to 70 cm^2 and allowed to relax overnight.

Figure 28 shows surface pressure vs time data for a single 5 cm^2 compression followed by a long relaxation. The extended time scale was still not enough to allow for a new equilibrium surface pressure. The effect of evaporation of the subphase eventually causes the platinum wire to pull out of the interface, and end the experiment before a steady surface pressure is recorded. Nevertheless, the long relaxation data can be used to predict what would happen if the film was able to relax to a new steady state.

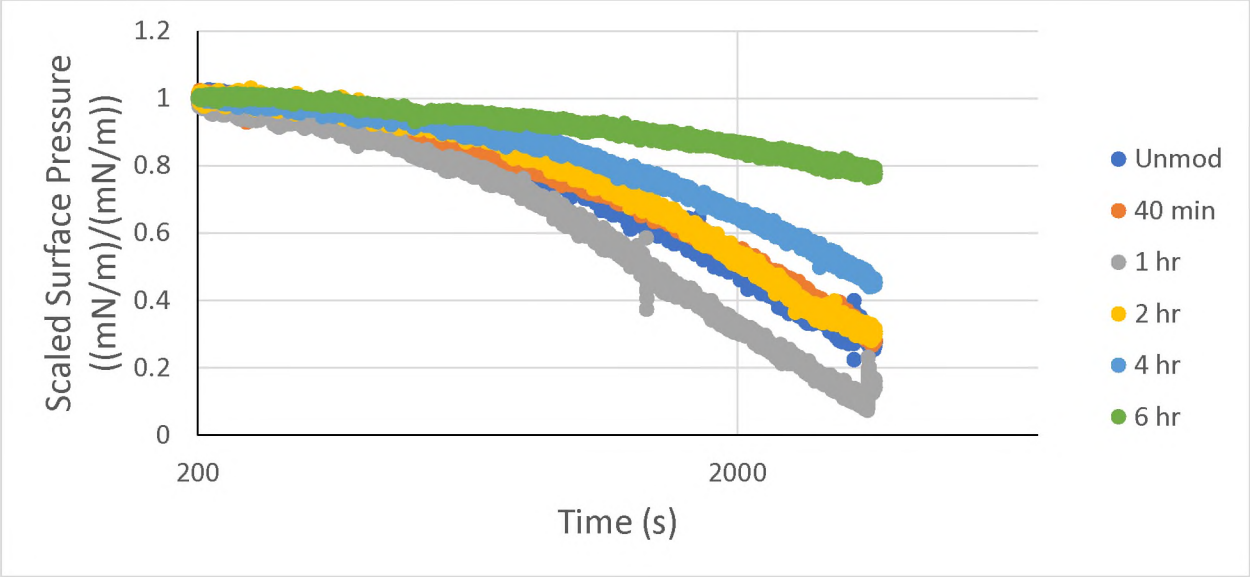

Figure 29: Scaled surface pressure plotted against time for long-scale relaxation time measurement. The more shallow the slope, the longer the relaxation time or the higher the eventual equilibrium surface pressure.

Figure 29 compares the long relaxation data for each modification time. The data for each modification time can be more easily compared by dividing the surface pressure values of each run by their respective maximum surface pressures after compression such that all the relaxations start at a scaled surface pressure of 1 mN/m. One of two effects can be inferred from the slopes in the graph (see **Fig. 29**). Longer relaxation times may be indicated by the shallower slopes for the higher modification times on the graph below. Alternatively, higher equilibrium surface pressures may be indicated by the shallower slopes. Either or both effects are possible. Therefore, with increasing oxidation durations, the relaxation times and/or the equilibrium surface pressures increase.

4.7 Isothermal surface pressure versus area measurements

To gauge the effect of temperature on surface pressure measurements, isothermal measurements were conducted by using a Polystat water circulation system in conjunction with a NIMA Langmuir-Blodgett trough. The room temperature in the lab would vary slightly, so each sample of varying modification time was tested in isothermal conditions at 20°C for one trial each, 25°C for two trials each, and 30°C for one trial each. Calibration of the water circulation bath such that the desired trough temperature would be maintained was performed by monitoring the tough temperature and changing the setpoint temperature of the circulation bath. An equation yielding trough temperature as a function of bath temperature was acquired, and utilized to determine the optimal settings for the compressions.

$$T_{Bath} = \left(\frac{1}{0.624}\right) * (T_{Trough} - 7.99) \quad (8)$$

Trough temperature was monitored with an AMPROBE temperature probe during the calibration and the compressions. Bath temperature was monitored by the circulation device itself.

Compression cycles were performed in the same manner as the room temperature experiments with the addition of the temperature regulating apparatus. The elasticity was calculated for all surface pressure isotherms in the same manner as the room temperature surface pressure measurements. Results may be tainted due to convection in the trough due to the temperature gradient induced by the heated or cooled water circulating through the trough's innards. Convection in the subphase could cause excess stresses in the film and at

the interface, adding an additional level of complexity in determining the behavior of the CNT films at the interface.

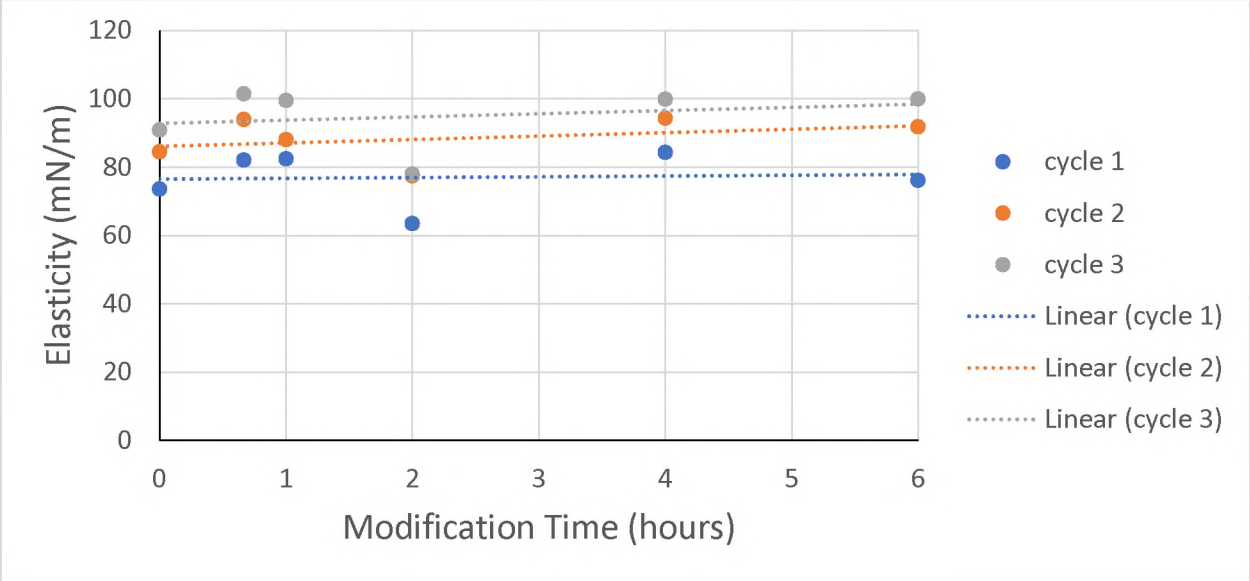

Figure 30: Gibbs Elasticity plotted vs modification time for trials performed at 20 ºC.

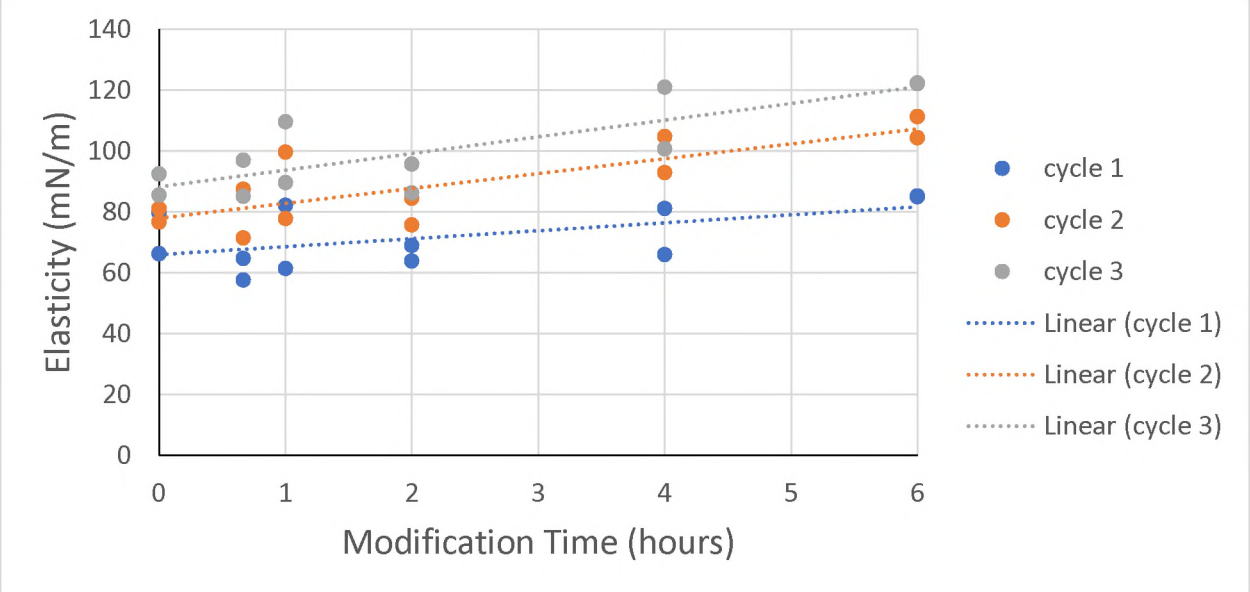

Figure 31: Gibbs Elasticity plotted vs modification time for trials performed at 25 ºC.

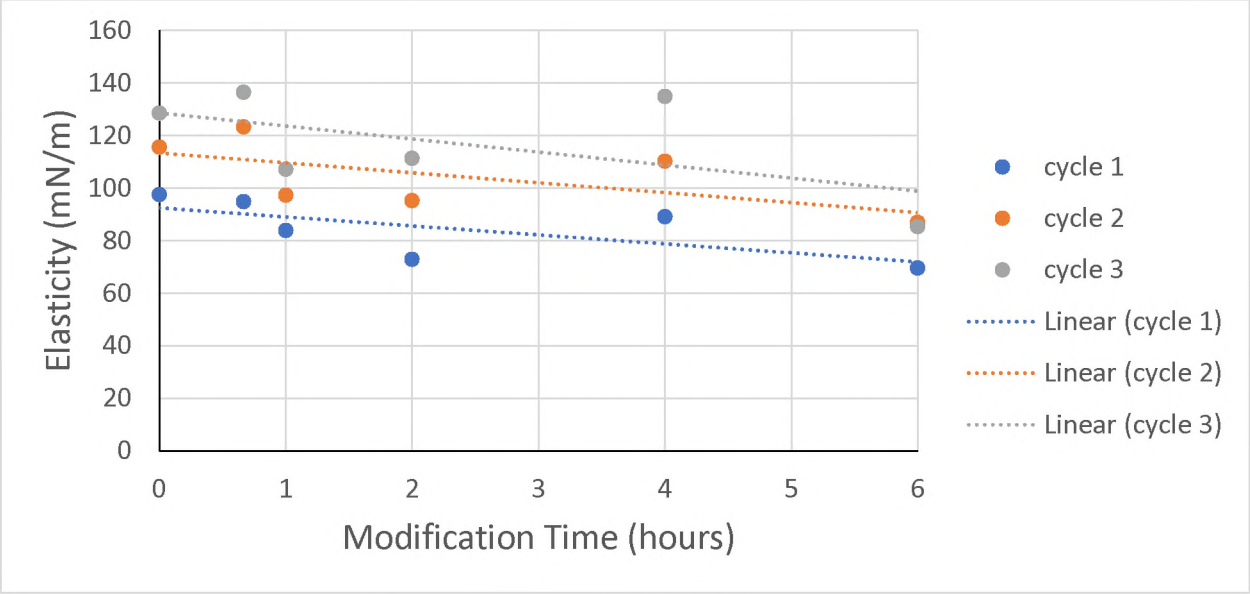

Figure 32: Gibbs Elasticity plotted vs modification time for trials performed at 30 ºC.

4.8 Discussion: Origin of film formation and mechanics

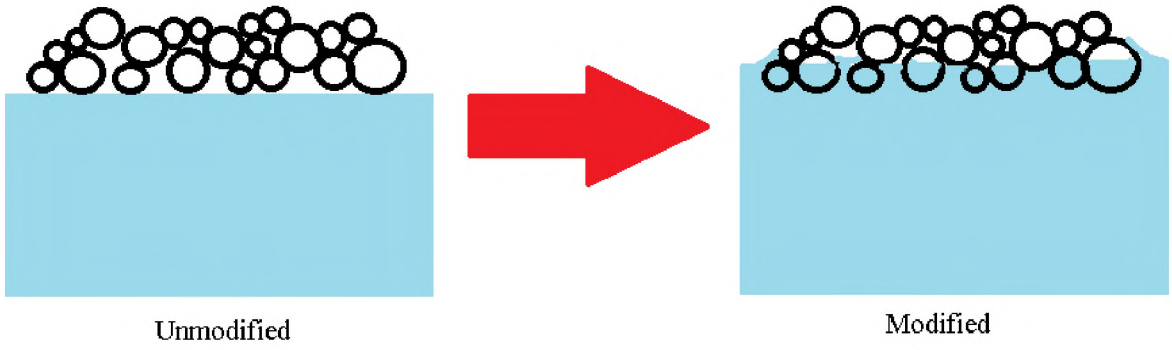

Figure 33: The black rings represent CNTs in cross-section sitting at an air/water interface.

In **Figure 33**, the unmodified tubes sit atop the interface without causing deformation of the surface because of their hydrophobic nature. With a lack of affinity for the water phase, the unmodified tubes are more at home in the air phase. The modified tubes are more hydrophilic due to the polar groups added to their surfaces during oxidation. Therefore, the modified tubes adsorb more strongly to the interface, deforming it as they come into contact with both phases of the interface. The deformation arises from the anisotropy in the shape of the particles, causing an excess in surface area of the interface and raising the surface energy. To minimize the excess surface area and the surface energy, the particles aggregate via capillary attractions such that the deformations due to their presence at the interface are pushed to the outsides of the film that is formed. Therefore, the longer modification times cause more capillary attractions forming denser films with lower critical areas. This agrees with the elasticity data. Comparing the data, the denser films are also the stiffest films. These films would be more difficult to deform. This is supported further by the optical microscopy data, since film buckling is more prevalent at low modification durations. Buckling in the films is less prevalent as the modification time increased because the more modified films were denser and had higher Gibbs elasticities than the unmodified or slightly modified tubes.

CHAPTER V

CONCLUSIONS AND RECOMMENDATIONS

Particle stabilized interfaces have a variety of applications across several fields. The particles employed to stabilize interfaces can pass their properties to the larger material they find themselves stabilizing. Carbon nanotubes are worthwhile particles to investigate therefore, due to their tensile, thermal, and electrical properties. Unfortunately, little is known about their interfacial properties.

To investigate the interfacial properties of CNTs at an air/water interface, surface pressure versus trough area data for compressions on a Langmuir-Blodgett trough was collected and analyzed. In addition, imaging of the interface under optical microscopy and SEM helped characterize the film microstructures formed. SEM imaging showed that, while some alignment occurs in the films, it does not seem to be affected by the modification in any significant way at the durations studied. In addition, the tubes were not observably altered in length or diameter by the modification. Surface pressure data was recorded via three-cycle compressions. The critical area of the films appeared to be affected by the modification time, such that the critical area was smaller at longer modification times. From the slopes of the surface pressure vs ln(A) graphs, the film elasticity could be

determined. The elasticity tended to increase with a corresponding increase in the duration of modification of the MWCNTs. The elasticity also increased with each subsequent cycle of compression on the trough, indicating a change in film structure with each subsequent compression. Imaging the films with optical microscopy yielded evidence of film buckling at low trough areas. In addition, the buckling was more prevalent in films with low modification times.

To understand the physical response of the system to stress, stepwise compressions were performed. The initial change in surface pressure represented the microstructural response of the films to the stress of compression. The thermodynamic effect on the surface pressure could not be determined because the film did not relax to a steady state surface pressure in the time allotted between compressions. Longer durations of relaxation were implemented to attempt to reach an equilibrium surface pressure. For the long relaxation compressions, the films still did not relax to a constant surface pressure before the wire pulled out of the interface due to evaporation of the subphase. However, extrapolating the data shows three possible outcomes. Either the relaxation times generally were longer with increasing modification duration, that the thermodynamic response was likely more pronounced for films with higher modification times, or a combination of these effects.

The contributions of this thesis are as follows:

- For films with little or no modification, buckling of the film is evident under compression, and this effect is mitigated for the longer modification times. In addition, film densification occurs for longer modification durations as evidenced by the smaller critical area for those films.

- The elasticity of the films increased with increasing modification time. We believe this is a consequence of the densification of the films that have been modified for longer durations.
- At the interface, longer duration modified tubes have enhanced capillary attractions to one another, while tubes with little to no modification sit atop the interface without deforming the interface as much. This physical understanding of the behaviors of the carbon nanotubes at the interface of air and water is supported by the all the data collected.

In future works, compressions should be performed such that the spreading agent, in this case isopropyl alcohol, is evaporated or otherwise removed from the interface. Evaporation of isopropyl alcohol during compressions causes a decrease in surface pressure with time for a little more than an hour. In addition, the effect that isopropyl alcohol has on the wetting of the tubes should be assessed, as both subphase and surface chemistry interactions have an effect on the wettability of the particles to the interface.

REFERENCES

1. Velev, O. D. and Lenhoff, A. M. "**Colloidal Crystals as Templates for Porous Materials**" *Current Opinion in Colloid & Interface Science* 5, no. 1 (2000): 56–63. doi:10.1016/S1359-0294(00)00039-X

2. Melle, S., Lask, M., and Fuller, G. G. "**Pickering Emulsions with Controllable Stability**" *Langmuir* 21, no. 6 (2005): 2158–2162. doi:10.1021/la047691n

3. Binks, B. P. and Lumsdon, S. O. "**Pickering Emulsions Stabilized by Monodisperse Latex Particles: Effects of Particle Size**" *Langmuir* 17, no. 15 (2001): 4540–4547. doi:10.1021/la0103822

4. Chevalier, Y. and Bolzinger, M.-A. "**Emulsions Stabilized with Solid Nanoparticles: Pickering Emulsions**" *Nanoparticles@interfaces* 439, no. Supplement C (2013): 23–34. doi:10.1016/j.colsurfa.2013.02.054

5. Coleman, J. N., Khan, U., Blau, W. J., and Gun'ko, Y. K. "**Small but Strong: A Review of the Mechanical Properties of Carbon Nanotube–polymer Composites**" *Carbon* 44, no. 9 (2006): 1624–1652. doi:10.1016/j.carbon.2006.02.038

6. Bauhofer, W. and Kovacs, J. Z. "**A Review and Analysis of Electrical Percolation in Carbon Nanotube Polymer Composites**" *CNT-NET 07 Special Issue with regular papers* 69, no. 10 (2009): 1486–1498. doi:10.1016/j.compscitech.2008.06.018

7. Dickinson, E. "**Proteins at Interfaces and in Emulsions Stability, Rheology and Interactions**" *Journal of the Chemical Society, Faraday Transactions* 94, no. 12 (1998): 1657–1669. doi:10.1039/A801167B

8. Argyropoulos, D. S. "**Materials, Chemicals, and Energy from Forest Biomass**" 954, (2007): doi:10.1021/bk-2007-0954, Available at http://pubs.acs.org/doi/book/10.1021/bk-2007-0954

9. Zhang, T., Davidson, D., Bryant, S. L., and Huh, C. "**Nanoparticle-Stabilized Emulsions for Applications in Enhanced Oil Recovery**" (2010): doi:10.2118/129885-MS, Available at https://www.onepetro.org/conference-paper/SPE-129885-MS

10. Vignati, E., Piazza, R., and Lockhart, T. P. "**Pickering Emulsions: Interfacial Tension, Colloidal Layer Morphology, and Trapped-Particle Motion**" *Langmuir* 19, no. 17 (2003): 6650–6656. doi:10.1021/la034264l

11. F.Y. Ushikubo and R.L. Cunha. "**Stability Mechanisms of Liquid Water-in-Oil Emulsions**" *Food Hydrocolloids* 34, (2014): 145–153. doi:10.1016/j.foodhyd.2012.11.016

12. Goff, H. D. "**Instability and Partial Coalescence in Whippable Dairy Emulsions**" *Journal of Dairy Science* 80, no. 10 (1997): 2620–2630. doi:10.3168/jds.S0022-0302(97)76219-2

13. Berg, J. C. "**An Introduction to Interfaces & Colloids: The Bridge to Nanoscience**" (2010):

14. Lau, K. K. S. and Gleason, K. K. "**Particle Functionalization and Encapsulation by Initiated Chemical Vapor Deposition (ICVD)**" *Surface and Coatings Technology* 201, no. 22–23 (2007): 9189–9194. doi:10.1016/j.surfcoat.2007.04.045

15. Lewandowski, E. P., Cavallaro, M., Botto, L., Bernate, J. C., Garbin, V., and Stebe, K. J. "**Orientation and Self-Assembly of Cylindrical Particles by Anisotropic Capillary Interactions**" *Langmuir* 26, no. 19 (2010): 15142–15154. doi:10.1021/la1012632

16. Hone, J., Llaguno, M. C., Nemes, N. M., Johnson, A. T., Fischer, J. E., Walters, D. A., Casavant, M. J., Schmidt, J., and Smalley, R. E. "**Electrical and Thermal Transport Properties of Magnetically Aligned Single Wall Carbon Nanotube Films**" *Applied Physics Letters* 77, no. 5 (2000): 666–668. doi:10.1063/1.127079

17. Rastogi, R., Kaushal, R., Tripathi, S. K., Sharma, A. L., Kaur, I., and Bharadwaj, L. M. "**Comparative Study of Carbon Nanotube Dispersion Using Surfactants**" *Journal of Colloid and Interface Science* 328, no. 2 (2008): 421–428. doi:10.1016/j.jcis.2008.09.015

18. Li, S., Li, H., Wang, X., Song, Y., Liu, Y., Jiang, L., and Zhu, D. "**Super-Hydrophobicity of Large-Area Honeycomb-Like Aligned Carbon Nanotubes**" *The Journal of Physical Chemistry B* 106, no. 36 (2002): 9274–9276. doi:10.1021/jp0209401

19. Datsyuk, V., Kalyva, M., Papagelis, K., Parthenios, J., Tasis, D., Siokou, A., Kallitsis, I., and Galiotis, C. "**Chemical Oxidation of Multiwalled Carbon Nanotubes**" *Carbon* 46, no. 6 (2008): 833–840. doi:10.1016/j.carbon.2008.02.012

20. Rosca, I. D., Watari, F., Uo, M., and Akasaka, T. "**Oxidation of Multiwalled Carbon Nanotubes by Nitric Acid**" *Carbon* 43, no. 15 (2005): 3124–3131. doi:10.1016/j.carbon.2005.06.019

21. Gábor, T., Aranyi, D., Papp, K., Kármán, F. H., and Kálmán, E. "**Dispersibility of Carbon Nanotubes**" *Materials Science Forum* 537–538, (2007): 161–168. doi:10.4028/www.scientific.net/MSF.537-538.161

22. Fuller, G. G. and Vermant, J. "**Complex Fluid-Fluid Interfaces: Rheology and Structure**" *Annual Review of Chemical and Biomolecular Engineering* 3, no. 1 (2012): 519–543. doi:10.1146/annurev-chembioeng-061010-114202

23. Gibbs, J. W. "**On the Equilibrium of Heterogeneous Substances**" *American Journal of Science* s3-16, no. 96 (1878): 441–458. doi:10.2475/ajs.s3-16.96.441

24. Li, X., Zhang, L., Wang, X., Shimoyama, I., Sun, X., Seo, W.-S., and Dai, H. "**Langmuir–Blodgett Assembly of Densely Aligned Single-Walled Carbon Nanotubes from Bulk Materials**" *Journal of the American Chemical Society* 129, no. 16 (2007): 4890–4891. doi:10.1021/ja071114e

25. Cote, L. J., Kim, F., and Huang, J. "**Langmuir–Blodgett Assembly of Graphite Oxide Single Layers**" *Journal of the American Chemical Society* 131, no. 3 (2009): 1043–1049. doi:10.1021/ja806262m

26. Tao, A., Kim, F., Hess, C., Goldberger, J., He, R., Sun, Y., Xia, Y., and Yang, P. "**Langmuir–Blodgett Silver Nanowire Monolayers for Molecular Sensing Using Surface-Enhanced Raman Spectroscopy**" *Nano Letters* 3, no. 9 (2003): 1229–1233. doi:10.1021/nl0344209

27. Park, K. H., Kim, B. H., Song, S. H., Kwon, J., Kong, B. S., Kang, K., and Jeon, S. "**Exfoliation of Non-Oxidized Graphene Flakes for Scalable Conductive Film**" *Nano Letters* 12, no. 6 (2012): 2871–2876. doi:10.1021/nl3004732

28. Peterson, I. R. "**Langmuir-Blodgett Films**" *Journal of Physics D: Applied Physics* 23, no. 4 (1990): 379. doi:10.1088/0022-3727/23/4/001

29. Wunderlich, B. "**Extended Chain Crystals of Linear High Polymers**" *Pure and Applied Chemistry* 31, no. 1–2 (2009): 49–64. doi:10.1351/pac197231010049

30. Samaniuk, J. R., Blair, V. E., Vlassopoulos, D., Fuller, G. G., and Vermant, J. "**Langmuir Acrylic Polymer Films: To Entangle, or Not to Entangle?**"

31. Mendoza, A. J., Guzman, E., Martinez-Pedrero, F., Ritacco, H., Rubio, R. G., Ortega, F., Starov, V. M., and Miller, R. "**Particle Laden Fluid Interfaces: Dynamics and Interfacial Rheology**" *Advances in Colloid and Interface Science* 206, (2014): 303–319. doi:10.1016/j.cis.2013.10.010

32. Pradilla, D., Simon, S., Sjöblom, J., Samaniuk, J., Skrzypiec, M., and Vermant, J. "**Sorption and Interfacial Rheology Study of Model Asphaltene Compounds**" *Langmuir* 32, no. 12 (2016): 2900–2911. doi:10.1021/acs.langmuir.6b00195

33. Vora, S. R., Bognet, B., Patanwala, H. S., Chinesta, F., and Ma, A. W. K. "**Surface Pressure and Microstructure of Carbon Nanotubes at an Air–Water Interface**" *Langmuir* 31, no. 16 (2015): 4663–4672. doi:10.1021/la504934x

34. Tchoul, M. N., Ford, W. T., Lolli, G., Resasco, D. E., and Arepalli, S. "**Effect of Mild Nitric Acid Oxidation on Dispersability, Size, and Structure of Single-Walled Carbon Nanotubes**" *Chemistry of Materials* 19, no. 23 (2007): 5765–5772. doi:10.1021/cm071758l

35. Vargaftik, N. B., Volkov, B. N., and Voljak, L. D. "**International Tables of the Surface Tension of Water**" *Journal of Physical and Chemical Reference Data* 12, no. 3 (1983): 817–820. doi:10.1063/1.555688

36. "**Overview of Electrophoresis**" Available at https://www.thermofisher.com/us/en/home/life-science/protein-biology/protein-biology-learning-center/protein-biology-resource-library/pierce-protein-methods/overview-electrophoresis.html

37. Khang, D.-Y., Rogers, J. A., and Lee, H. H. "**Mechanical Buckling: Mechanics, Metrology, and Stretchable Electronics**" *Advanced Functional Materials* 19, no. 10 (2009): 1526–1536. doi:10.1002/adfm.200801065

APPENDICES

APPENDIX A.

(Additional Tables)

Temp (°C)	mod time (hrs)	Critical area (cm^2)
room	0	40.02
room	0	45.07
20	0	35.67
25	0	42.36
25	0	45.67
30	0	36.59
room	0.6667	38.05
room	0.6667	38.54
20	0.6667	33.96
25	0.6667	39.06
25	0.6667	38.10
30	0.6667	33.02
room	1	39.69
room	1	38.54
20	1	33.44
25	1	38.25
25	1	44.23
30	1	31.83
room	2	35.55
room	2	34.92
20	2	39.11
25	2	39.19
25	2	36.54
30	2	37.50
room	4	32.43
room	4	34.43
20	4	33.52
25	4	36.41
25	4	35.83
30	4	33.39
room	6	32.50
room	6	32.76
20	6	32.01
25	6	33.21
25	6	34.77
30	6	30.73

Table 3.

mod time (h)	weight mix (IPA+H2O)(g)	weight CNTs (g)	wt%
0	9.9983	0.0102	0.101913
0	9.9963	0.01	0.099937
0.667	9.9752	0.0113	0.113153
0.667	9.9955	0.0105	0.104937
1	10.001	0.0105	0.104879
1	9.9955	0.0107	0.106934
2	9.991	0.0109	0.108979
2	9.9981	0.0113	0.112894
4	9.9891	0.0107	0.107002
4	9.9895	0.0109	0.108996
6	9.9989	0.0111	0.110889
6	9.9991	0.011	0.109889

Table 4.

APPENDIX B.

(Surface Pressure vs ln(A) graphs)

Room Temperature:

Unmodified:

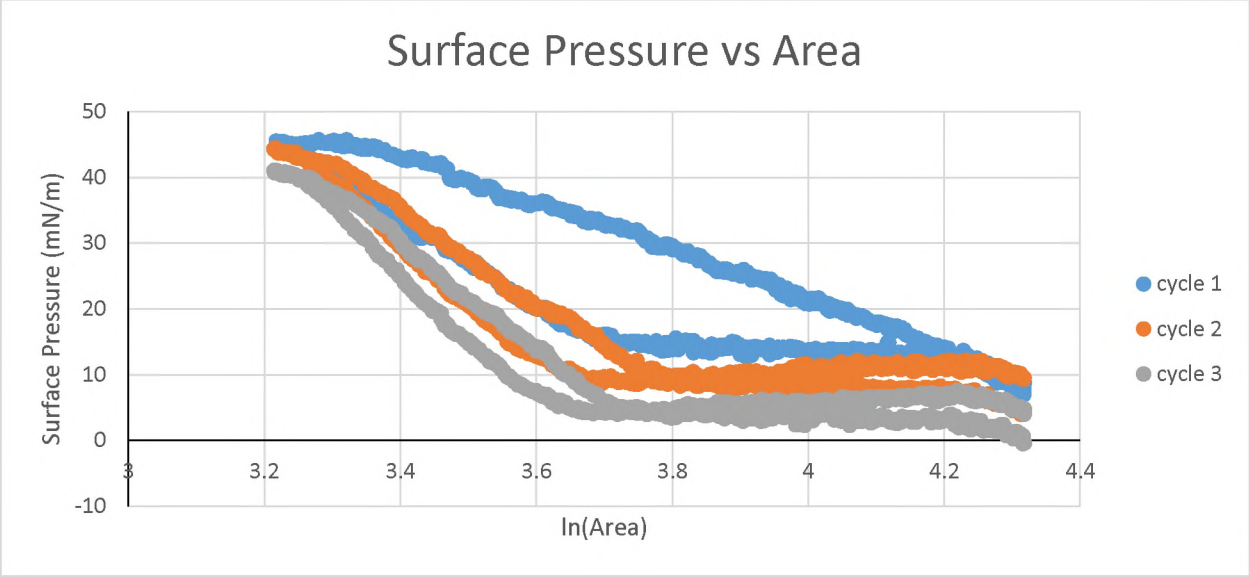

Figure 34.

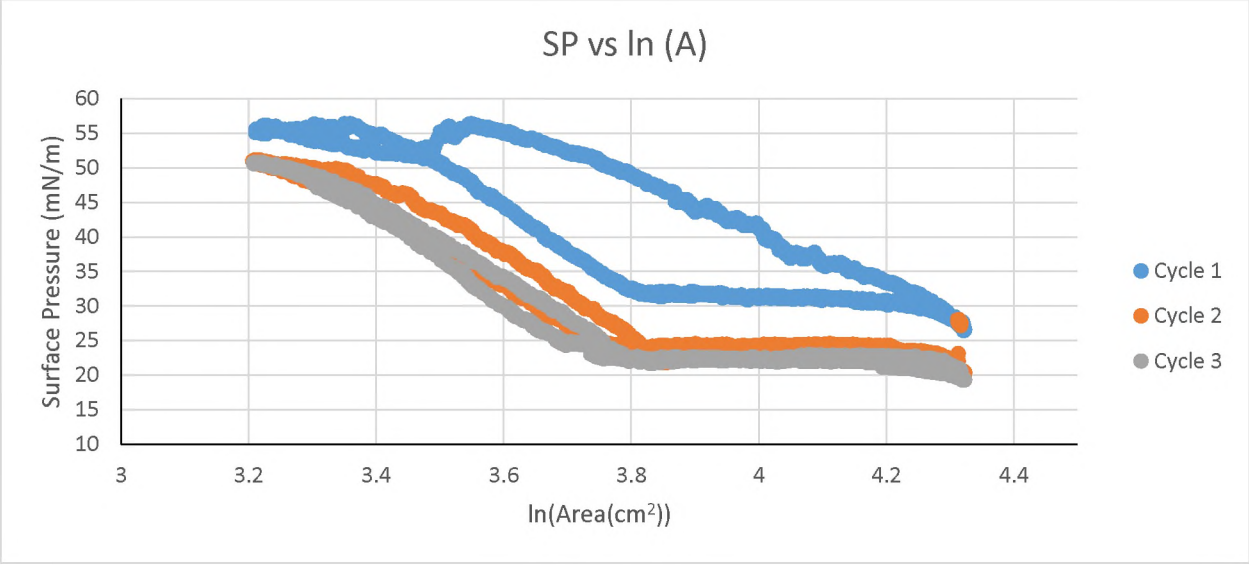

Figure 35.

40 minutes:

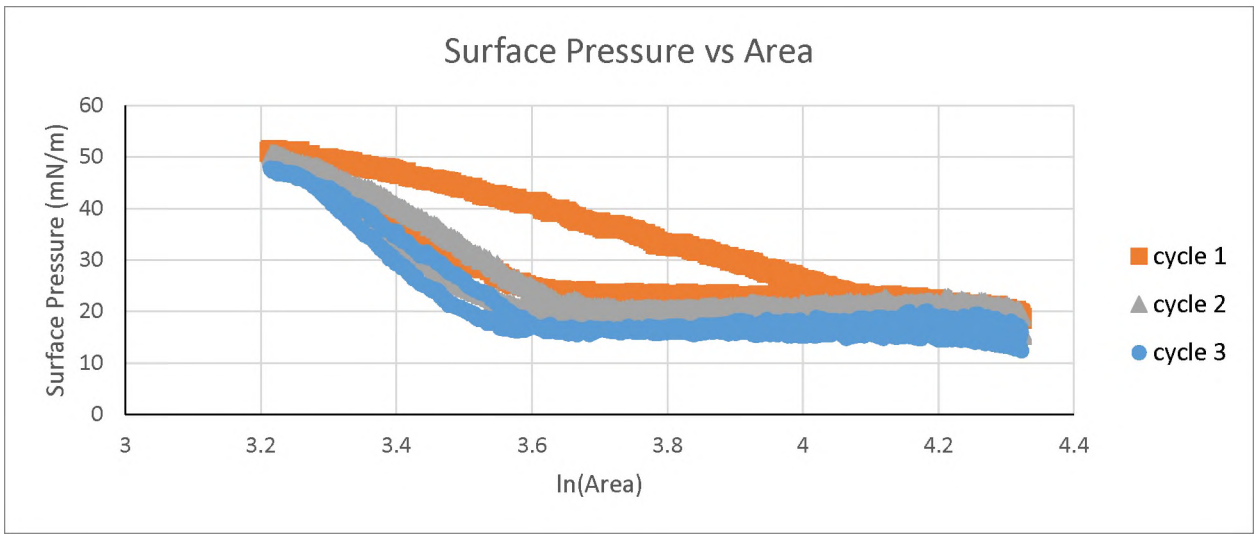

Figure 36.

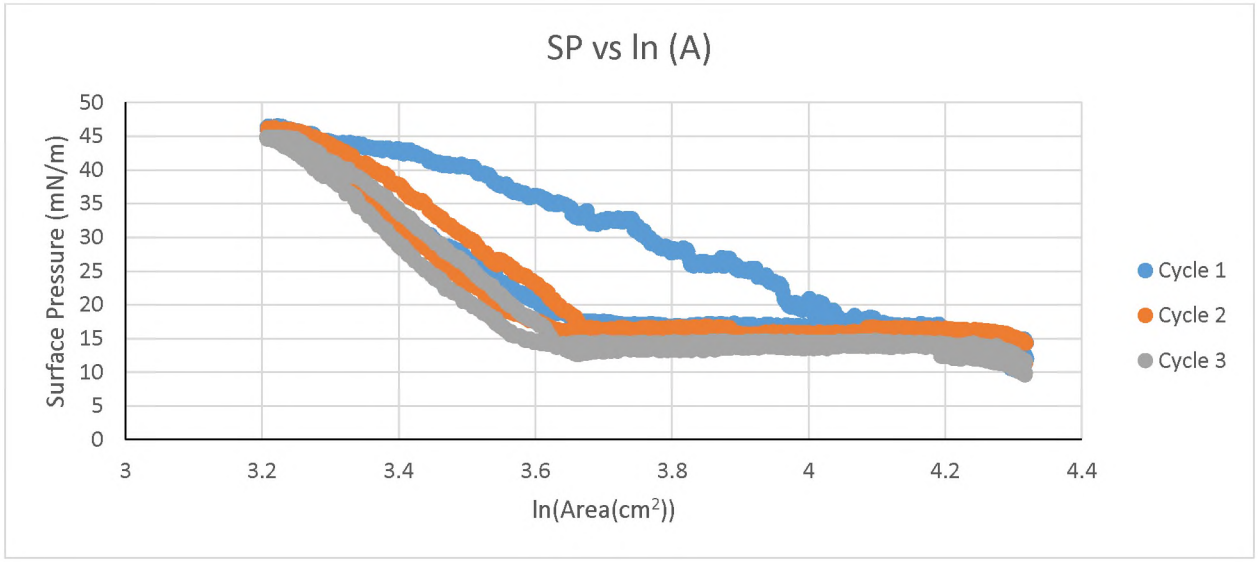

Figure 37.

1 hour:

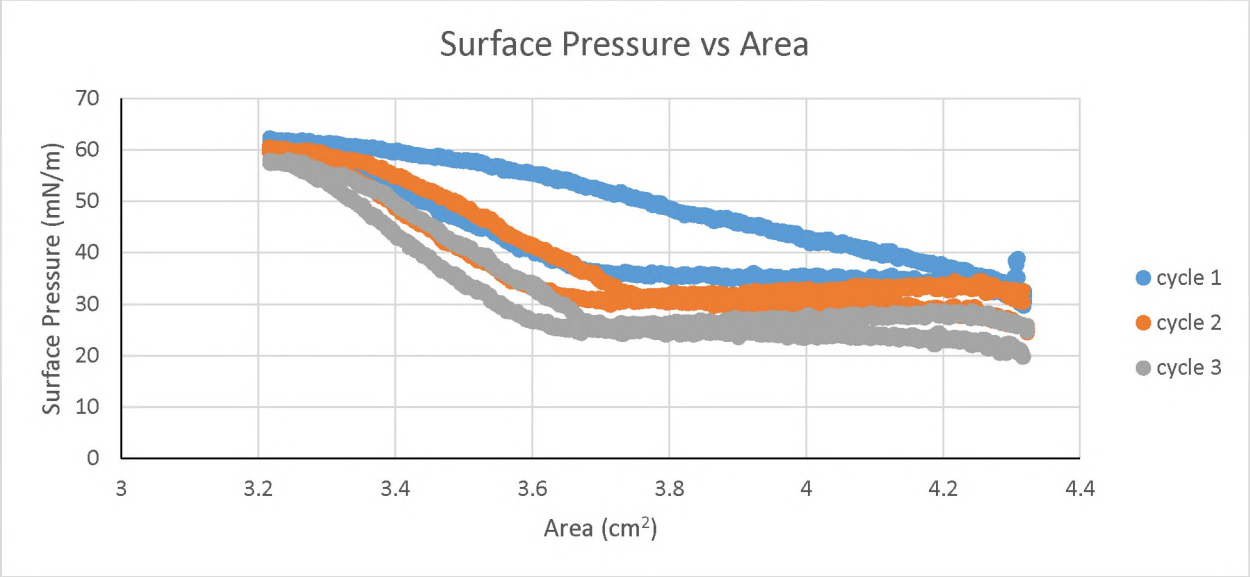

Figure 38.

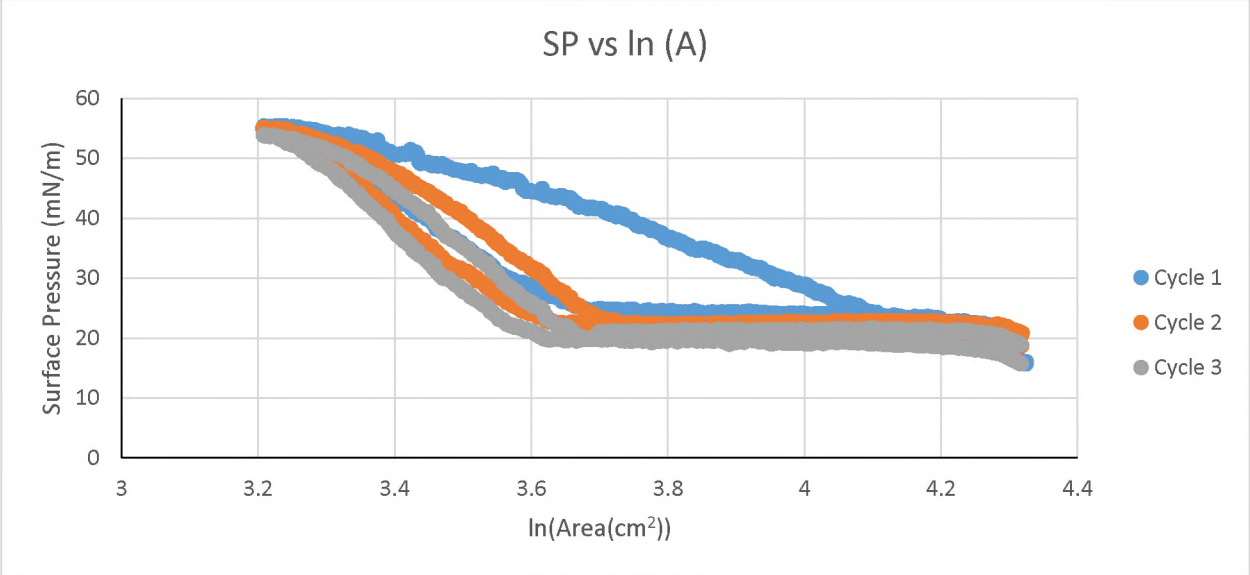

Figure 39.

2 hours:

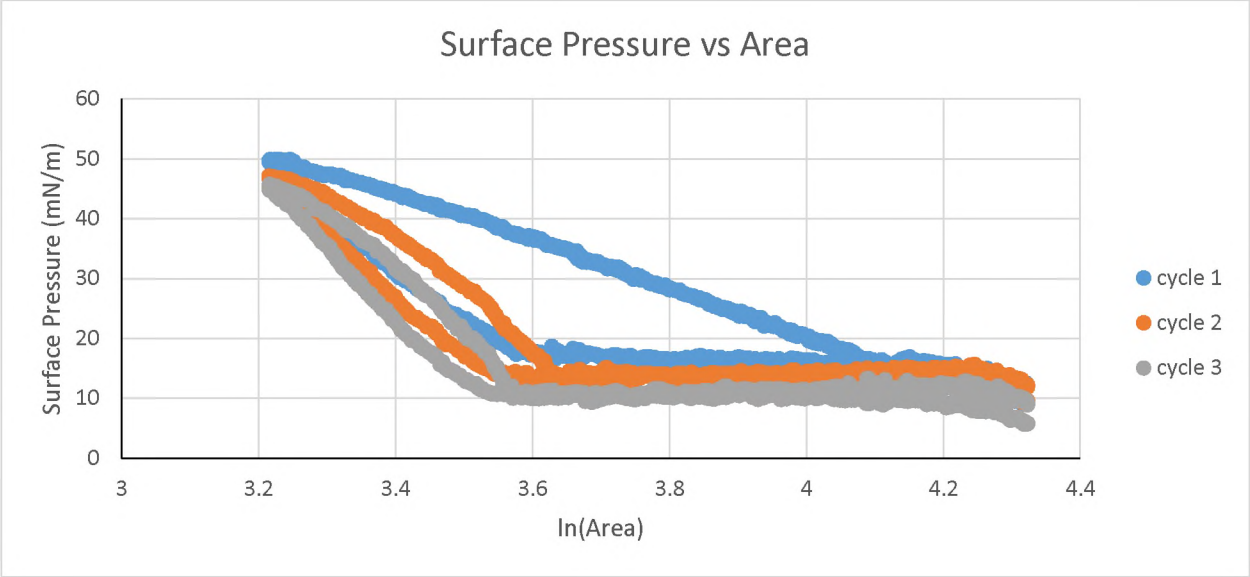

Figure 40.

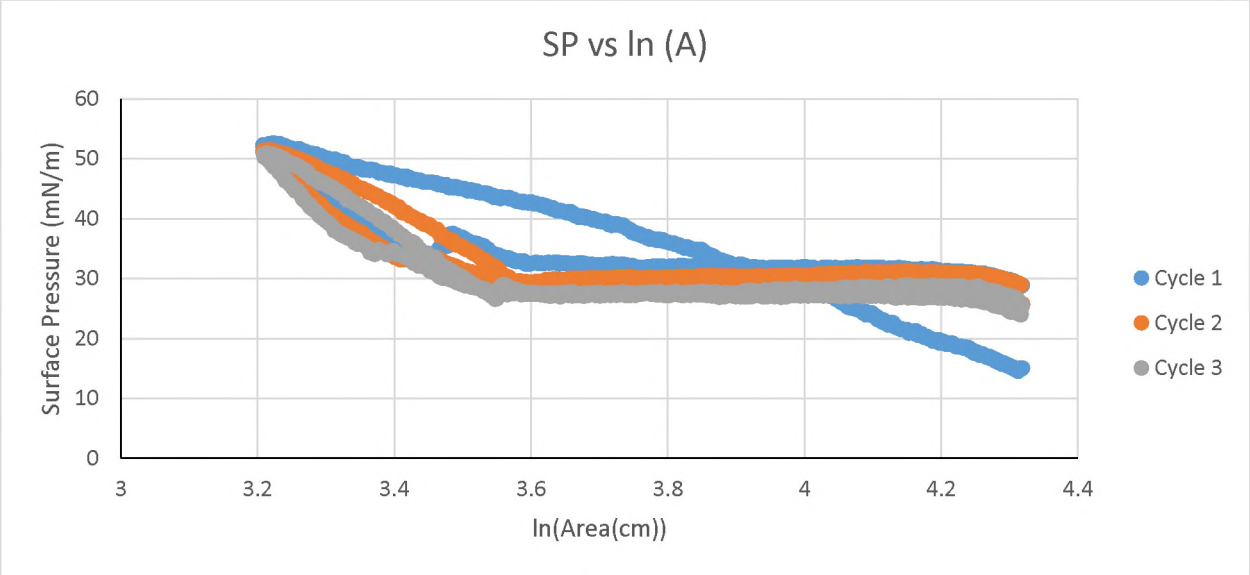

Figure 41.

4 hour:

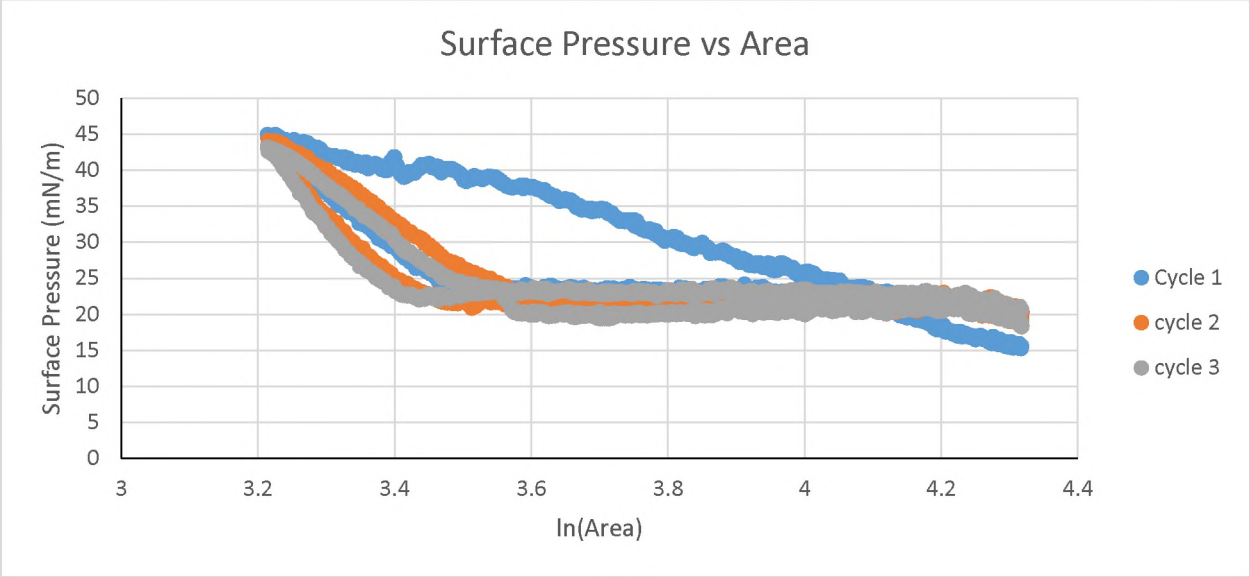

Figure 42.

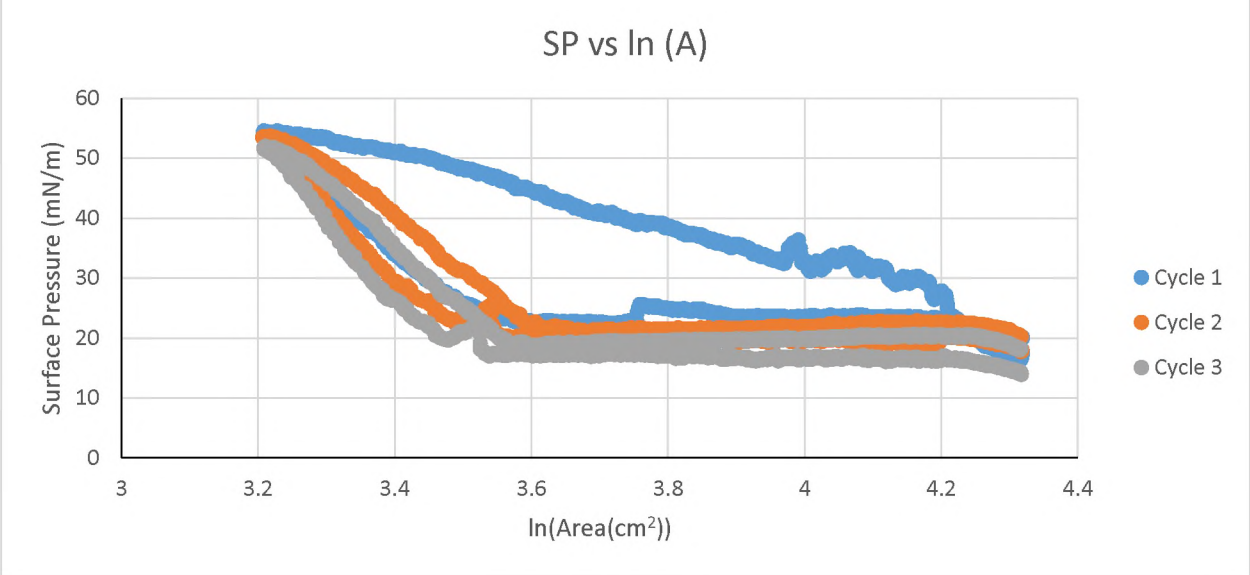

Figure 43.

6 hour:

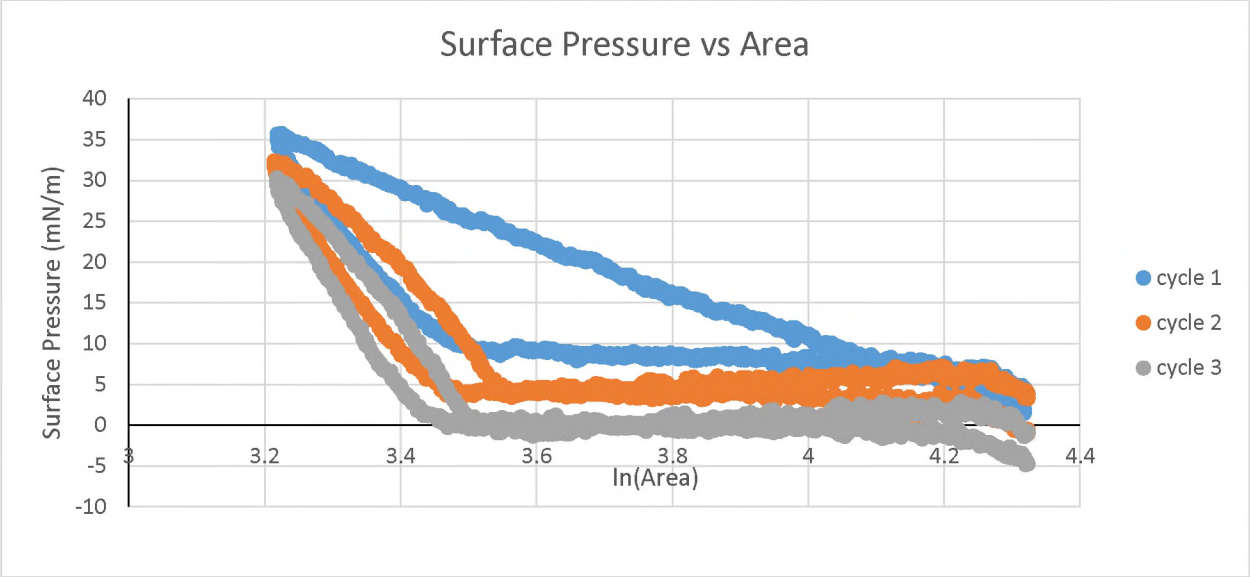

Figure 44.

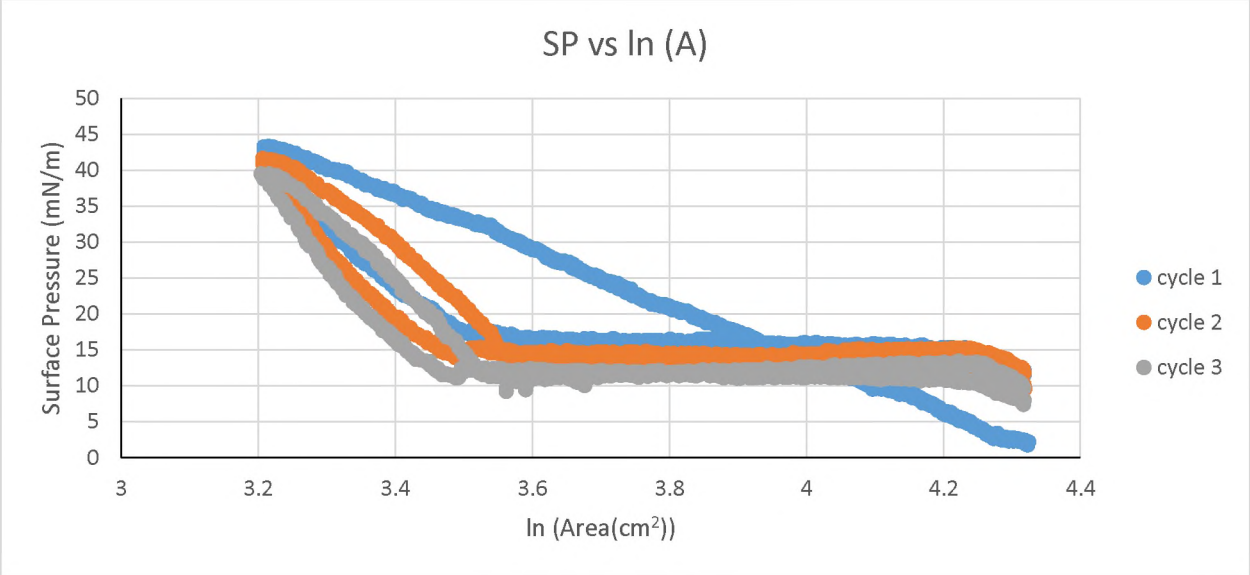

Figure 45.

20°C Temperature control:

Unmodified:

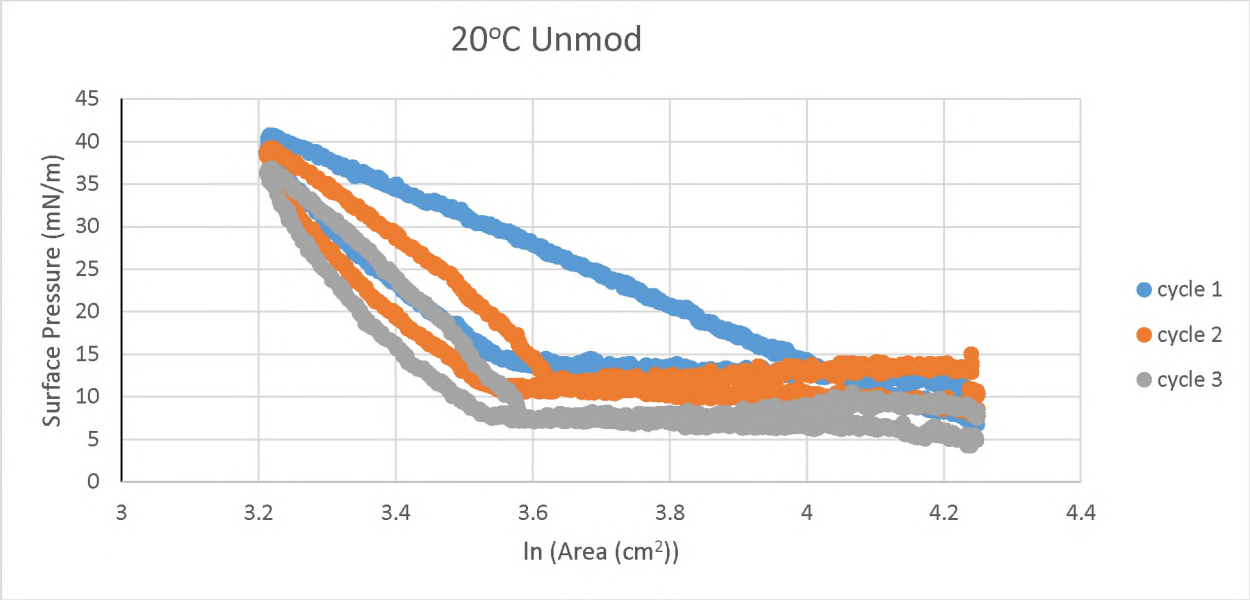

Figure 46.

40 minutes:

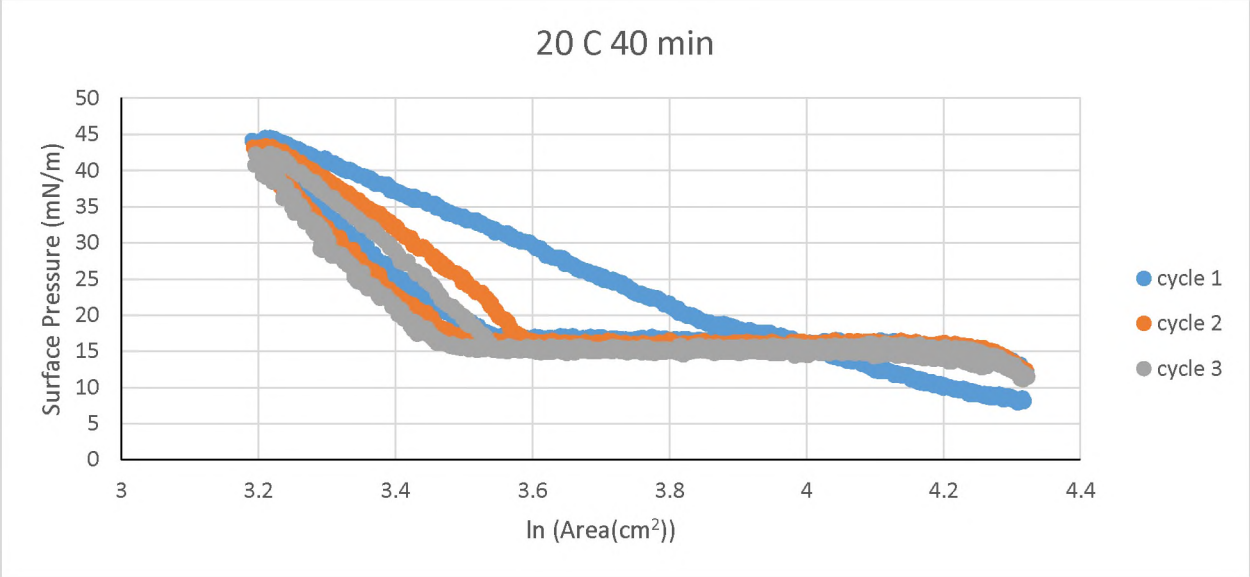

Figure 47.

1 hour:

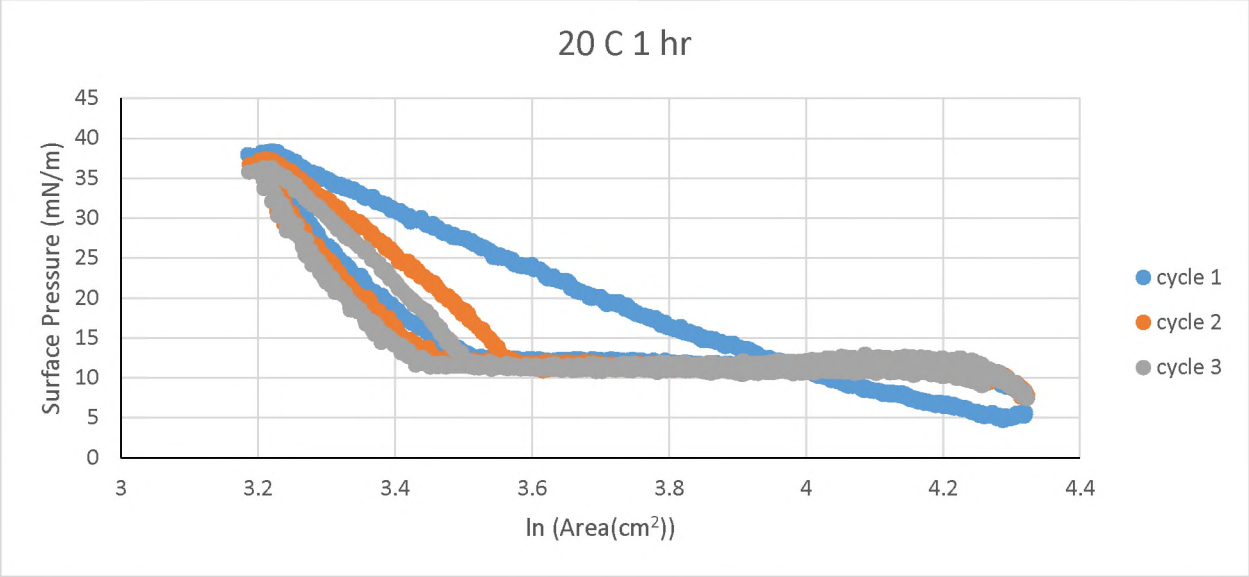

Figure 48.

2 hour:

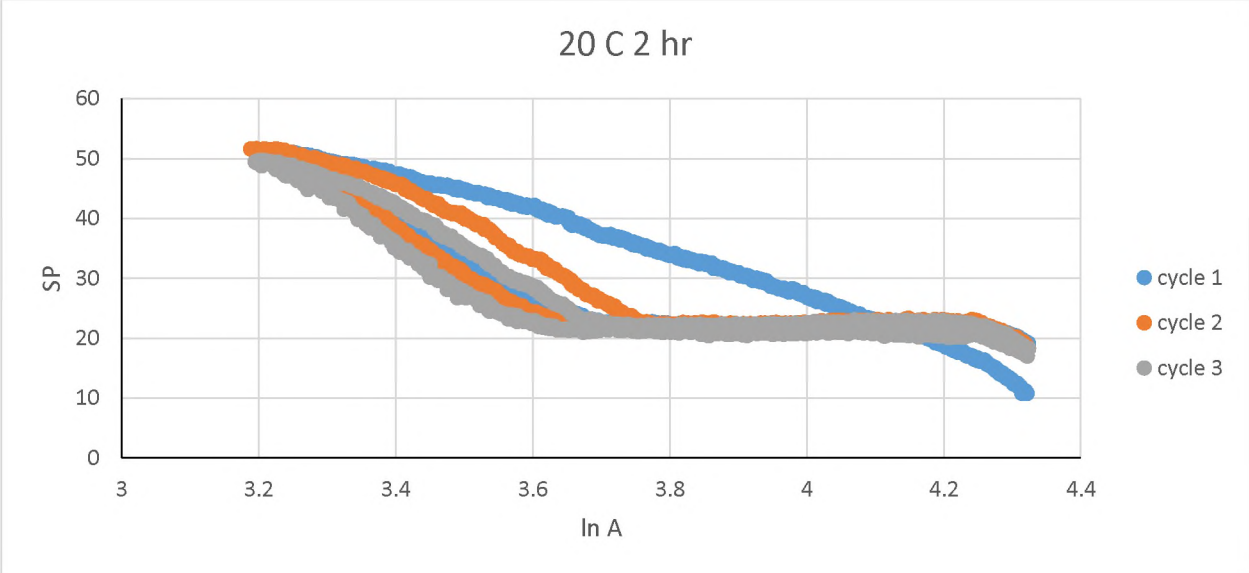

Figure 49.

4 hour:

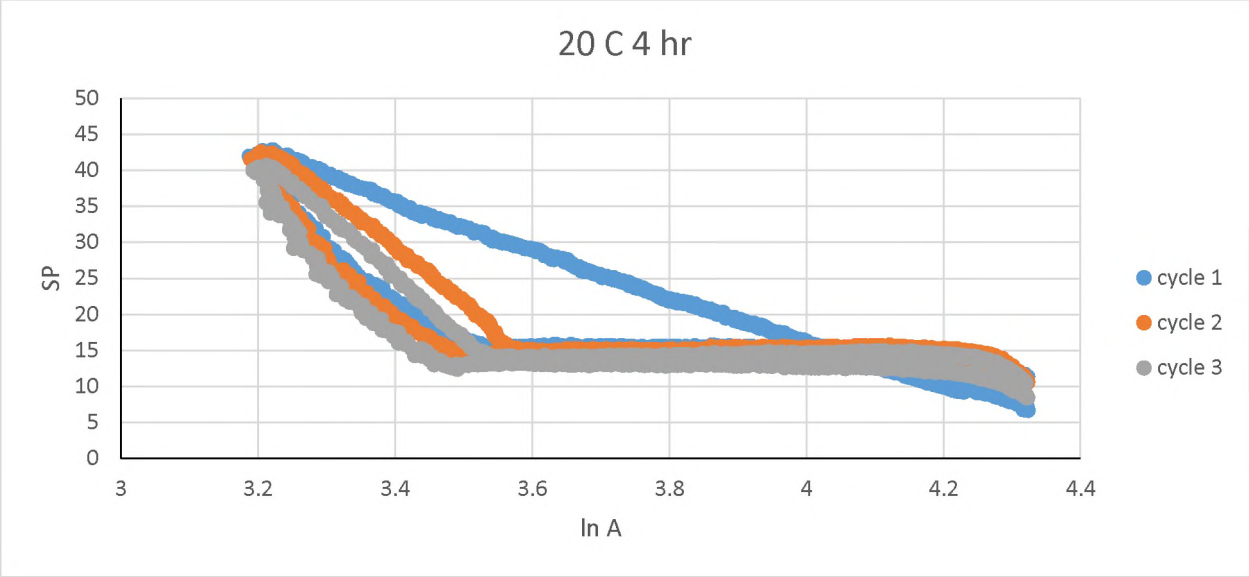

Figure 50.

6 hour:

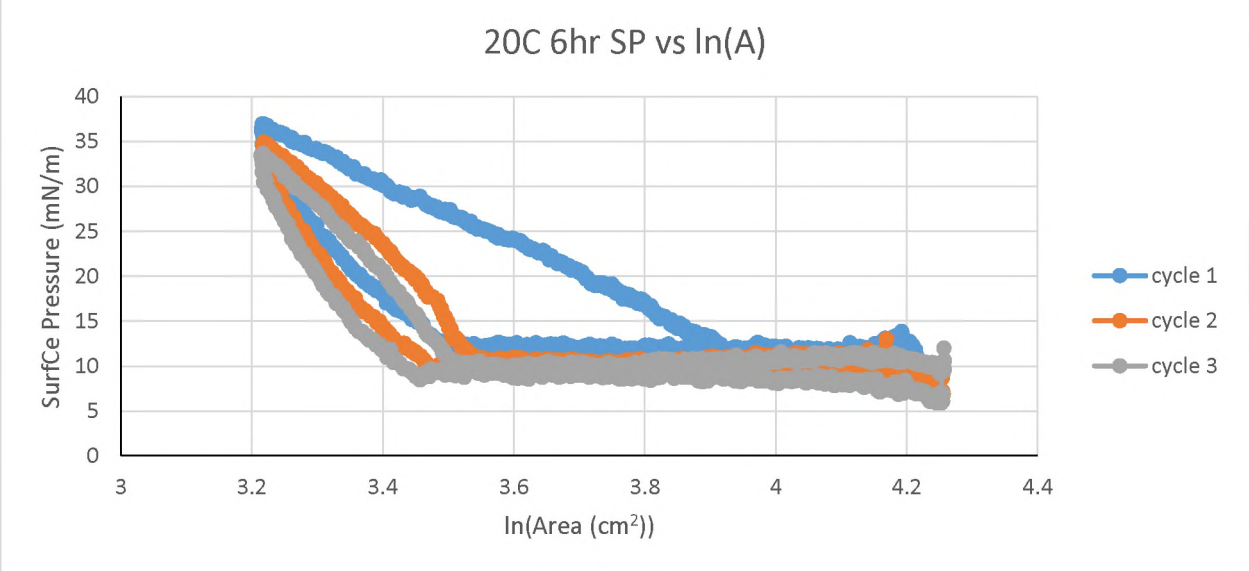

Figure 51.

25°C Temperature control:

Unmodified:

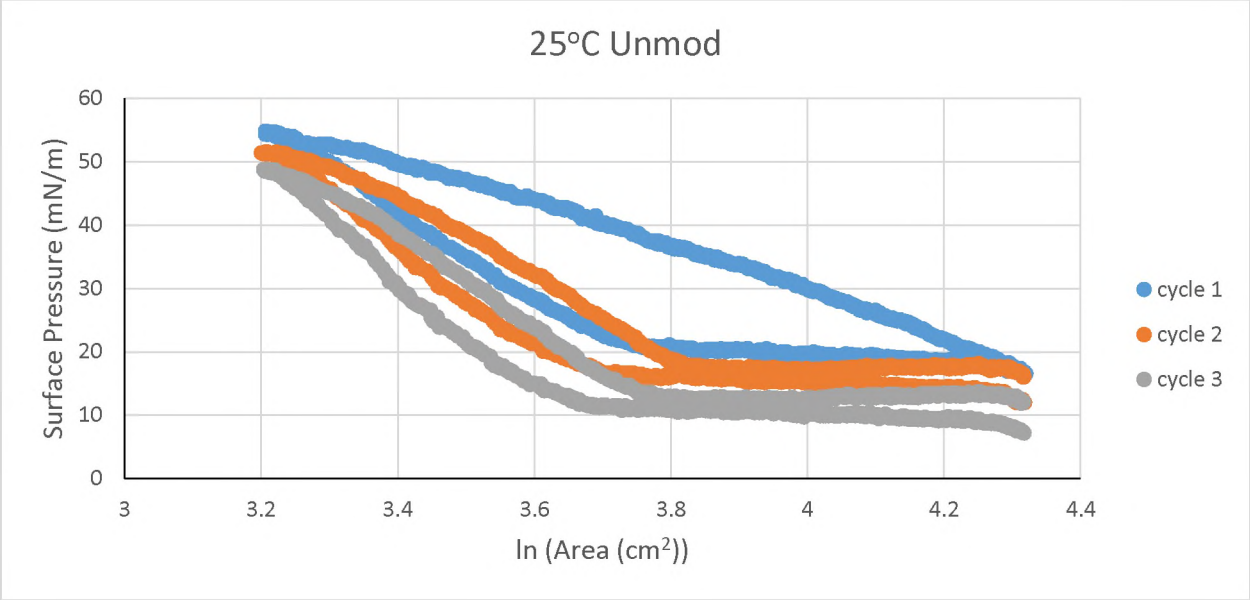

Figure 52.

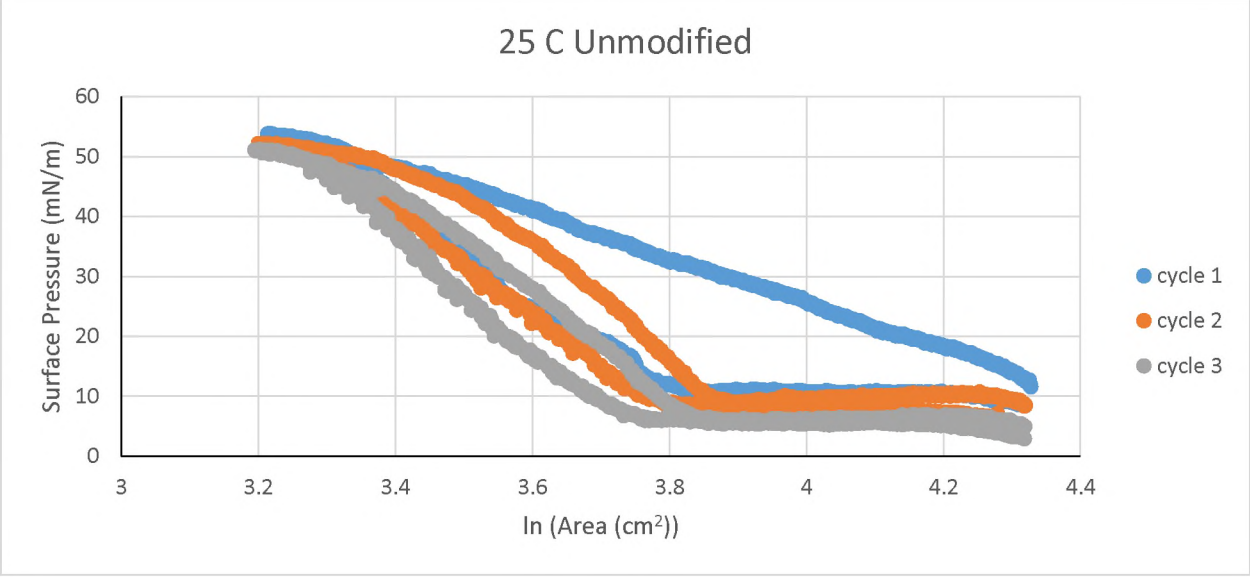

Figure 53.

40 minutes:

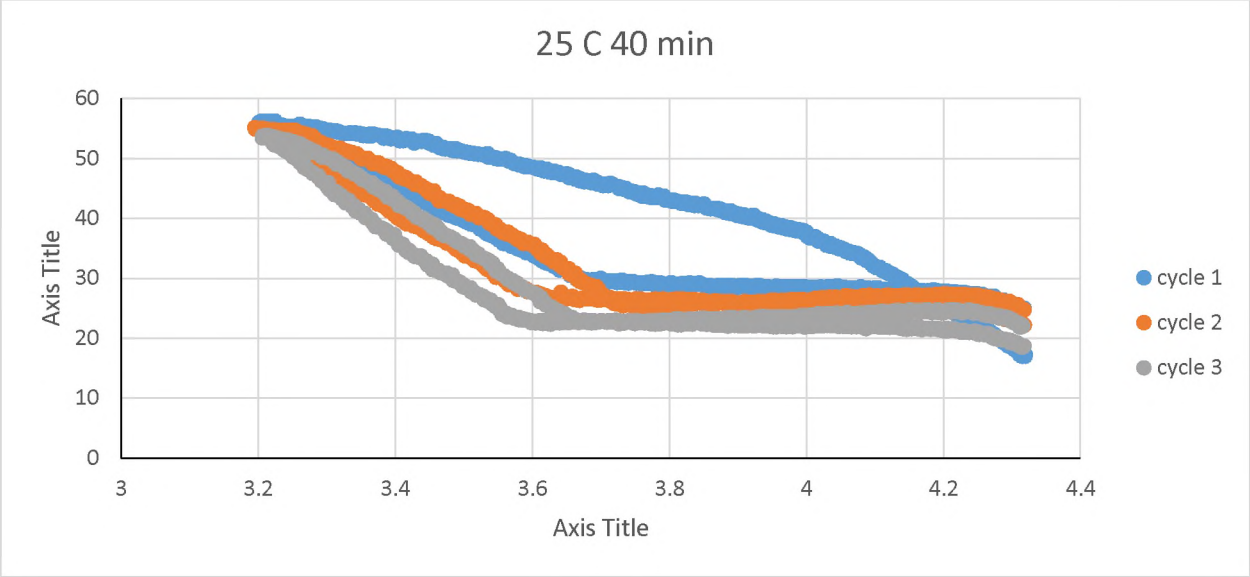

Figure 54.

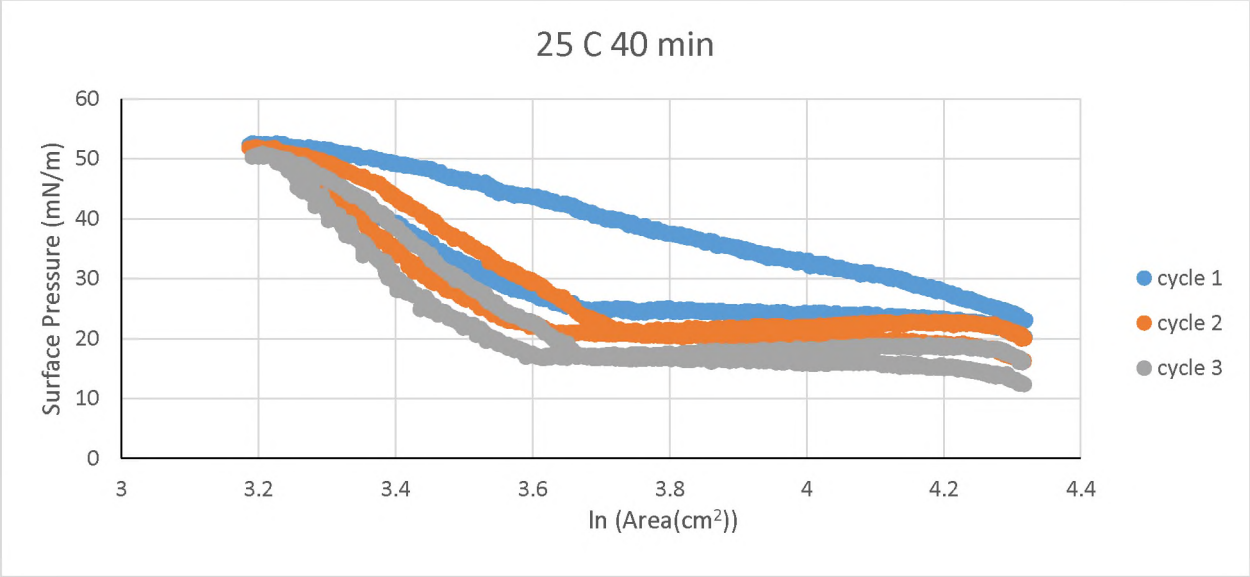

Figure 55.

1 hour:

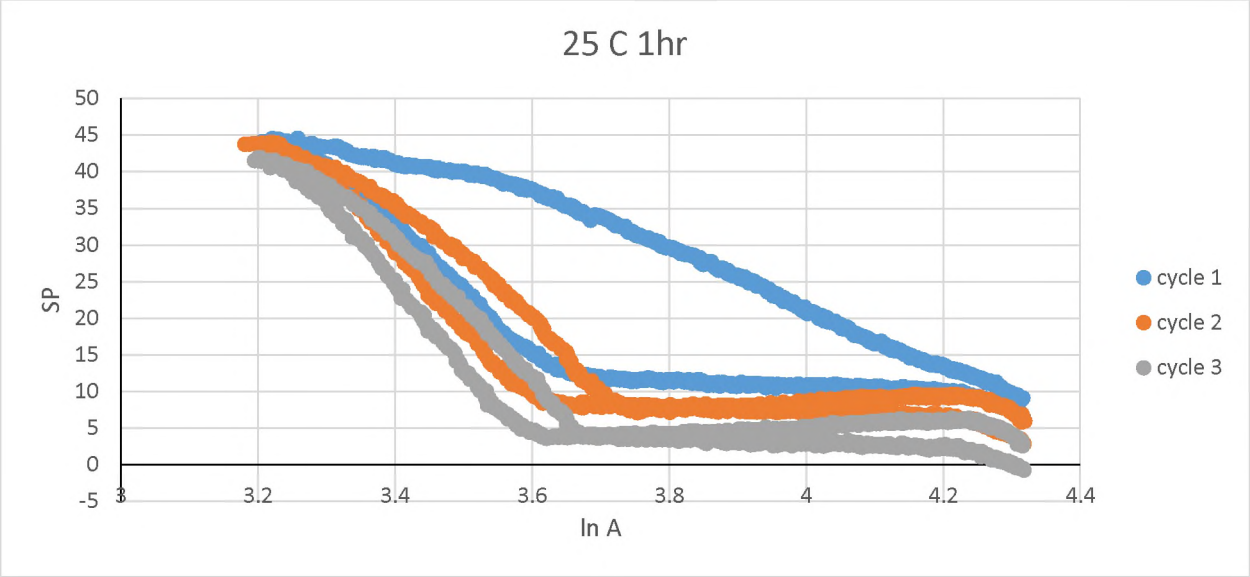

Figure 56.

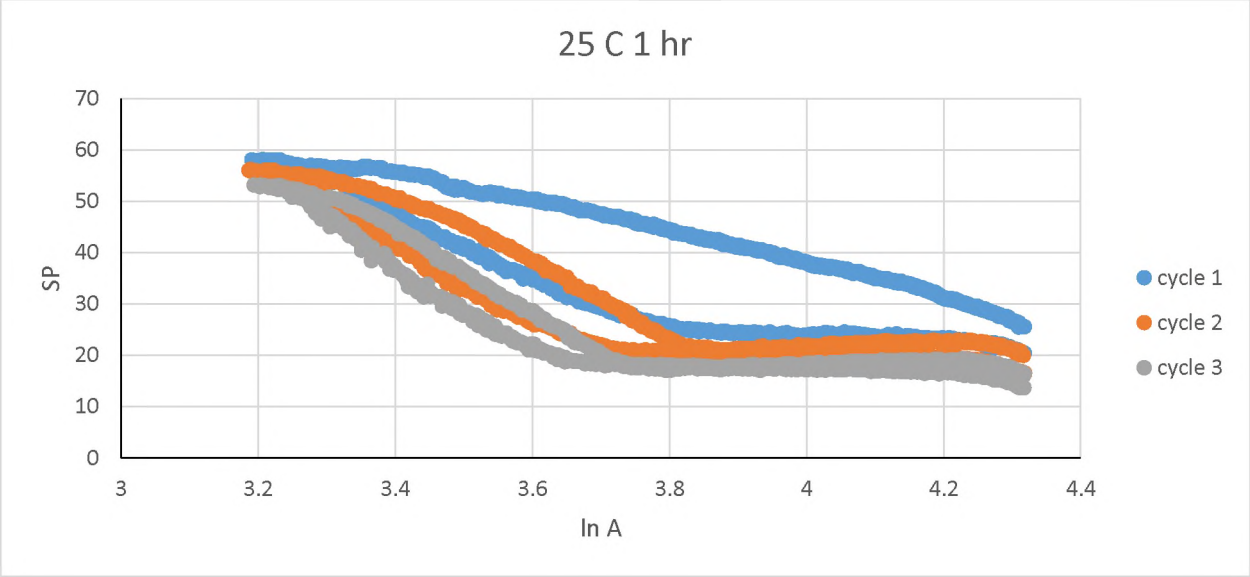

Figure 57.

2 hour:

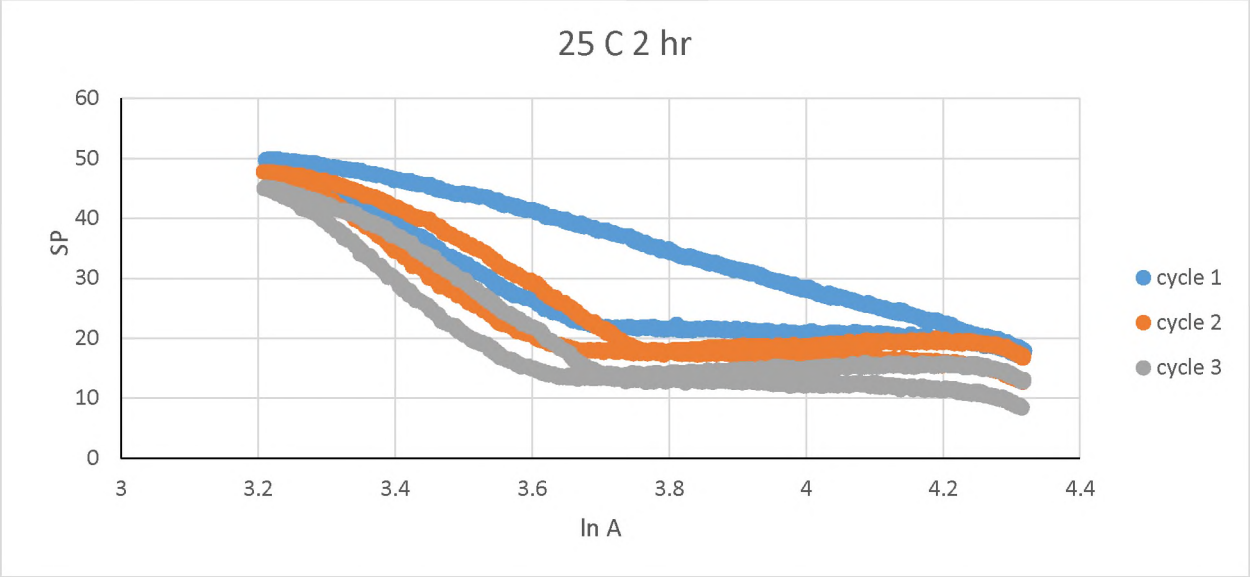

Figure 58.

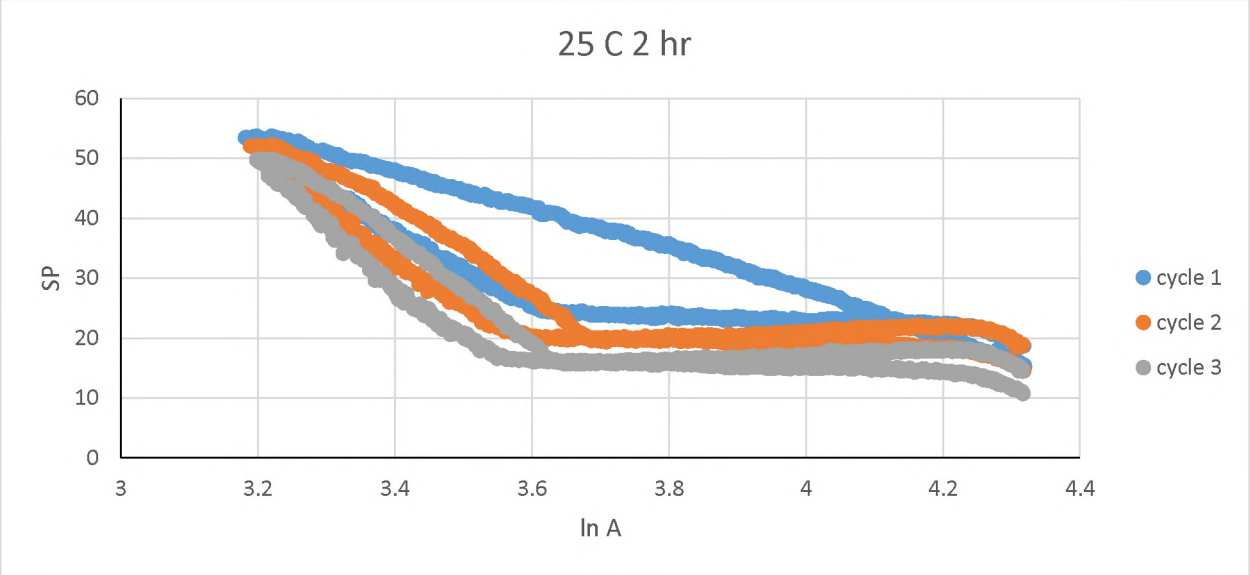

Figure 59.

4 hour:

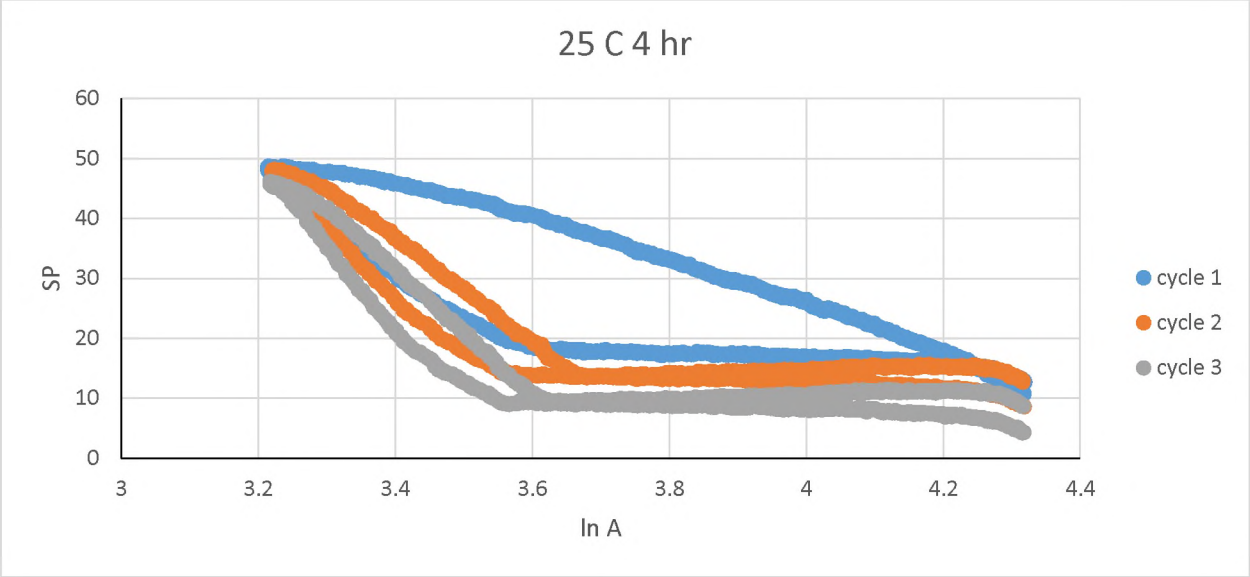

Figure 60.

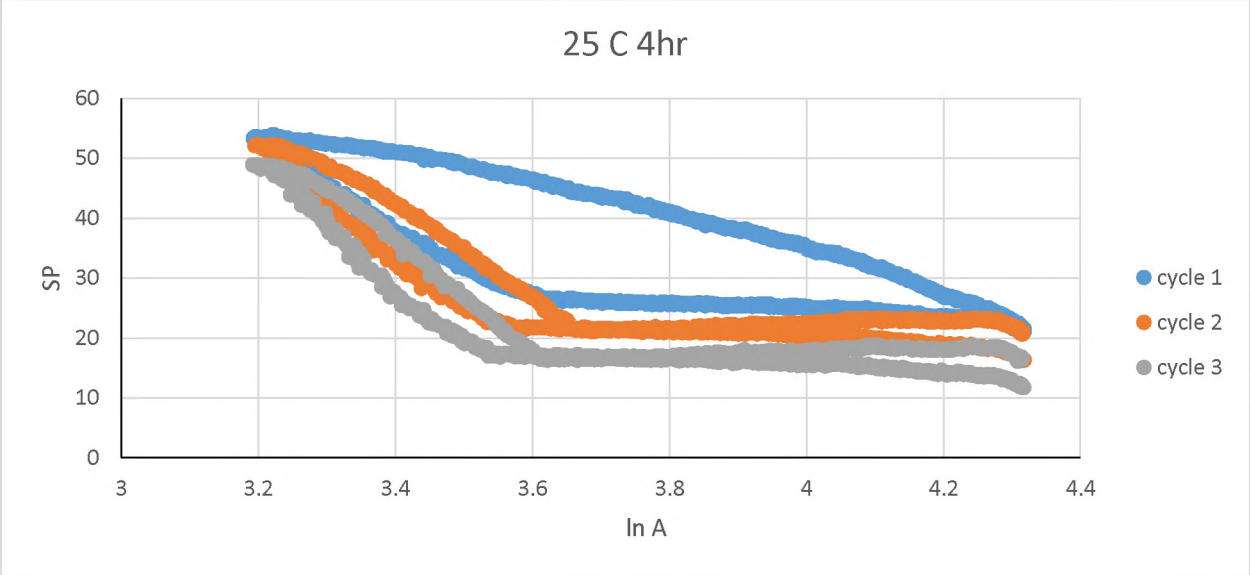

Figure 61.

6 hour:

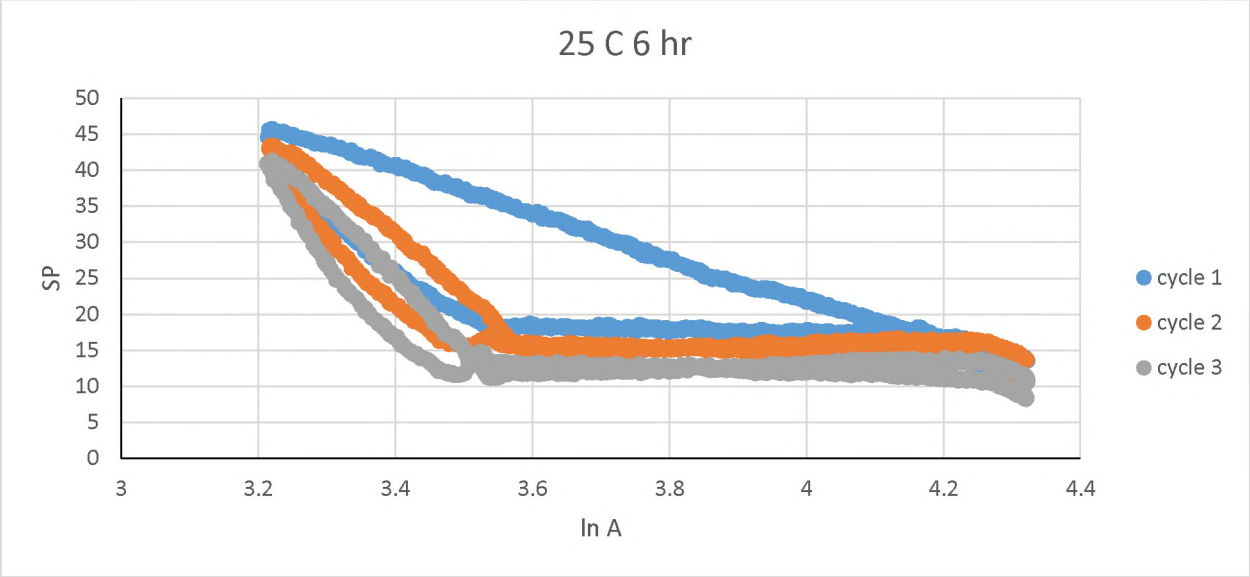

Figure 62.

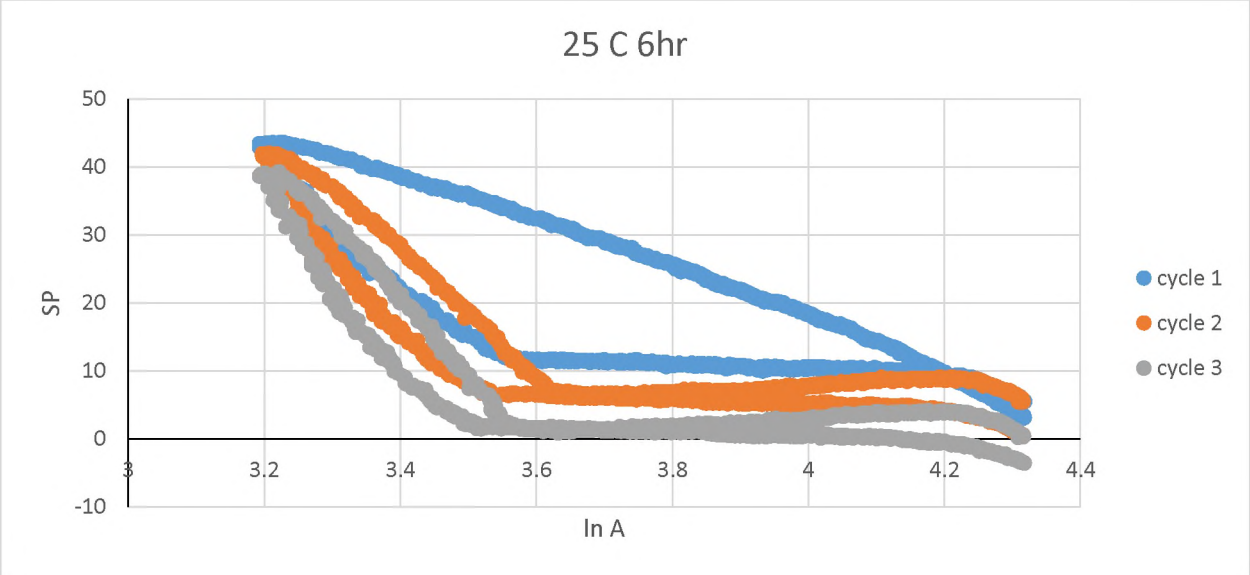

Figure 63.

30°C Temperature control:

Unmodified:

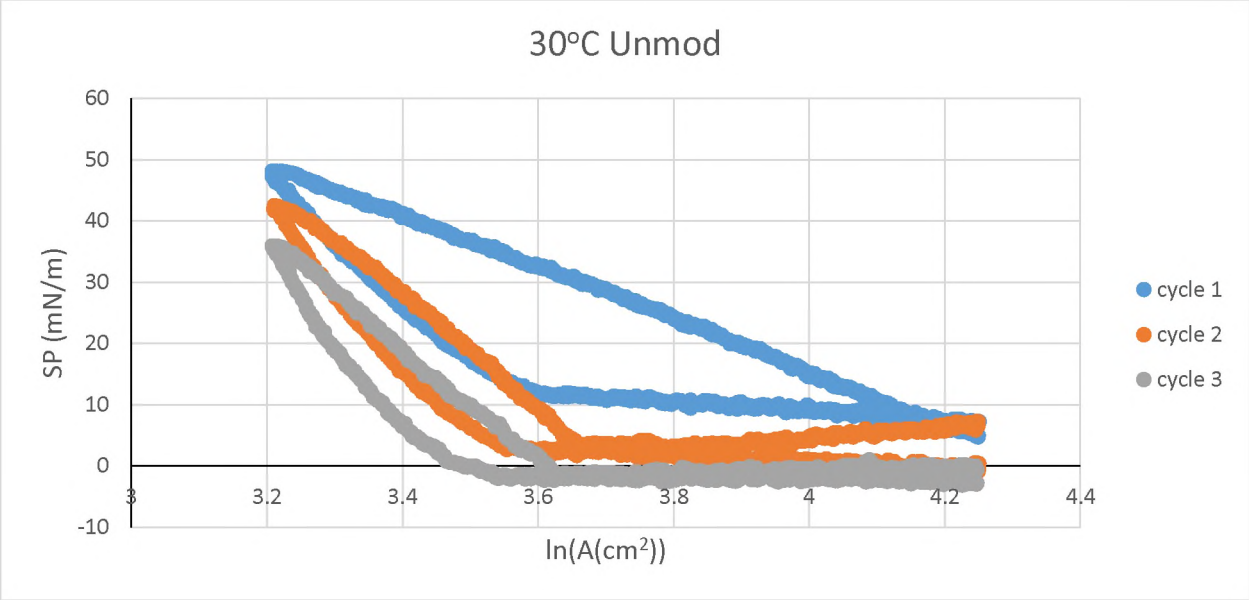

Figure 64.

40 minute:

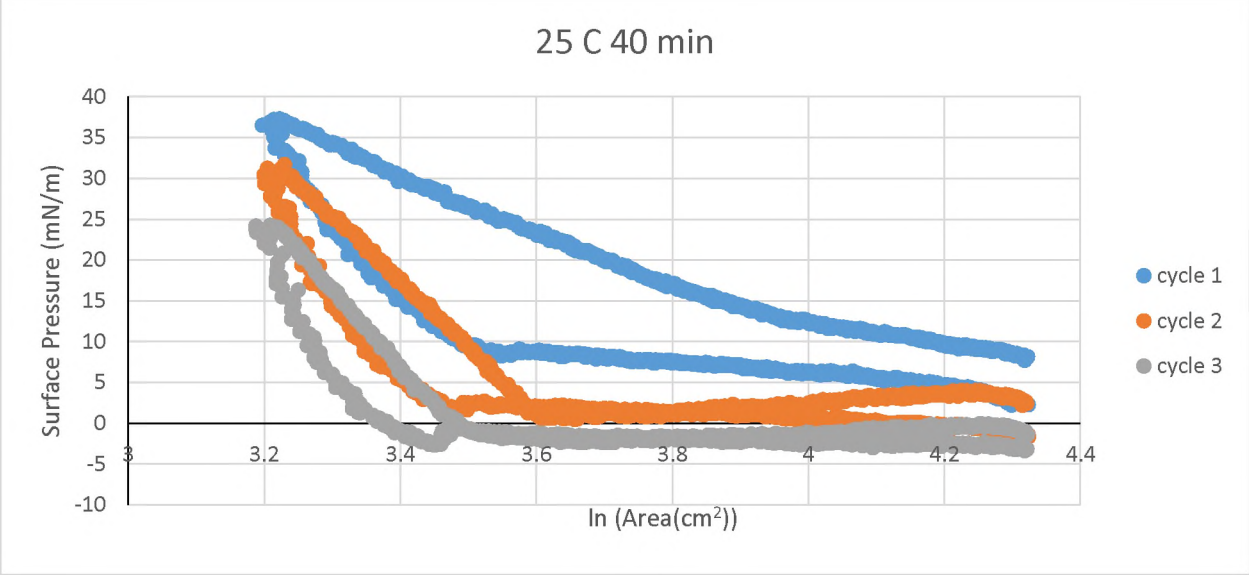

Figure 65.

1 hour:

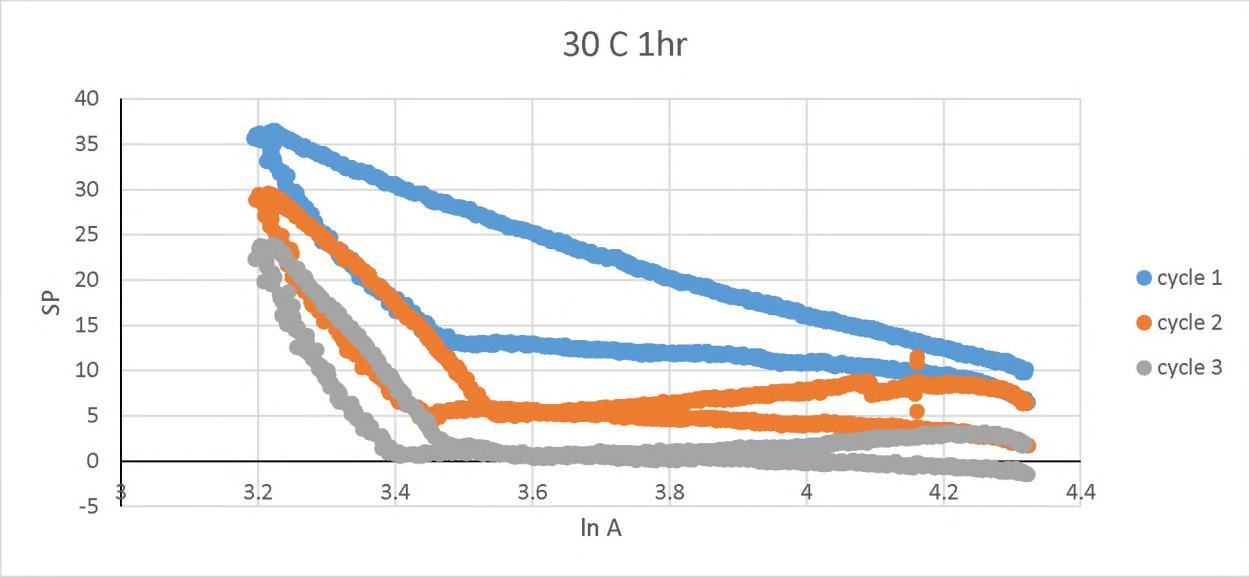

Figure 66.

2 hour:

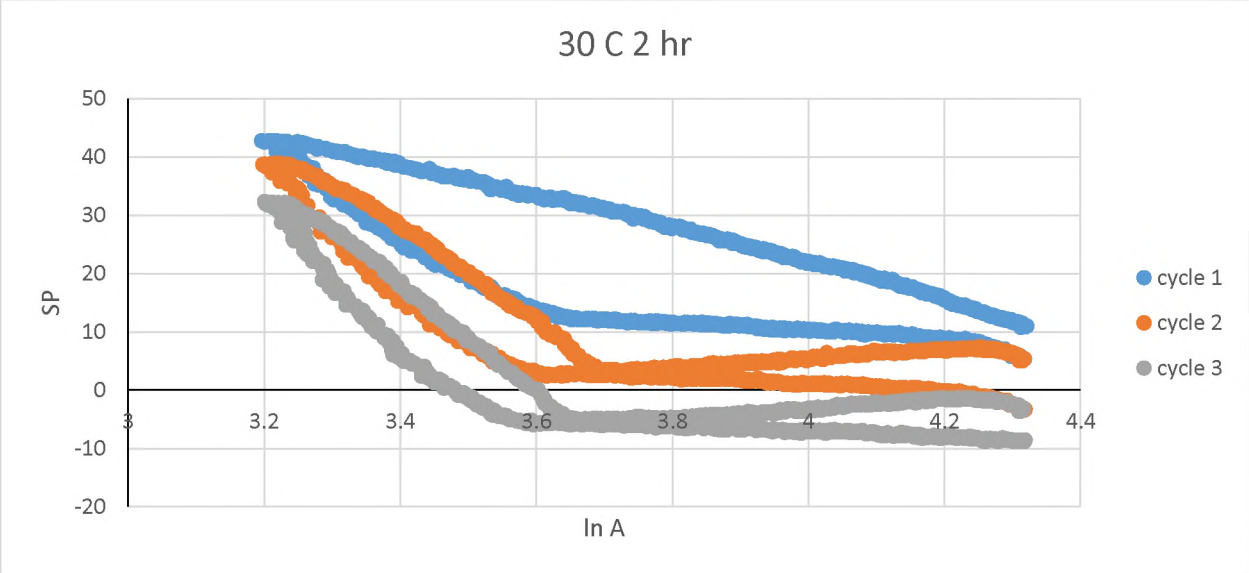

Figure 67.

4 hour:

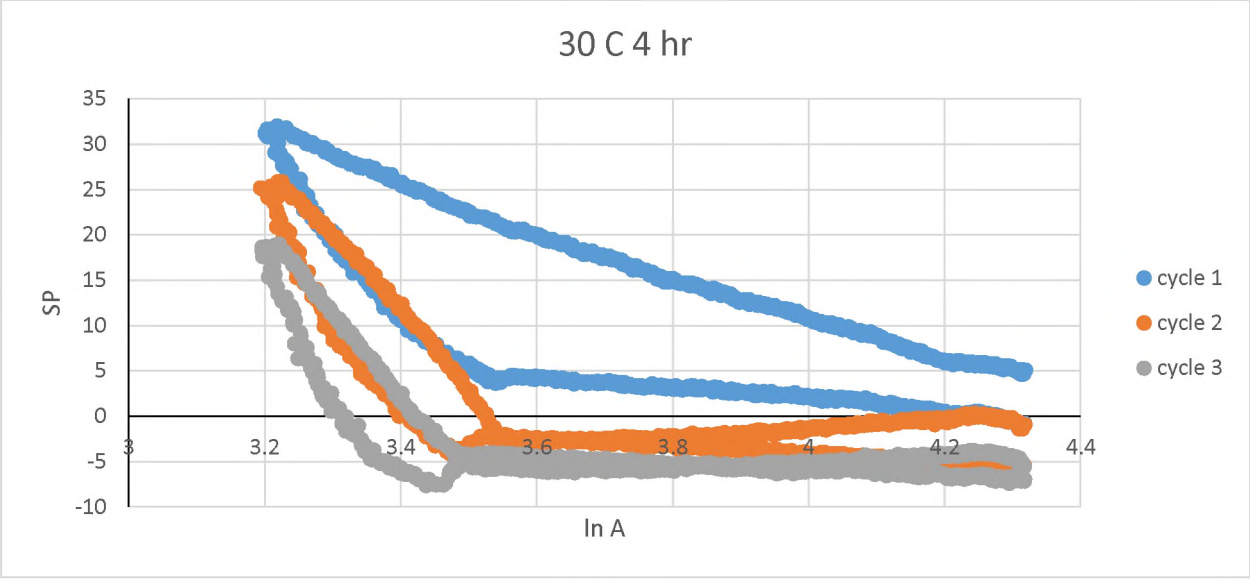

Figure 68.

6 hour:

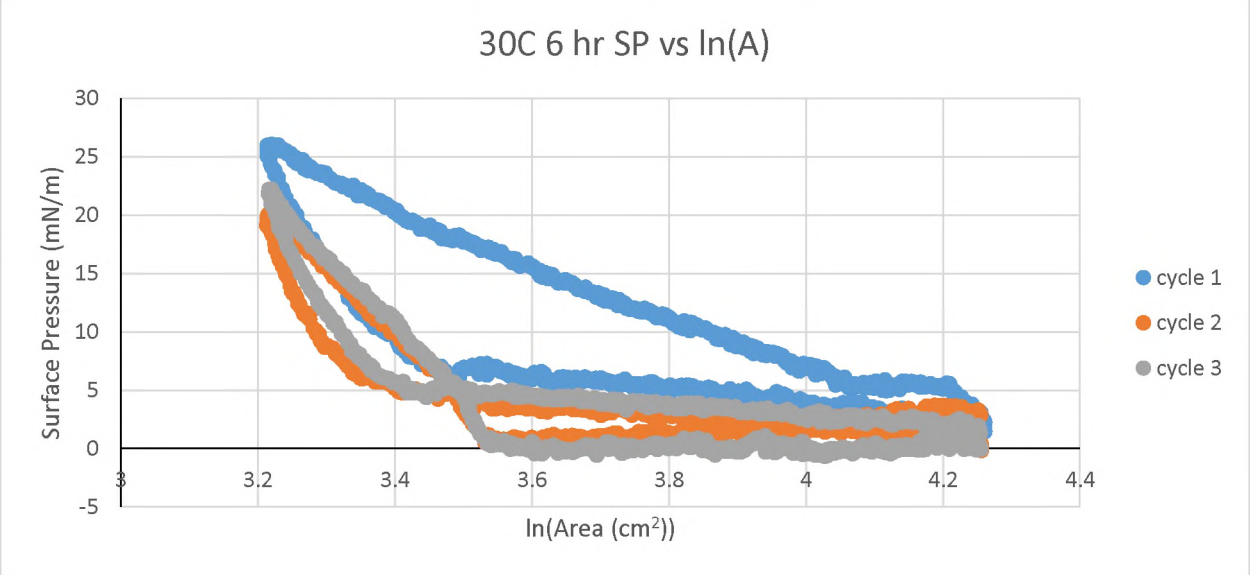

Figure 69.

APPENDIX C.

(Elasticity Data)

Room Temperature:

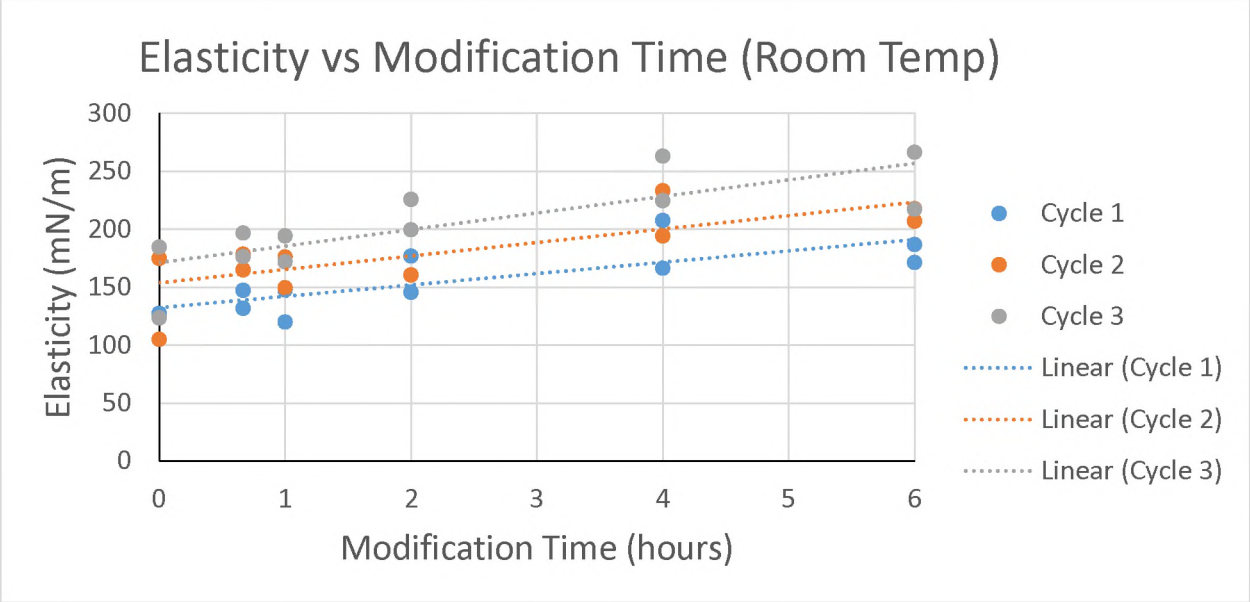

Figure 70.

20°C:

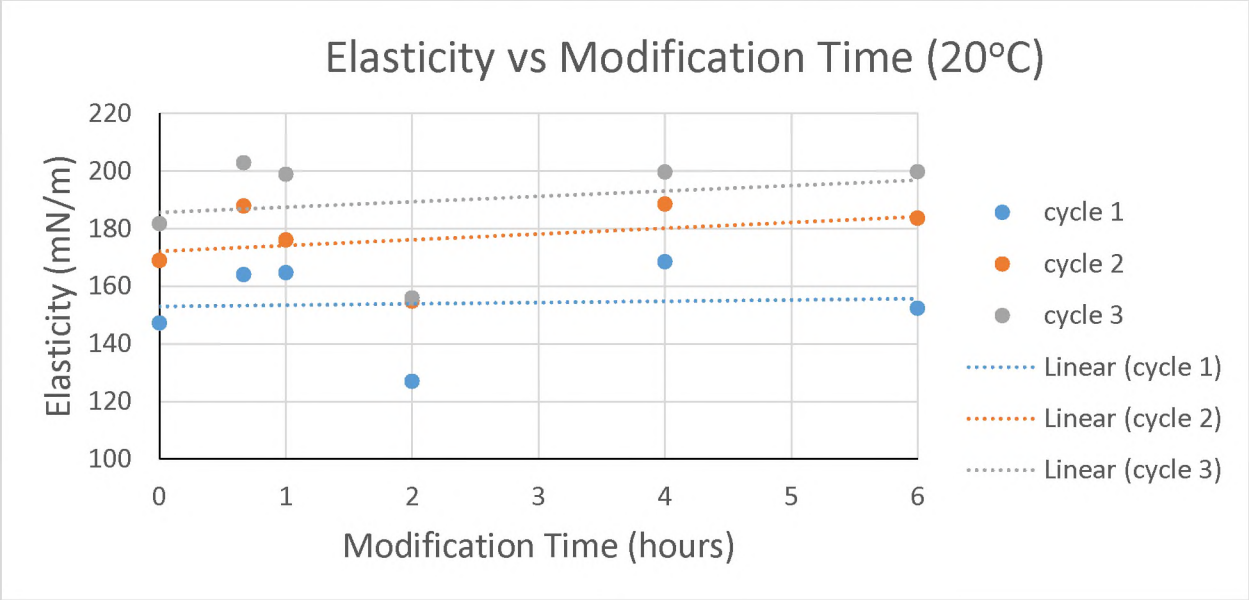

Figure 71.

25°C:

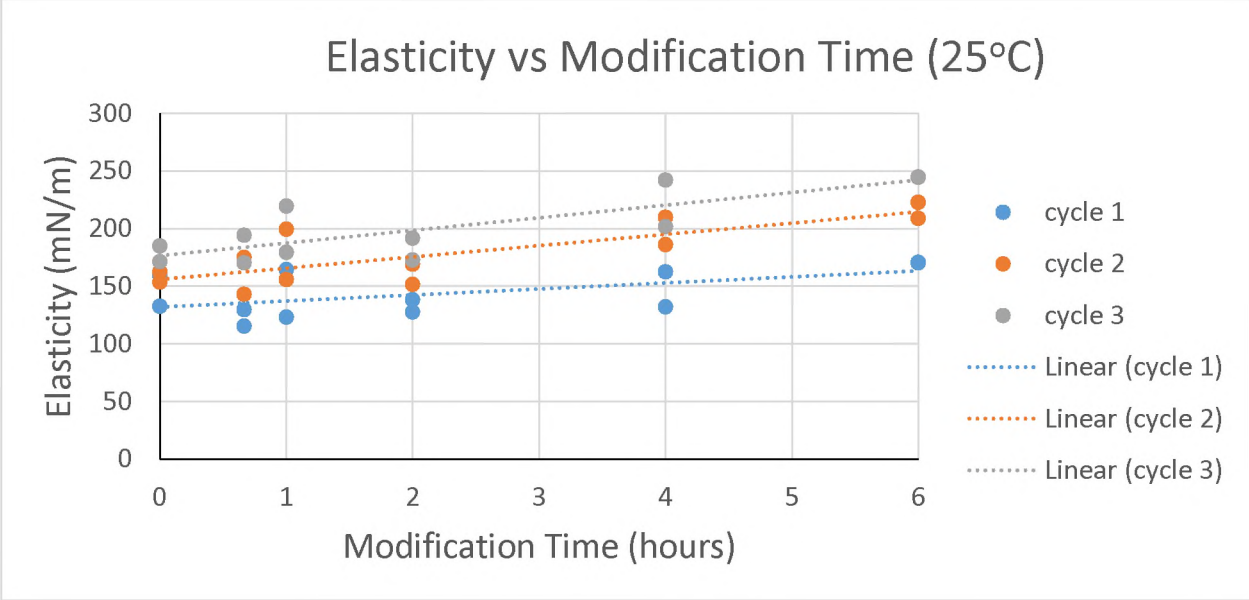

Figure 72.

30°C:

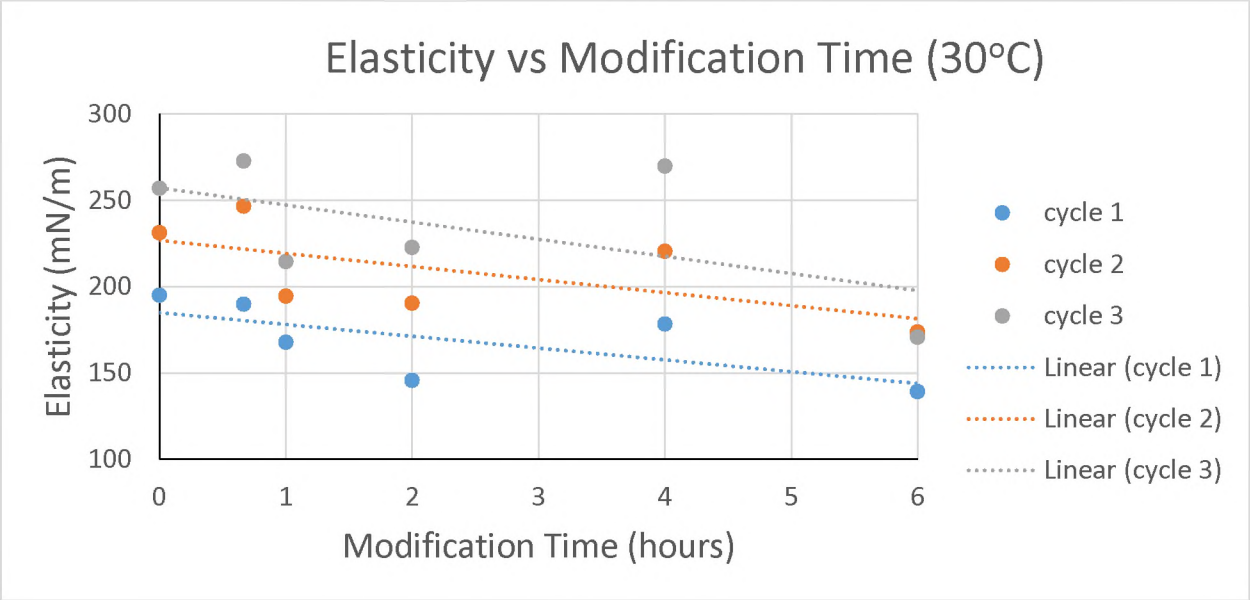
Elasticity vs Modification Time (30°C)
Elasticity (mN/m)
300
250
200
150
100
0
1
2
3
4
5
6
Modification Time (hours)
cycle 1
cycle 2
cycle 3
Linear (cycle 1)
Linear (cycle 2)
Linear (cycle 3)

Figure 73.

APPENDIX D.

(Optical Microscopy)

Unmodified:

40 cm^2:

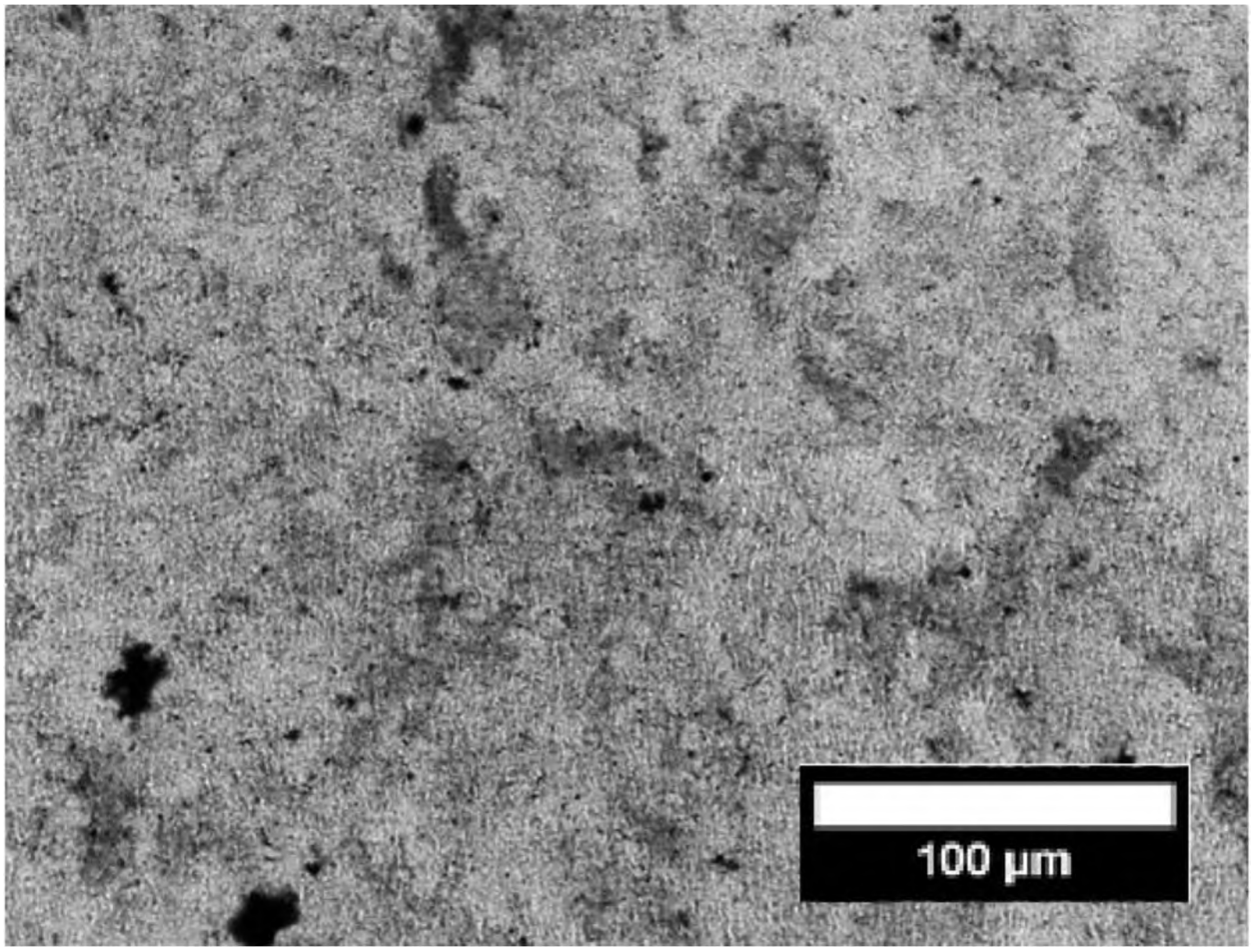

Figure 74.

35 cm^2:

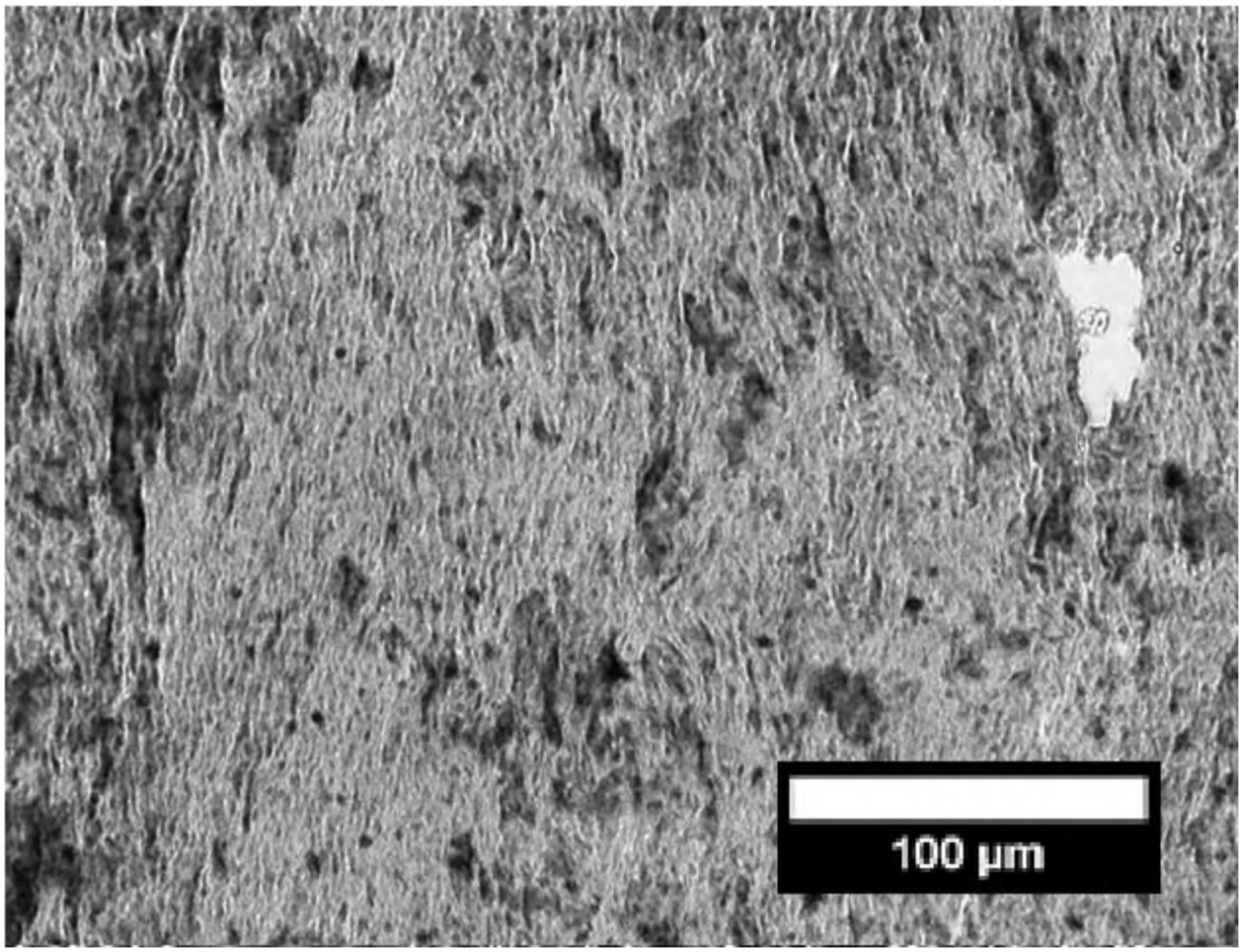

Figure 75.

30 cm^2:

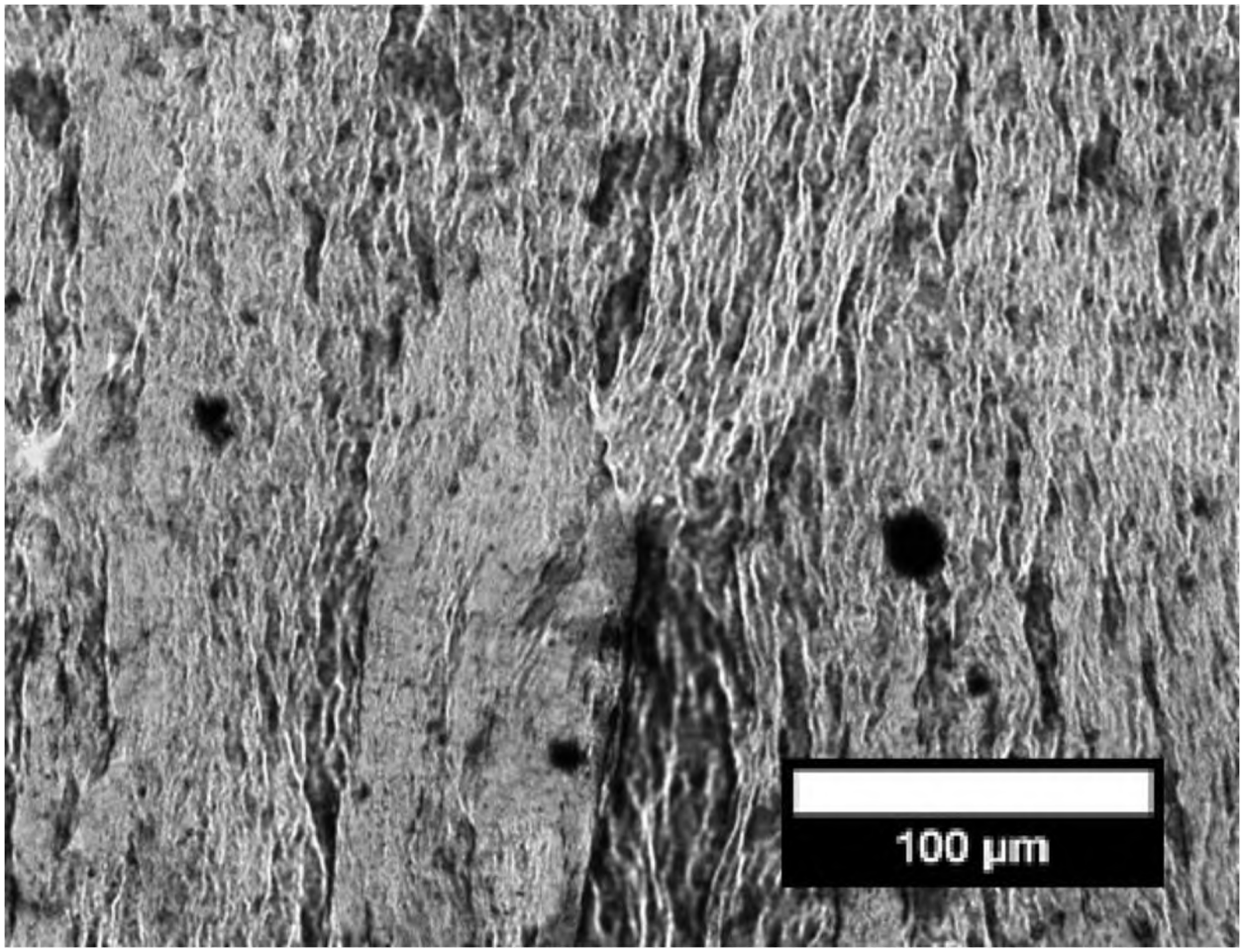

Figure 76.

25 cm^2:

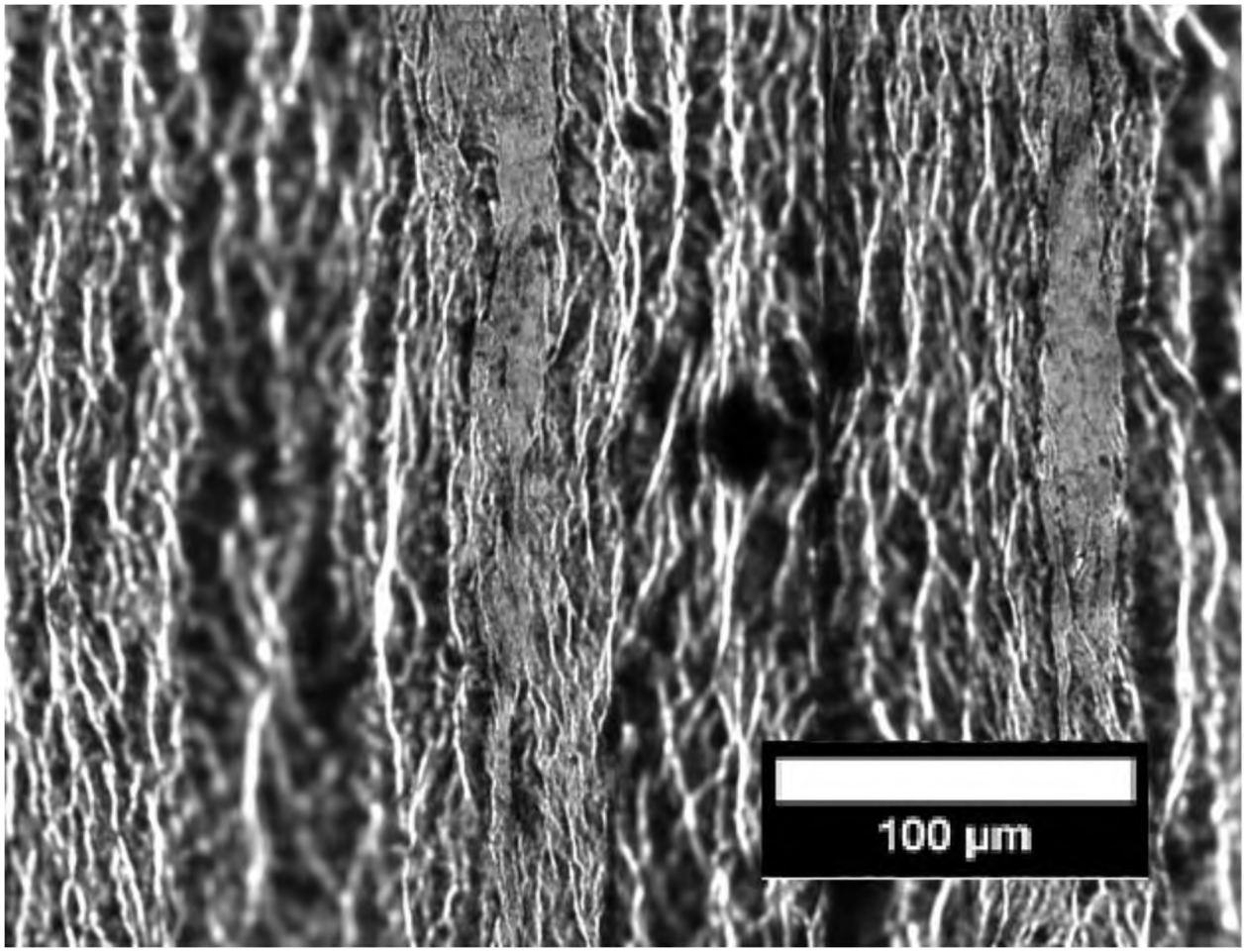

Figure 77.

2-hour modification:

40 cm^2:

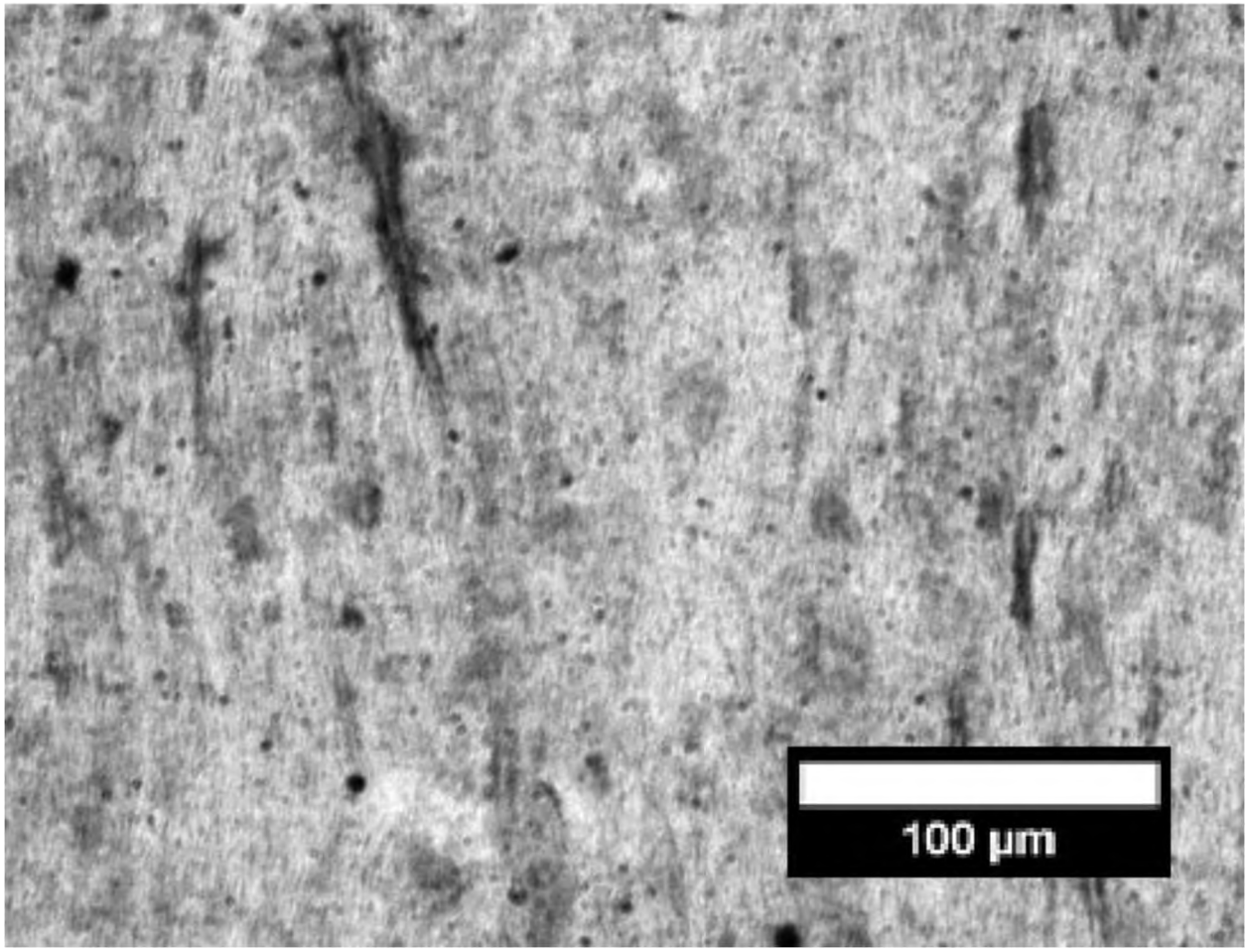

Figure 78.

35 cm^2:

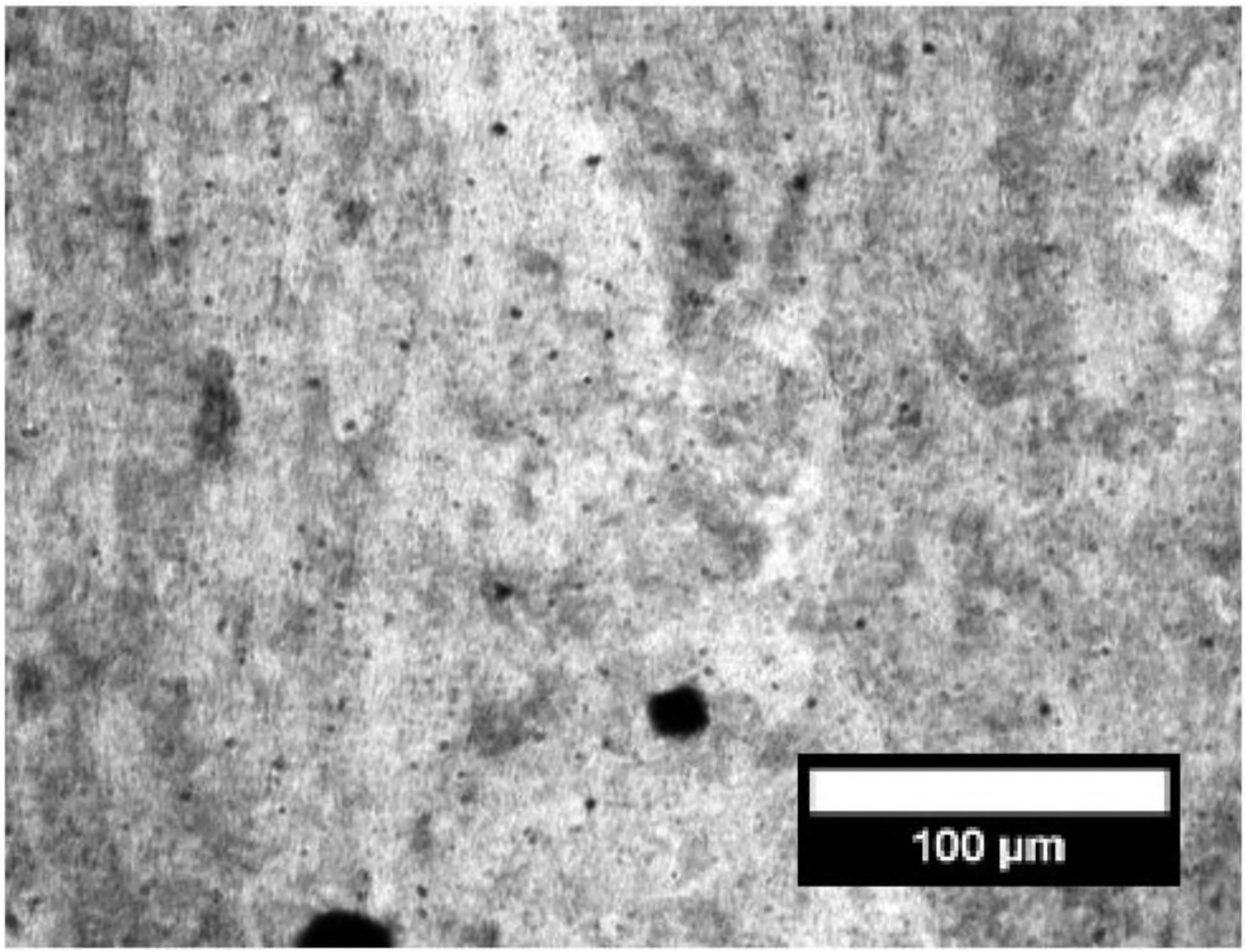

Figure 79.

30 cm^2:

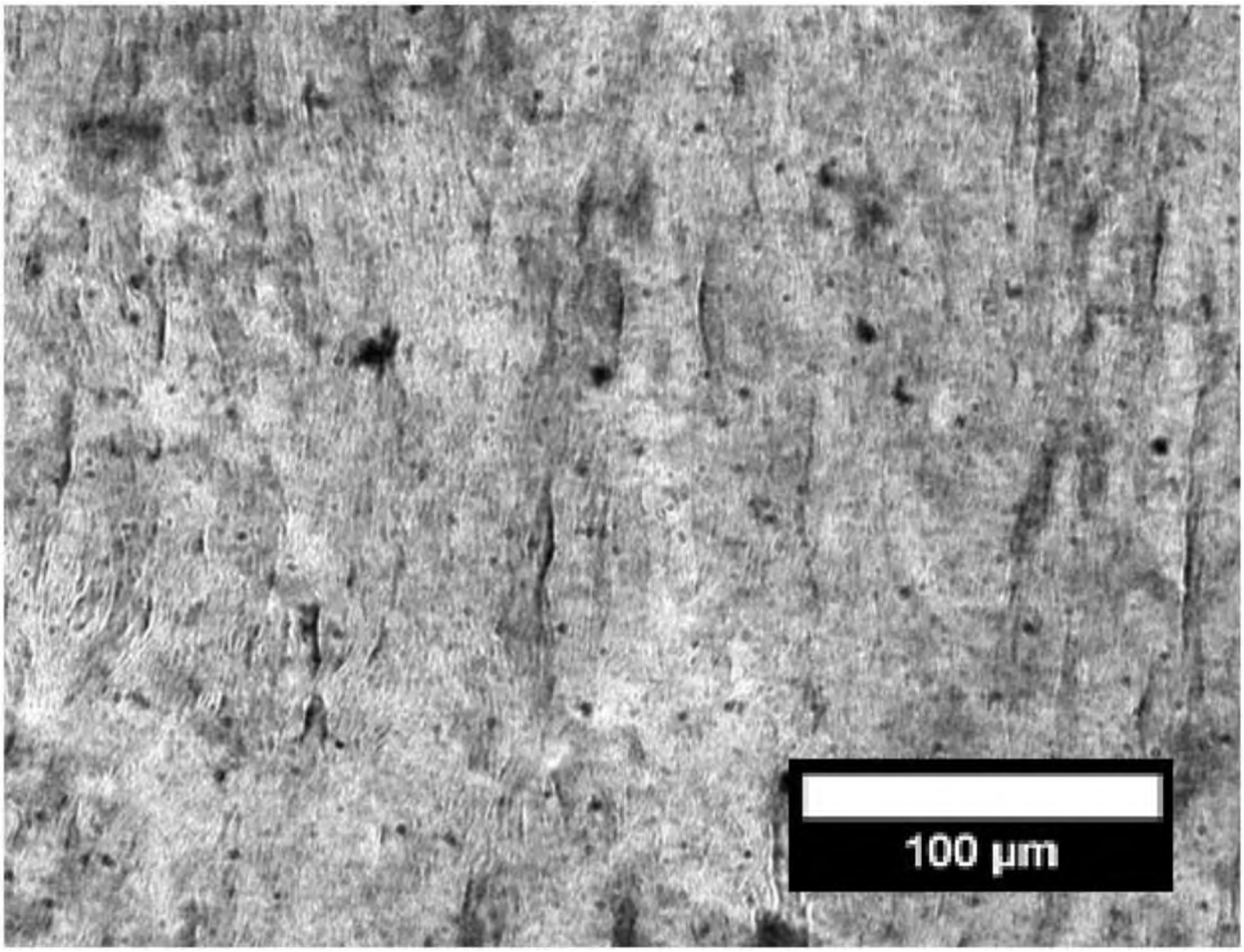

Figure 80.

25 cm^2:

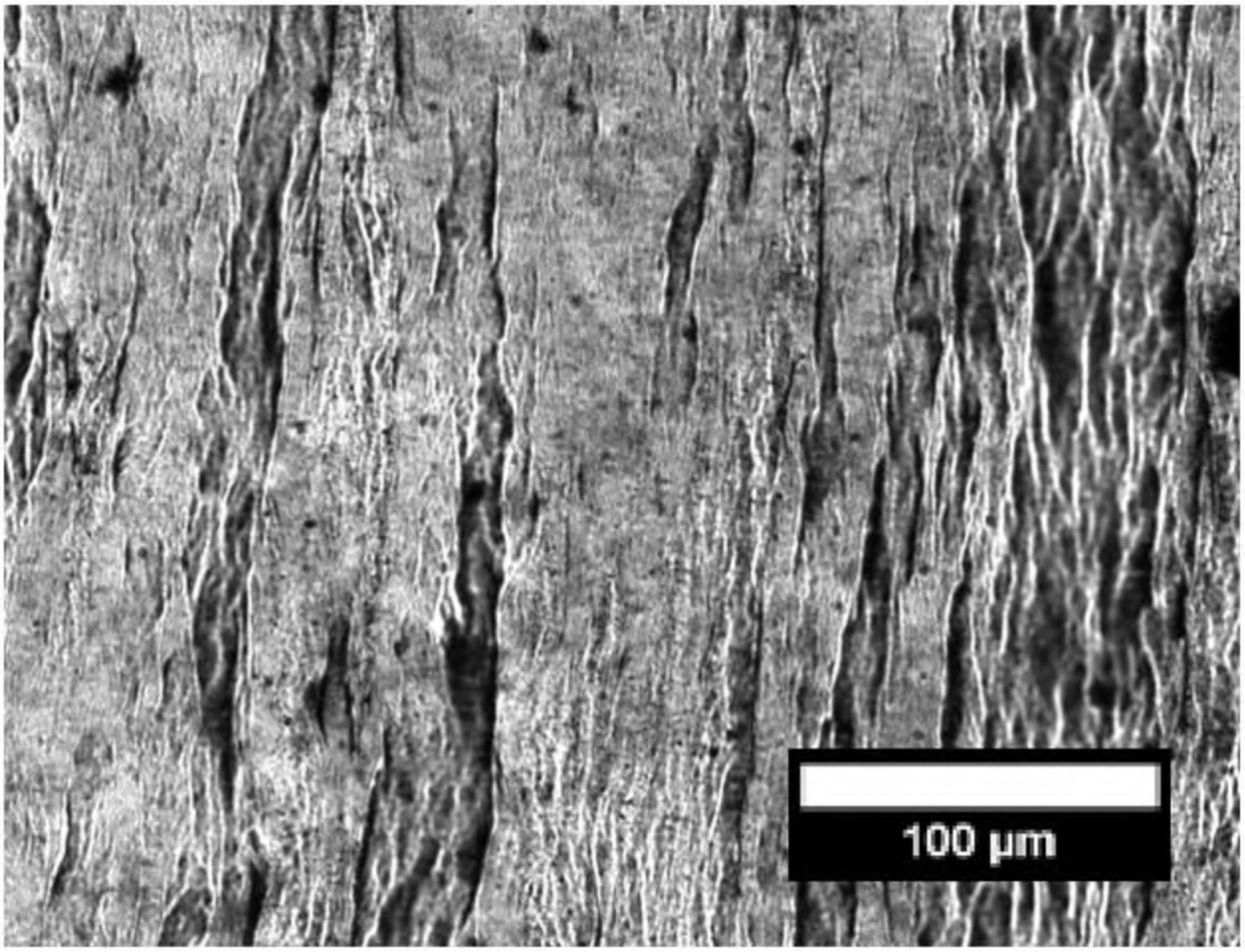

Figure 81.

6-hour modification:

40 cm^2:

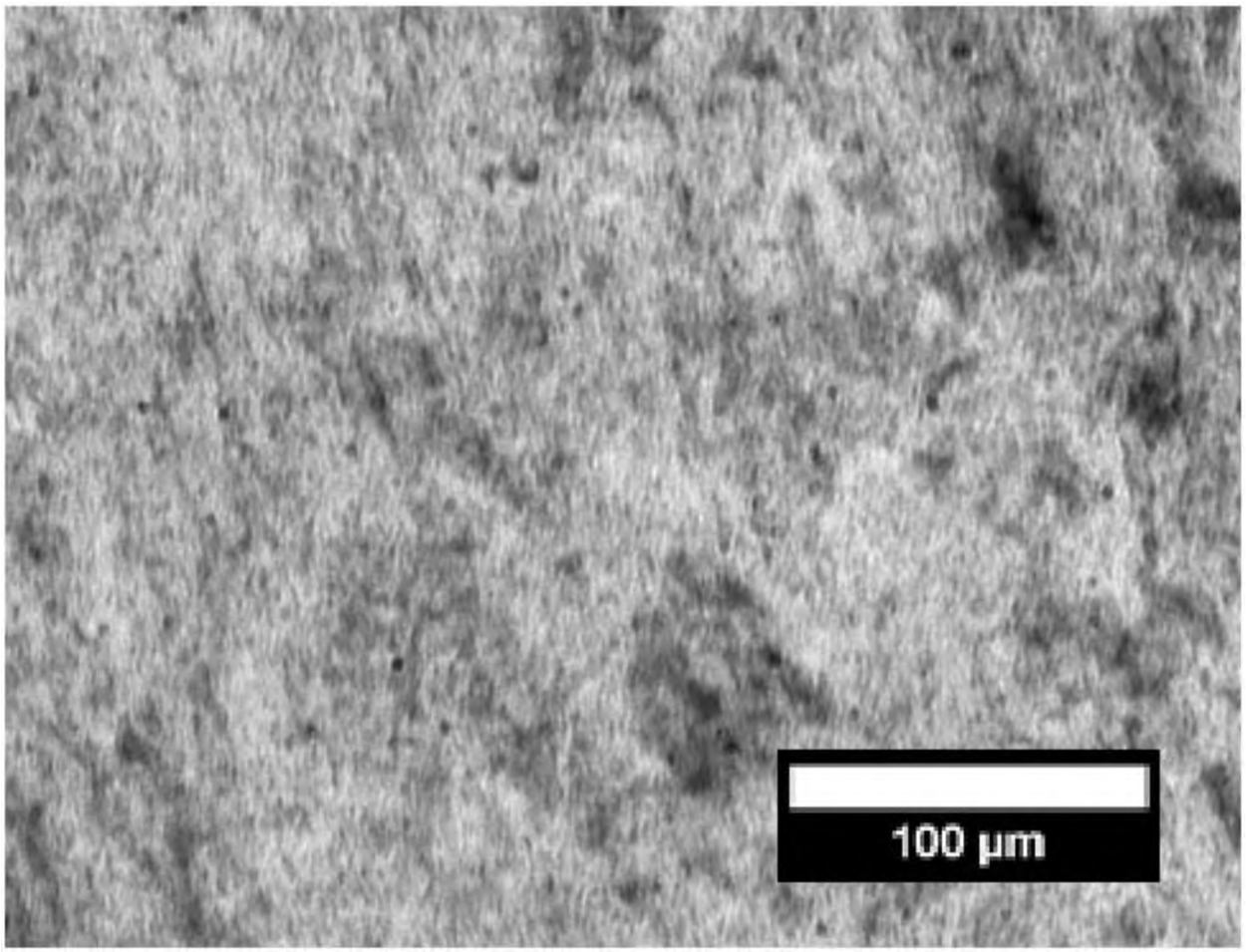

Figure 82.

35 cm^2:

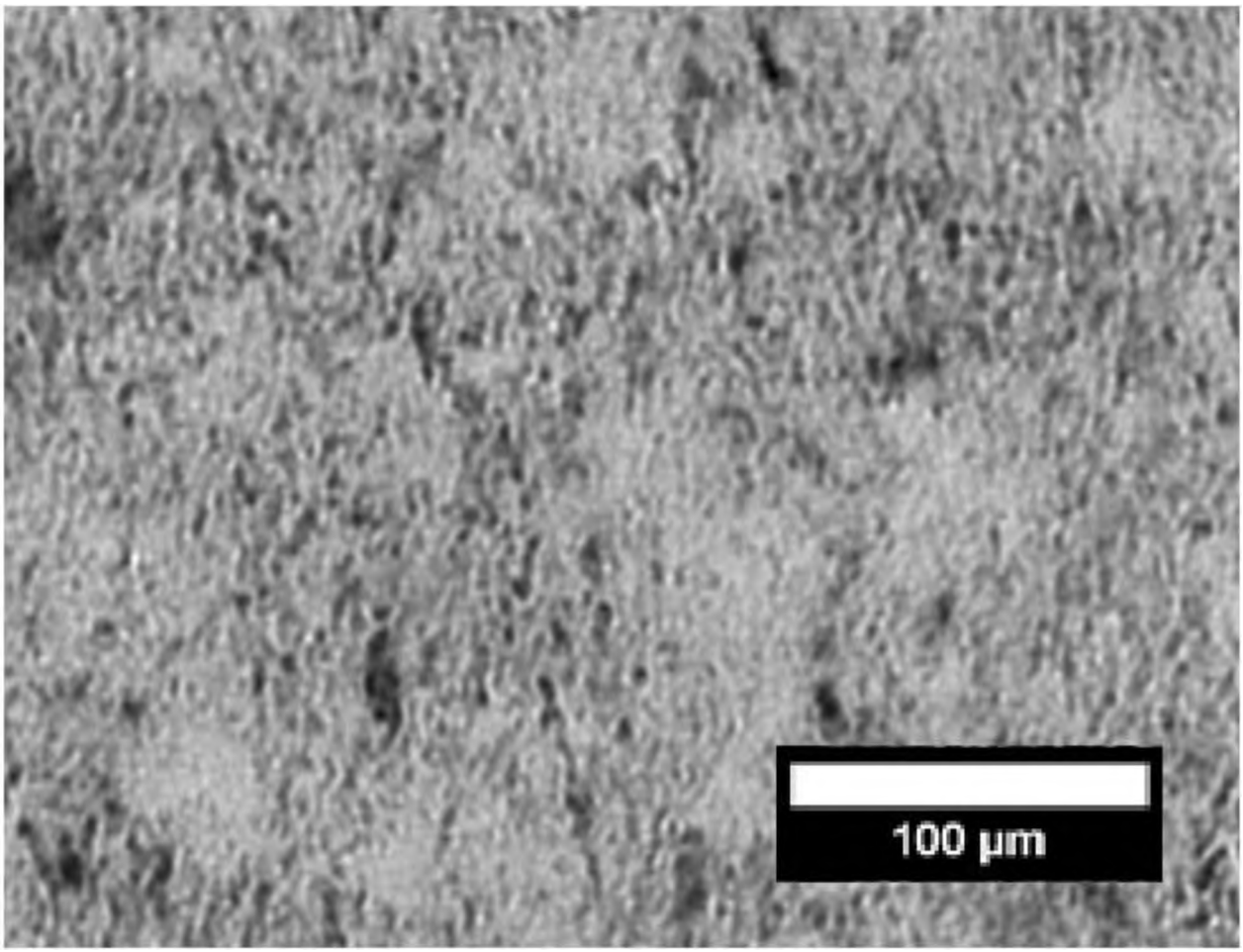

Figure 83.

30 cm^2:

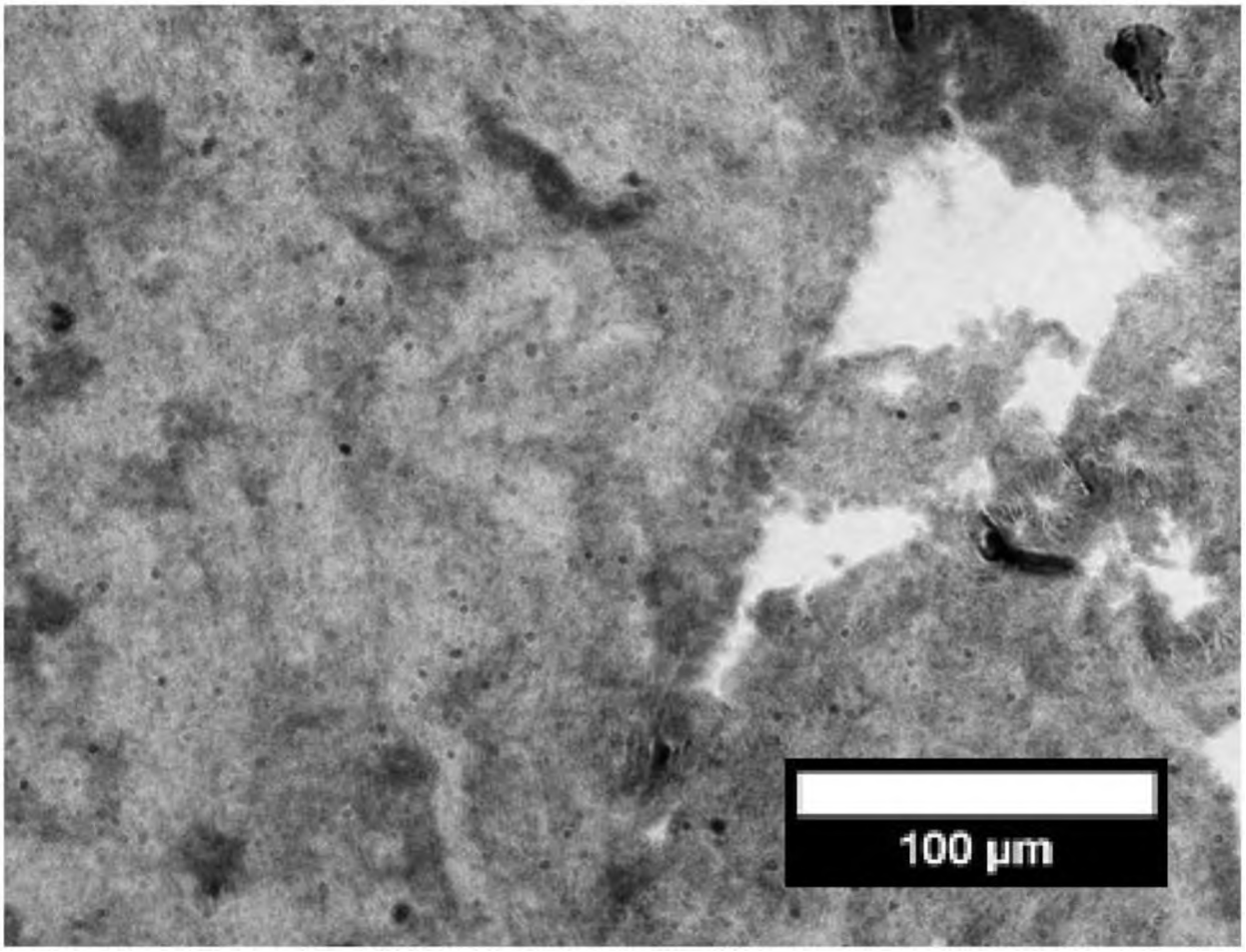

Figure 84.

25 cm^2:

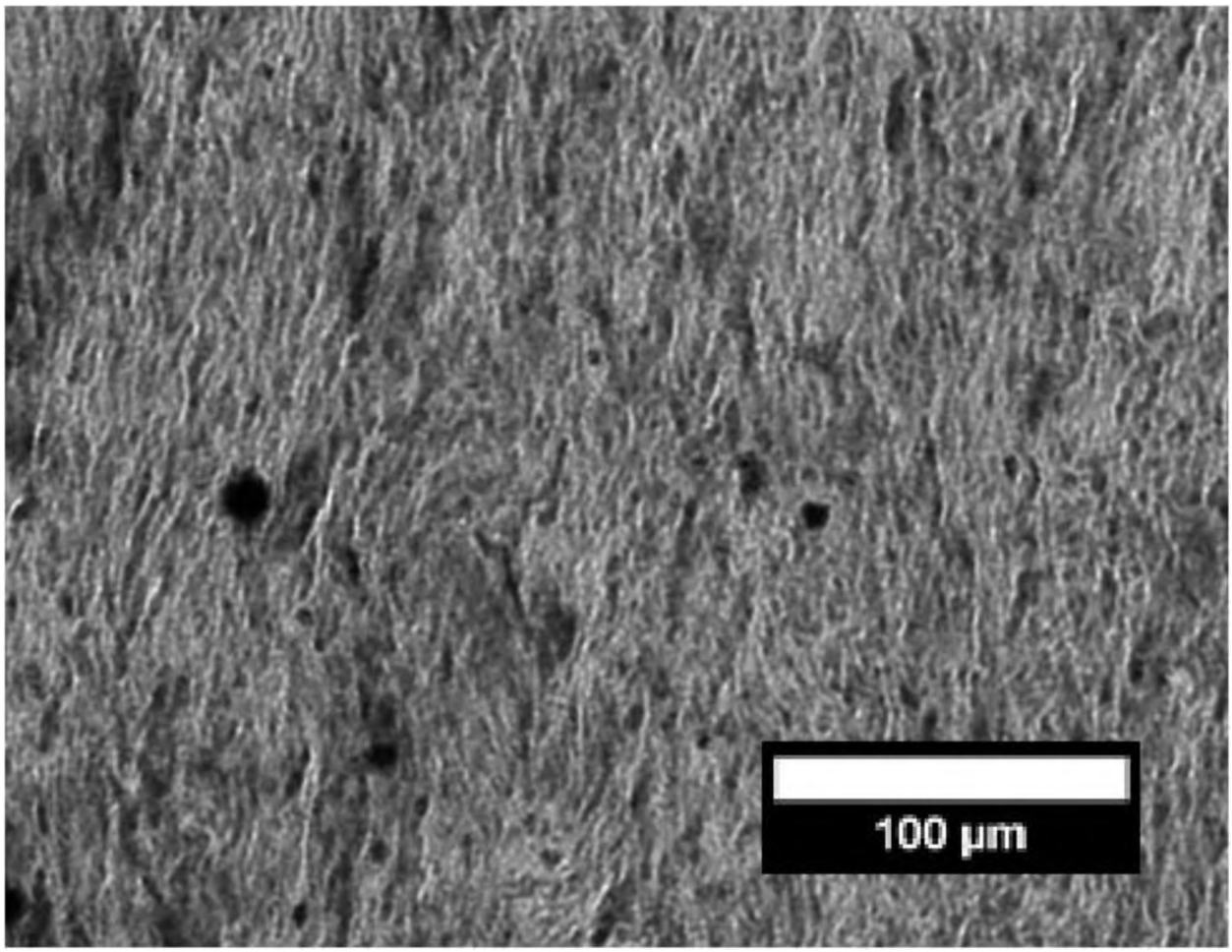

Figure 85.

APPENDIX E.

(SEM Images)

Unmodified:

40 cm^2:

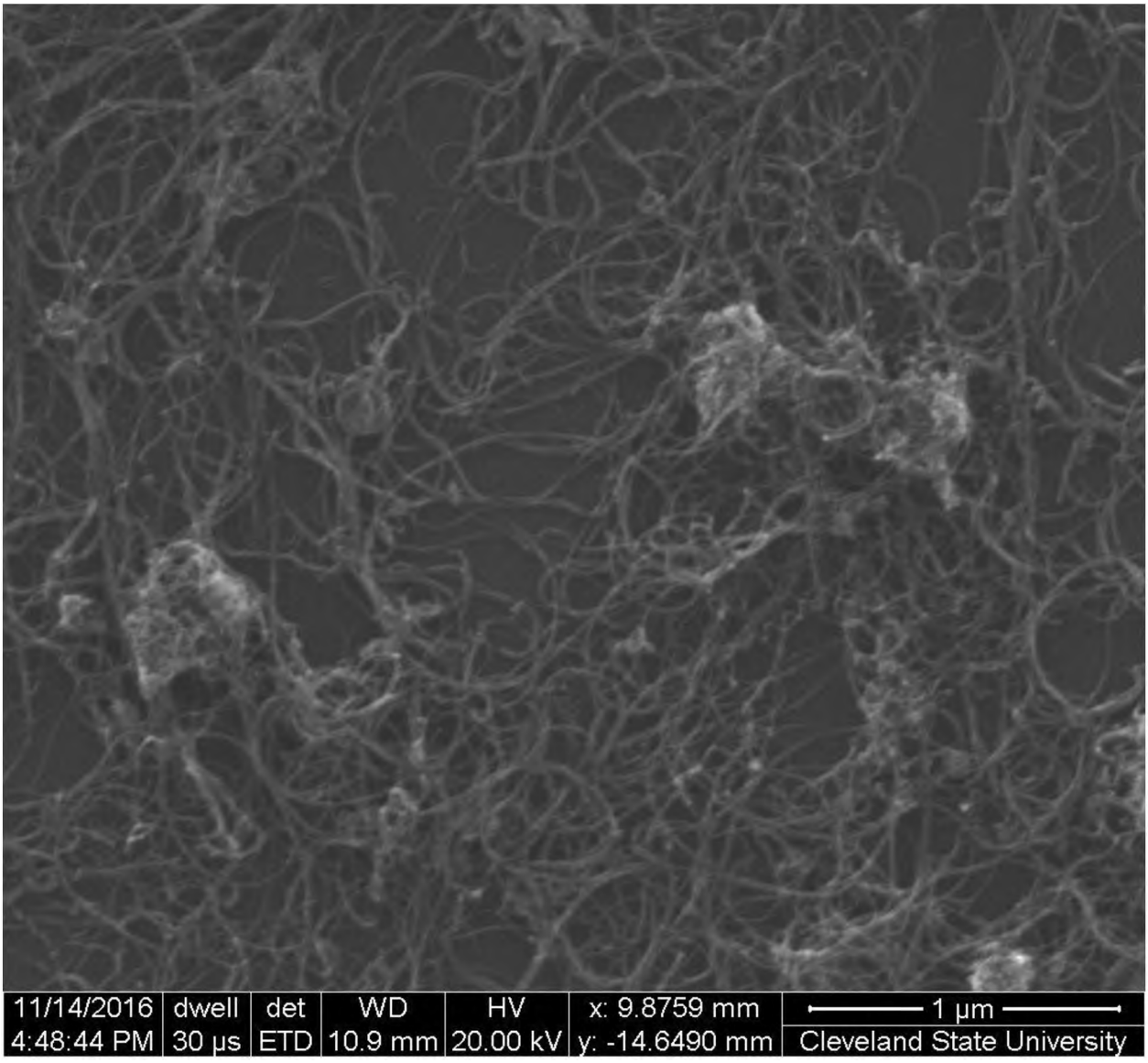

Figure 86.

25 cm^2:

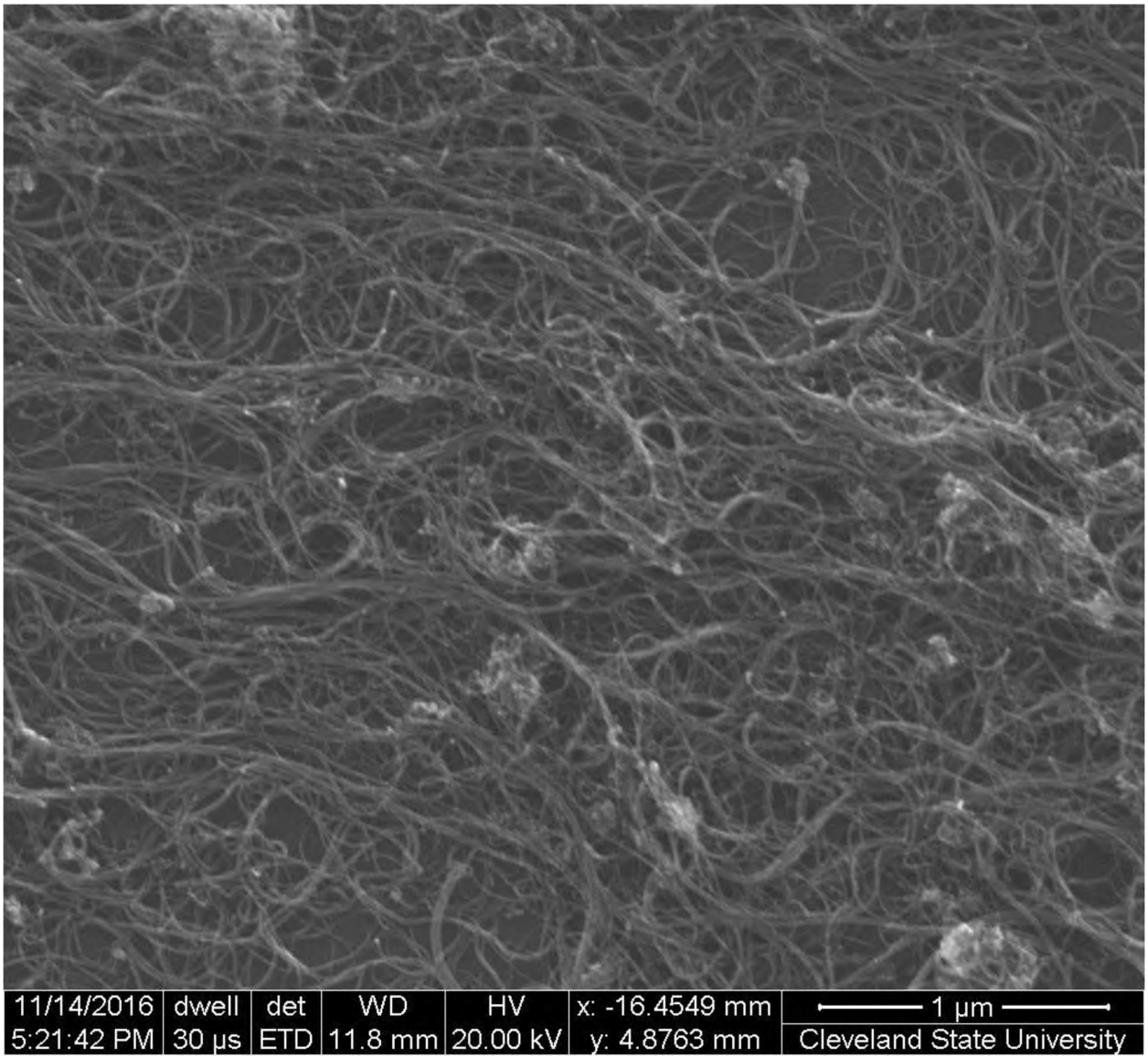

Figure 87.

40-minute modification:

35 cm^2:

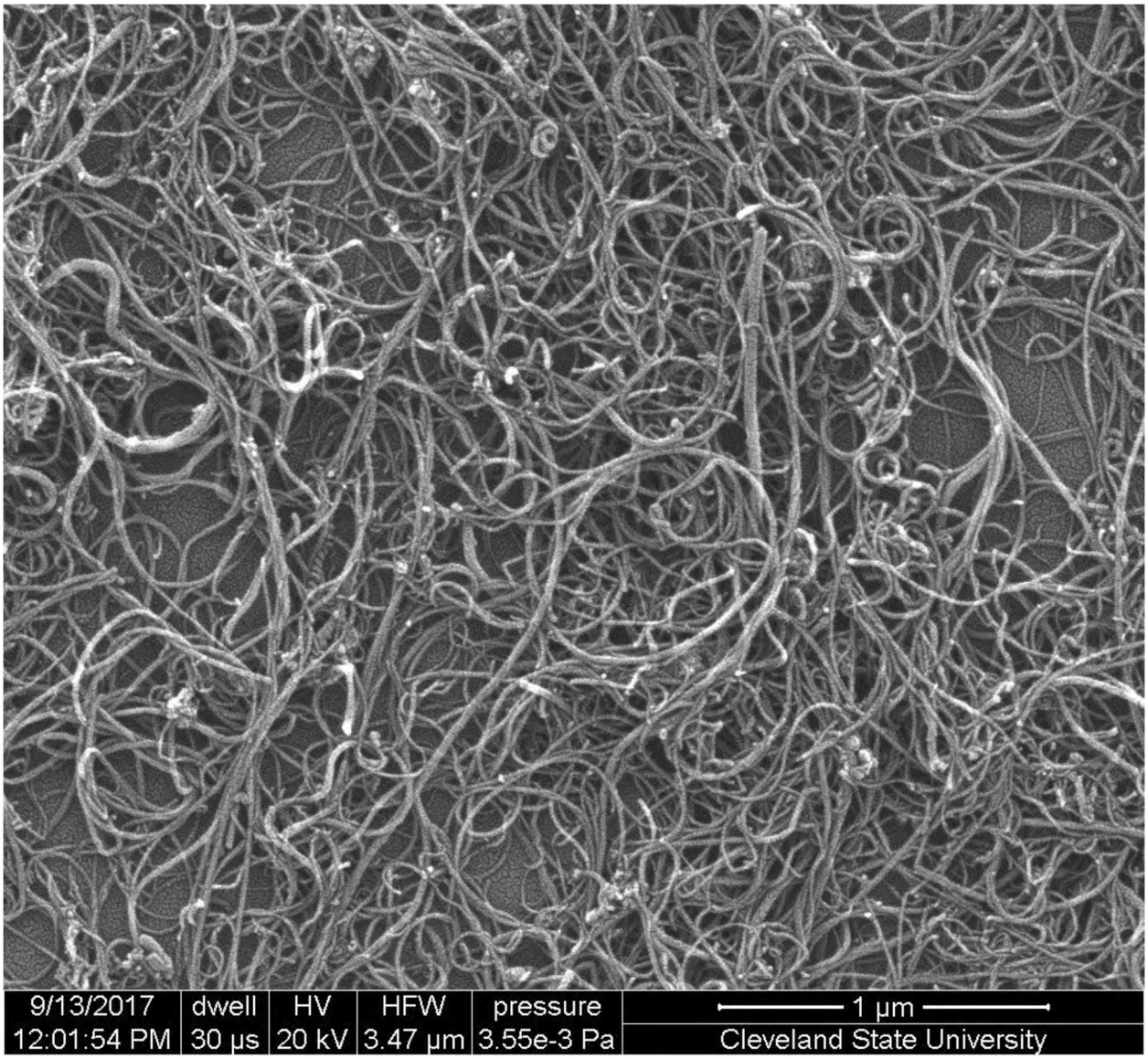

Figure 88.

25 cm^2:

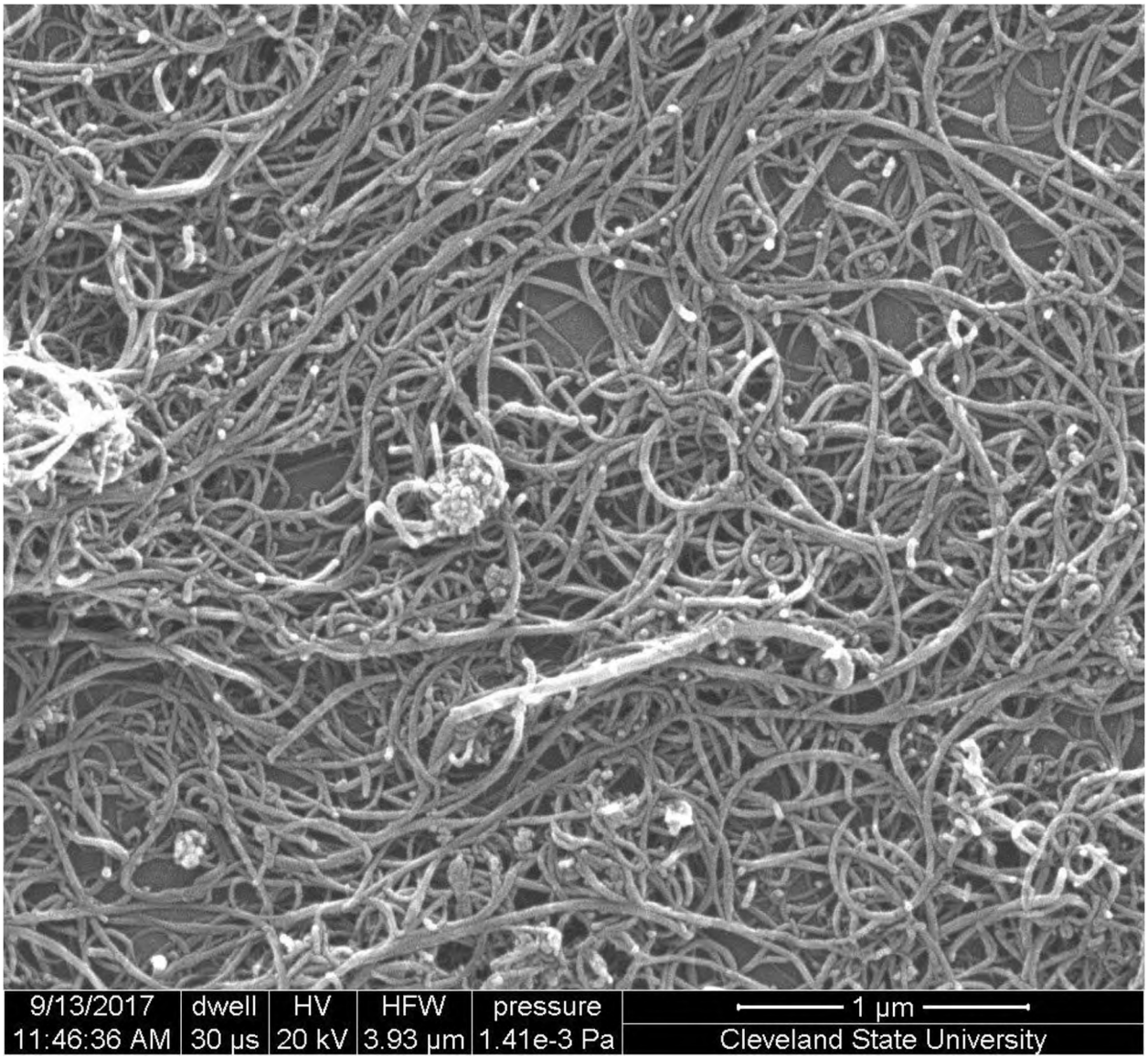

Figure 89.

1-hour modification:

35 cm^2:

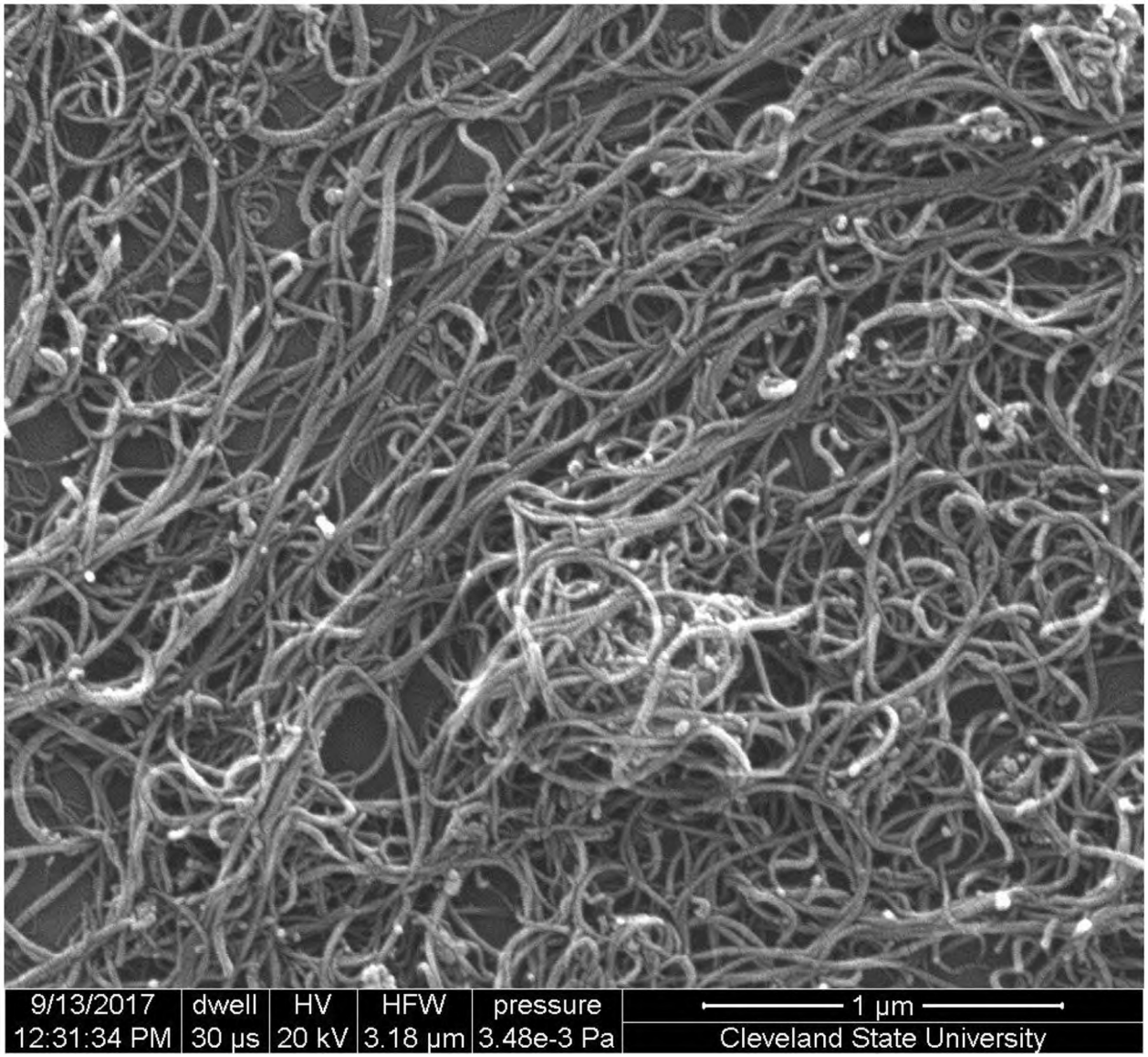

Figure 90.

25 cm^2:

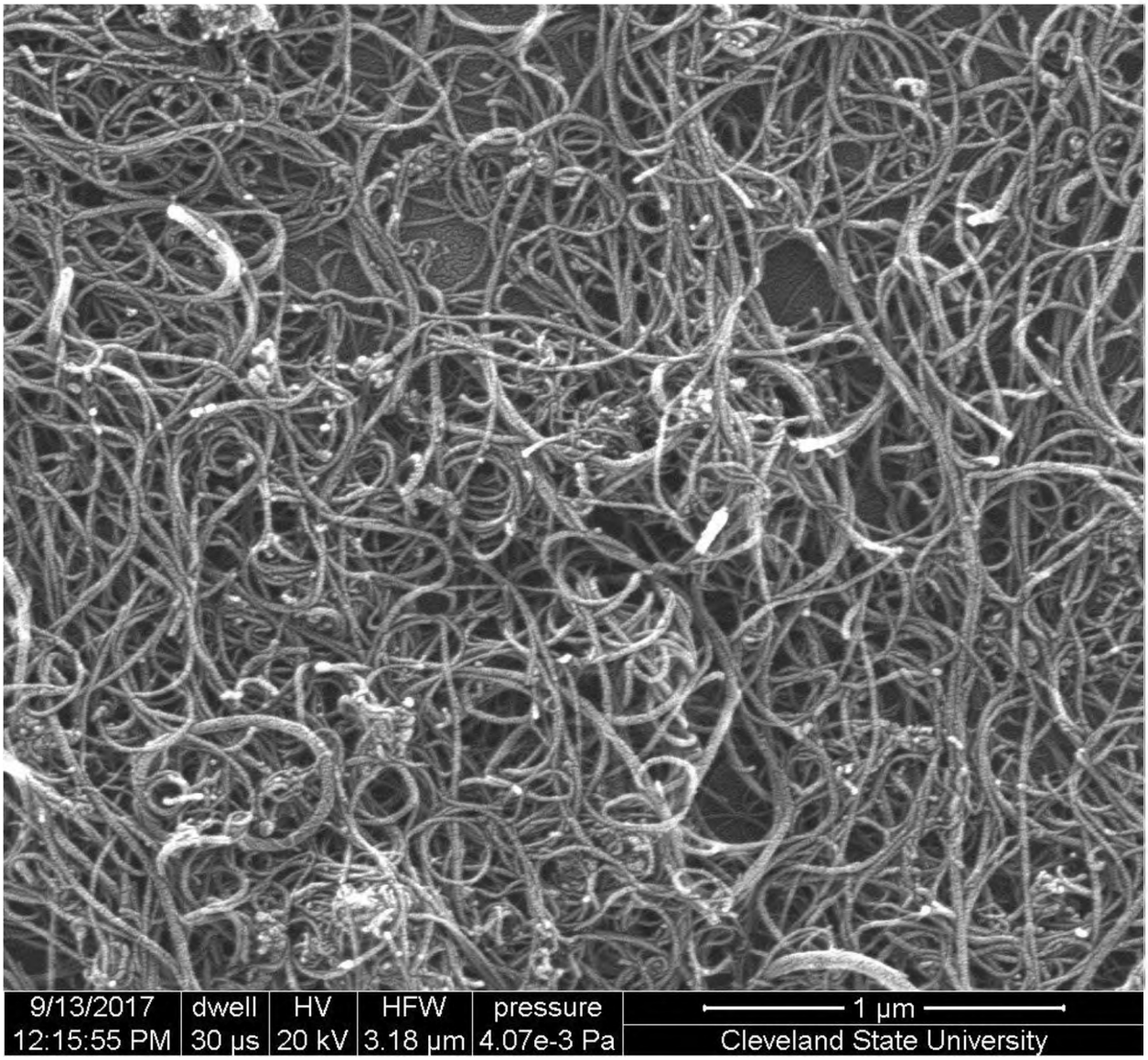

Figure 91.

2-hour modification:

35 cm^2:

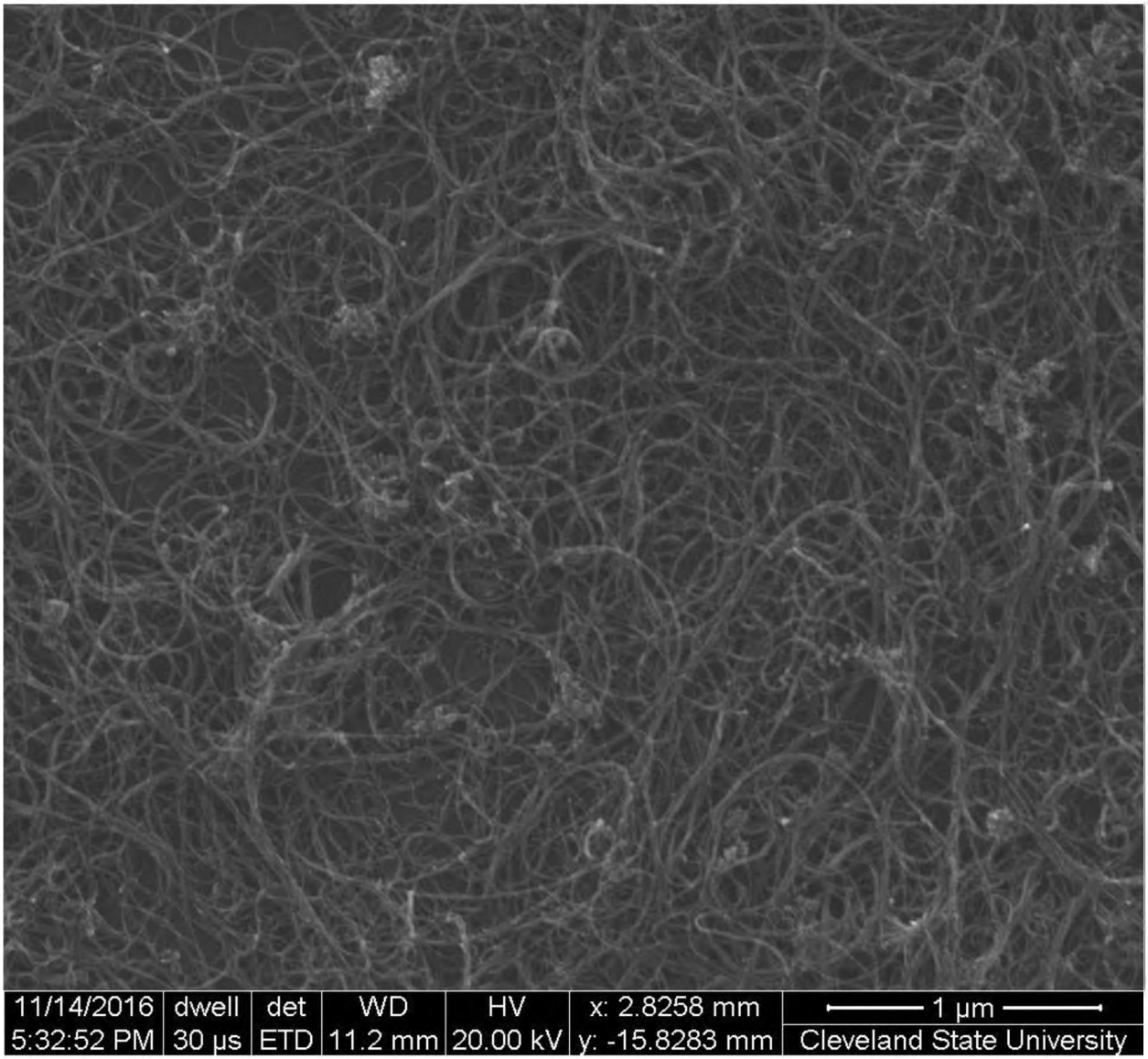

Figure 92.

25 cm^2:

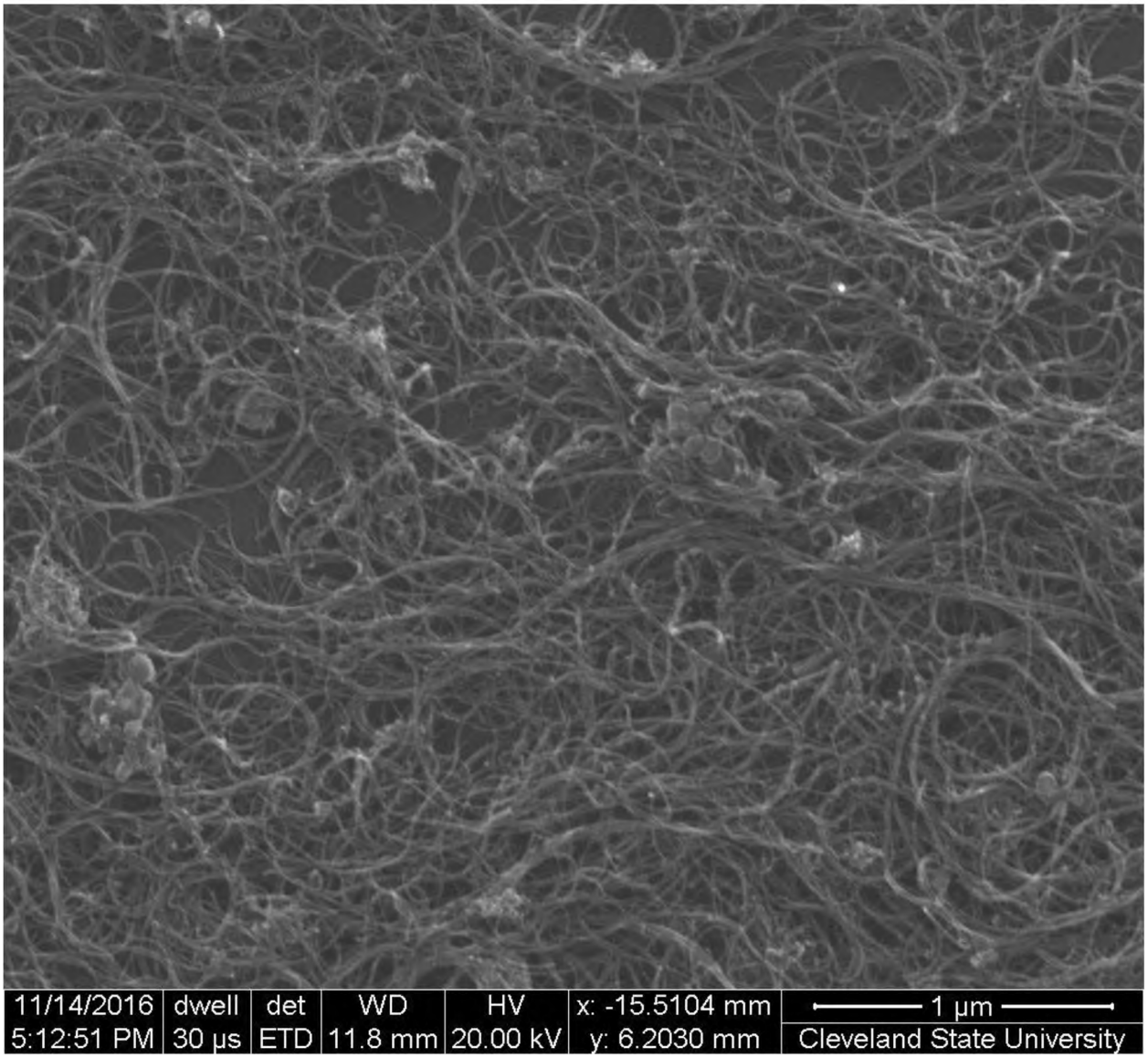

Figure 93.

4-hour modification:

35 cm^2:

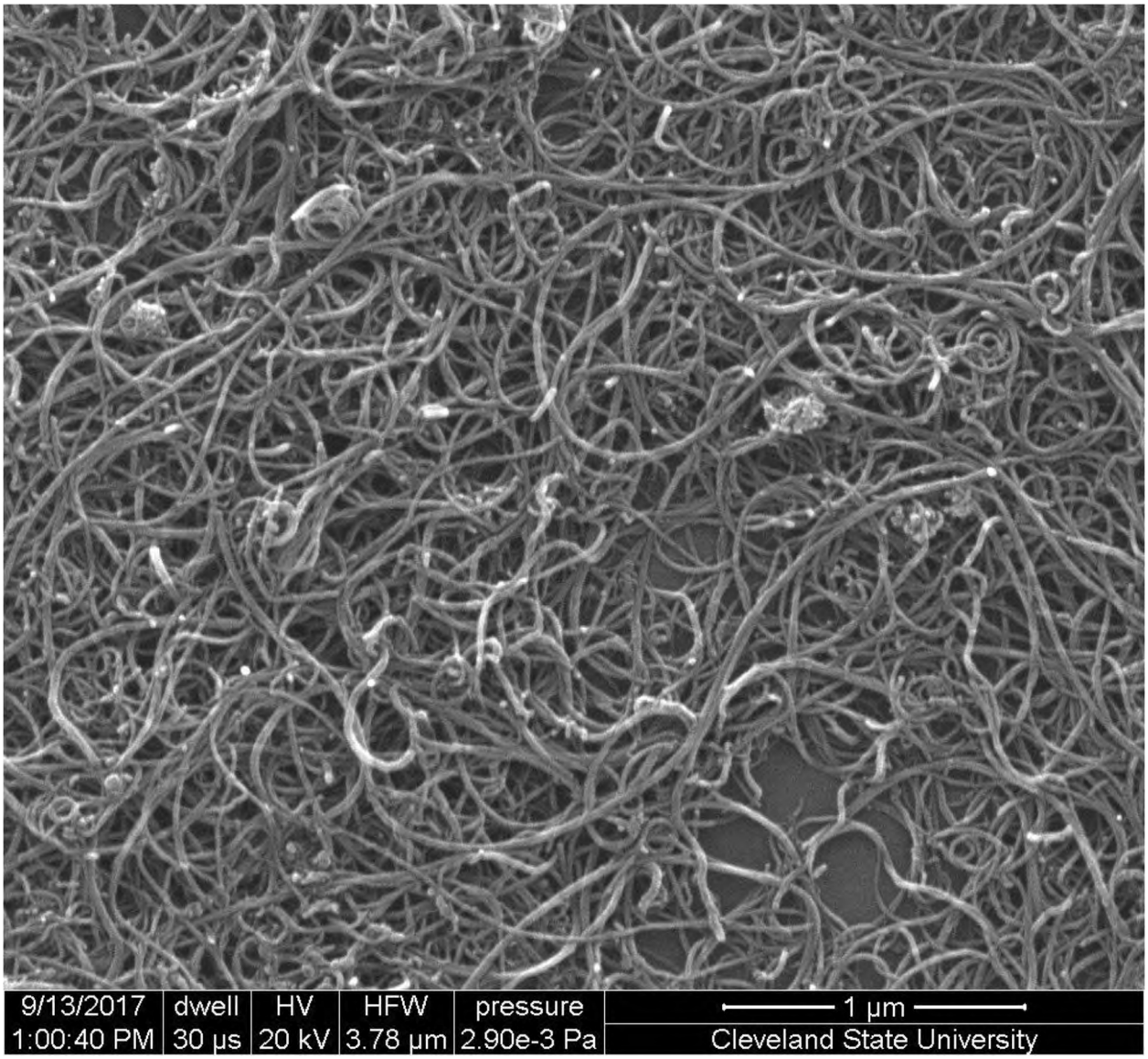

Figure 94.

25 cm^2:

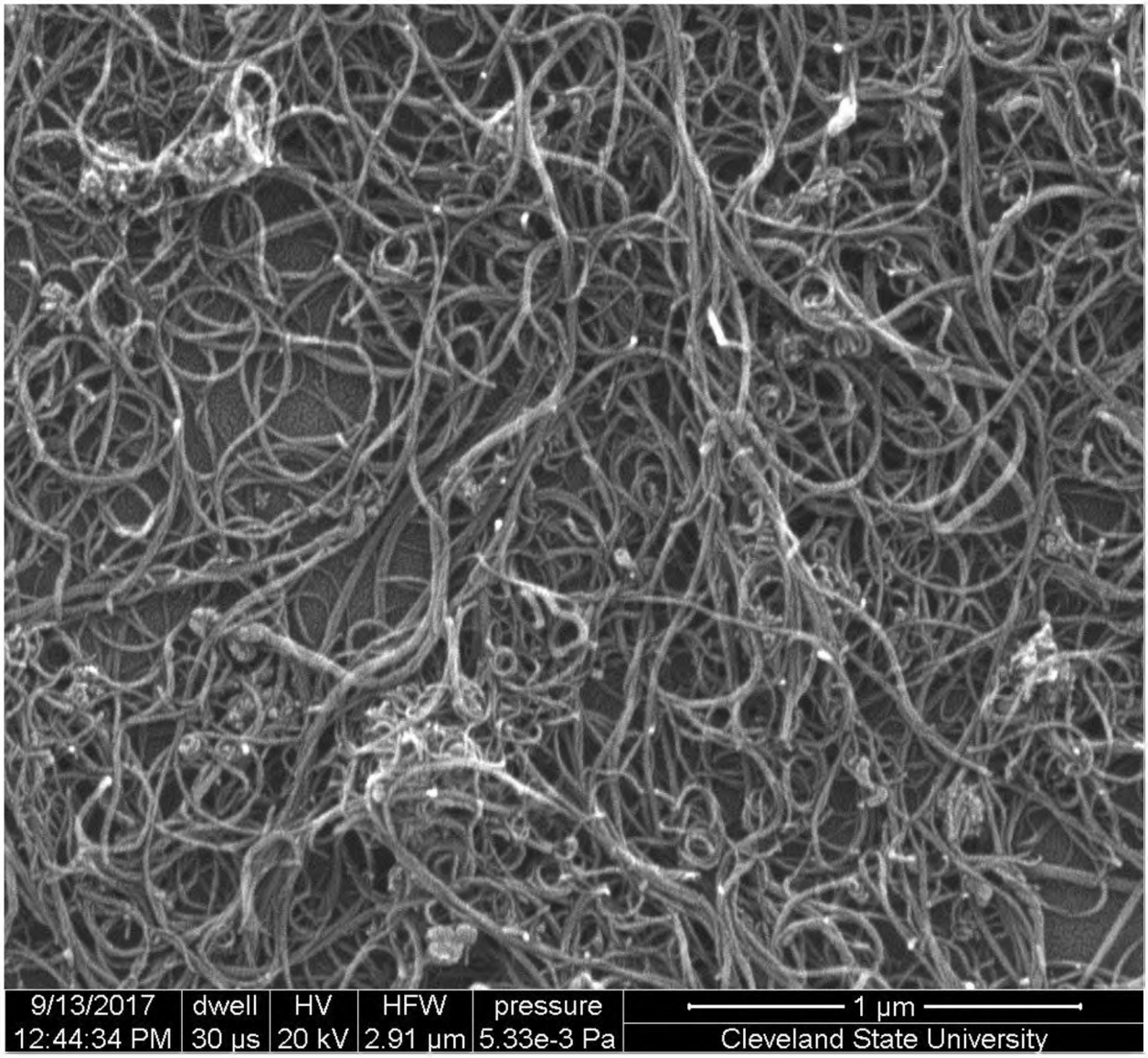

Figure 95.

6-hour modification:

35 cm^2:

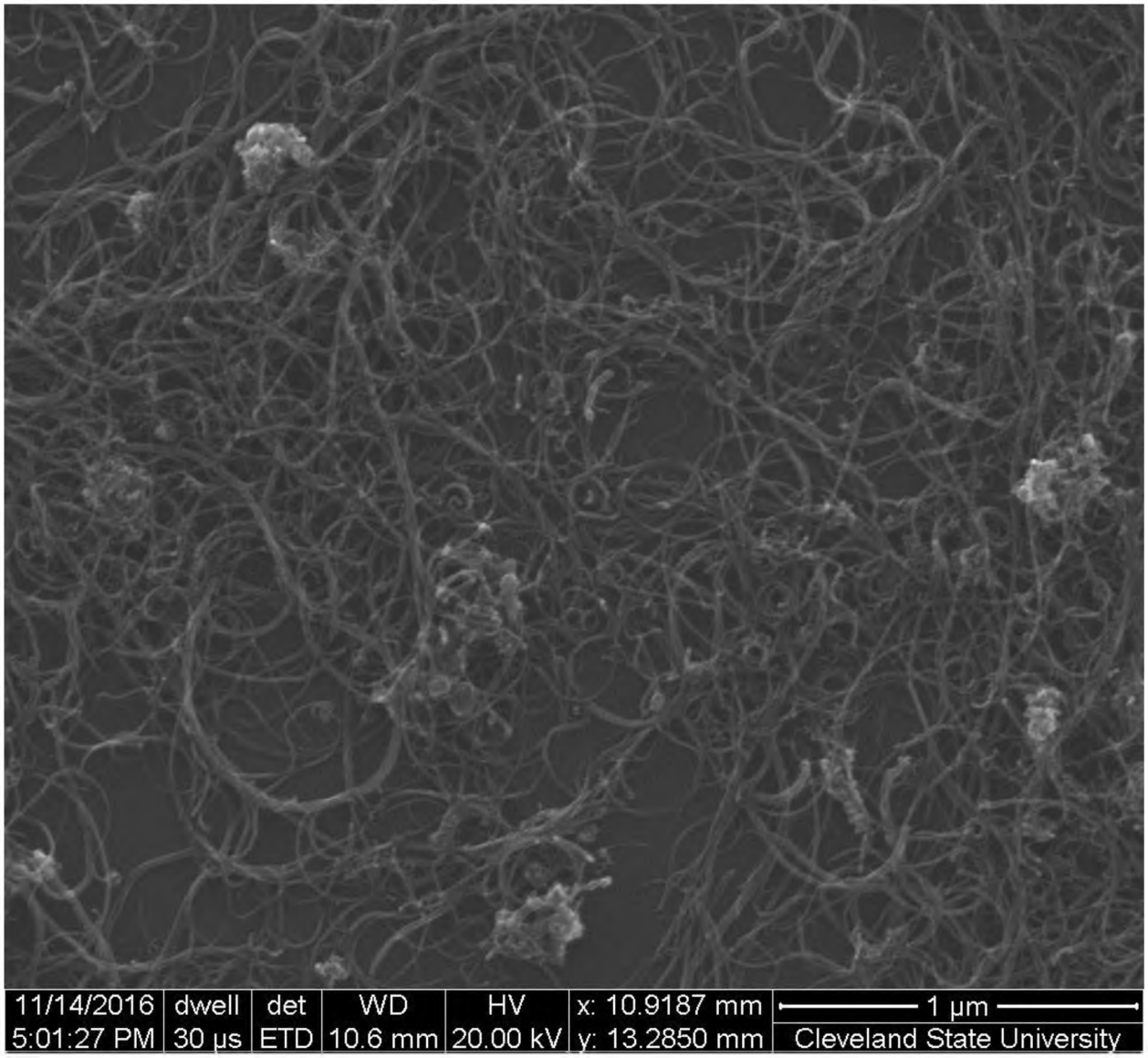

Figure 96.

25 cm^2:

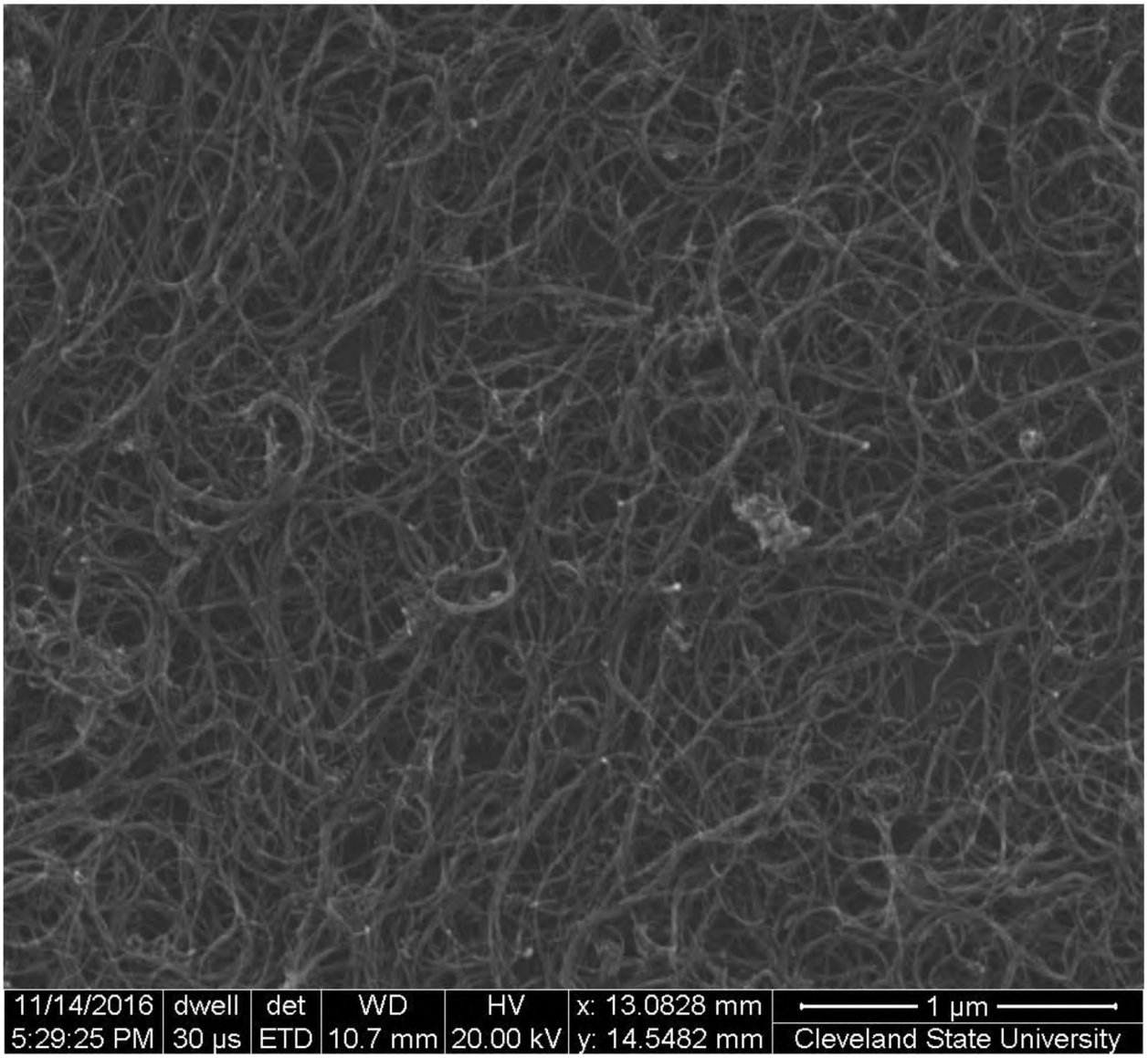
11/14/2016
5:29:25 PM
dwell
30 µs
det
ETD
WD
10.7 mm
HV
20.00 kV
x: 13.0828 mm
y: 14.5482 mm
1 µm
Cleveland State University

Figure 97.

APPENDIX F.

(Step Compressions)

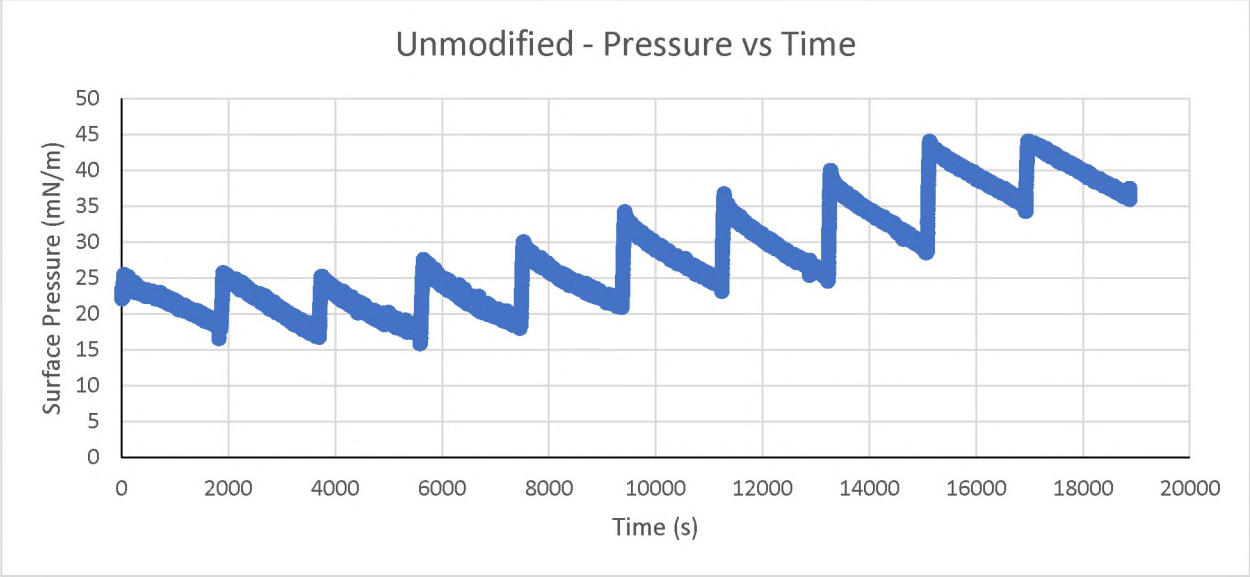

Figure 98.

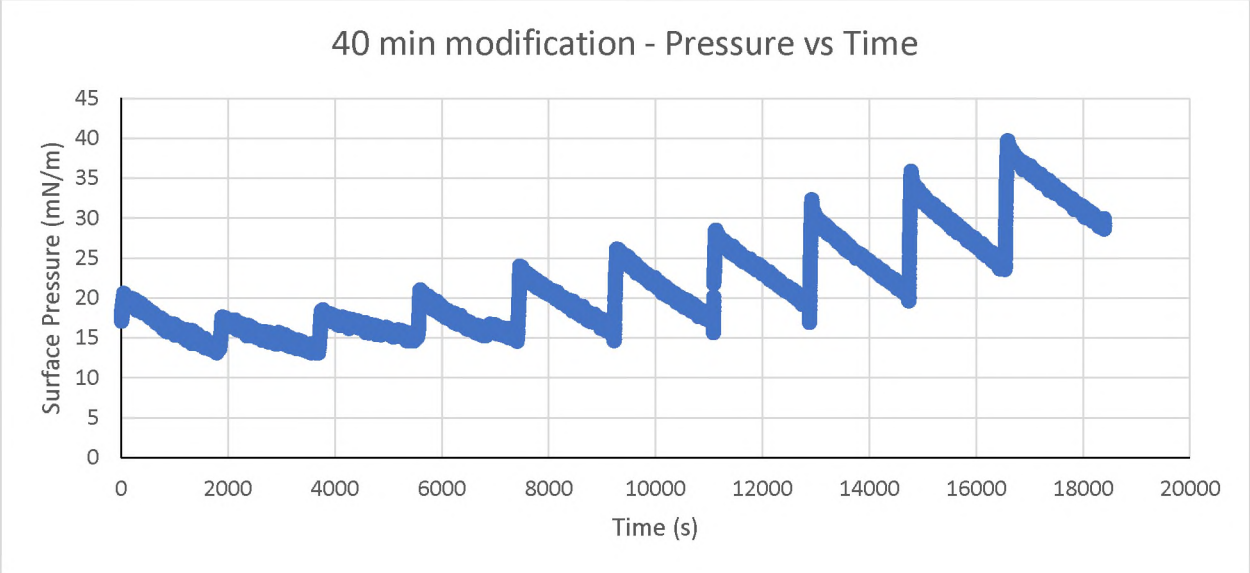

Figure 99.

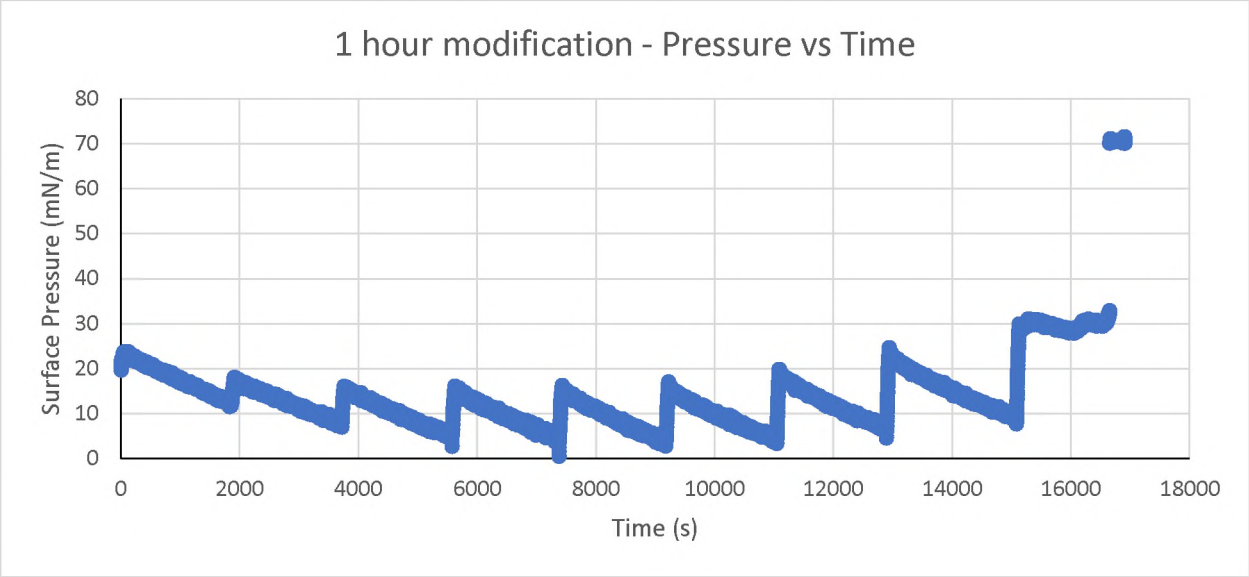

Figure 100.

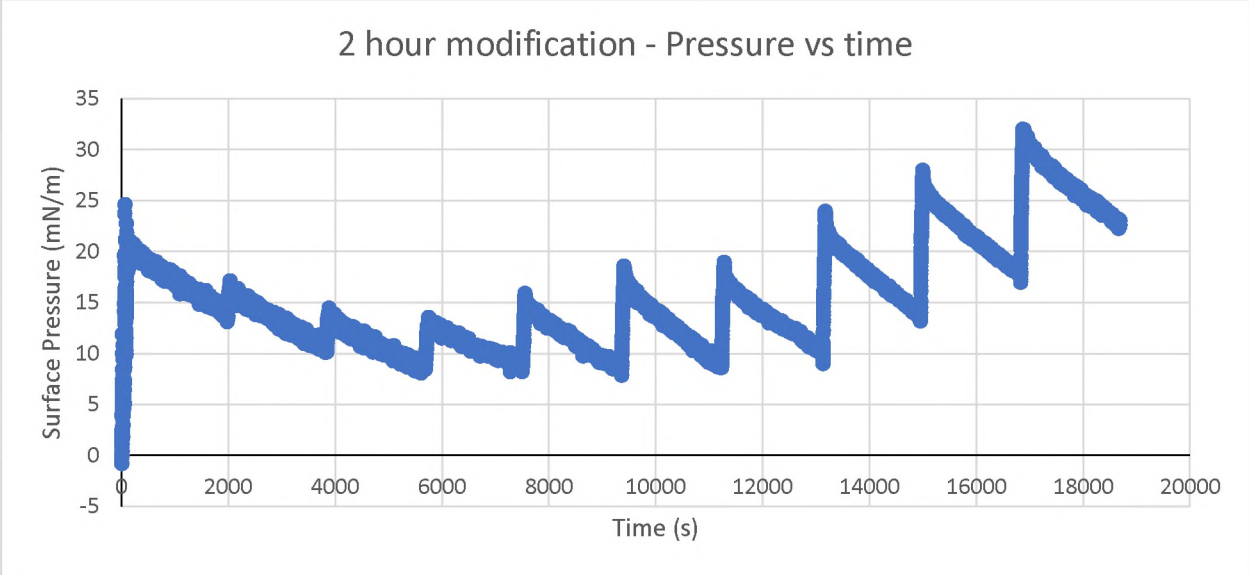

Figure 101.

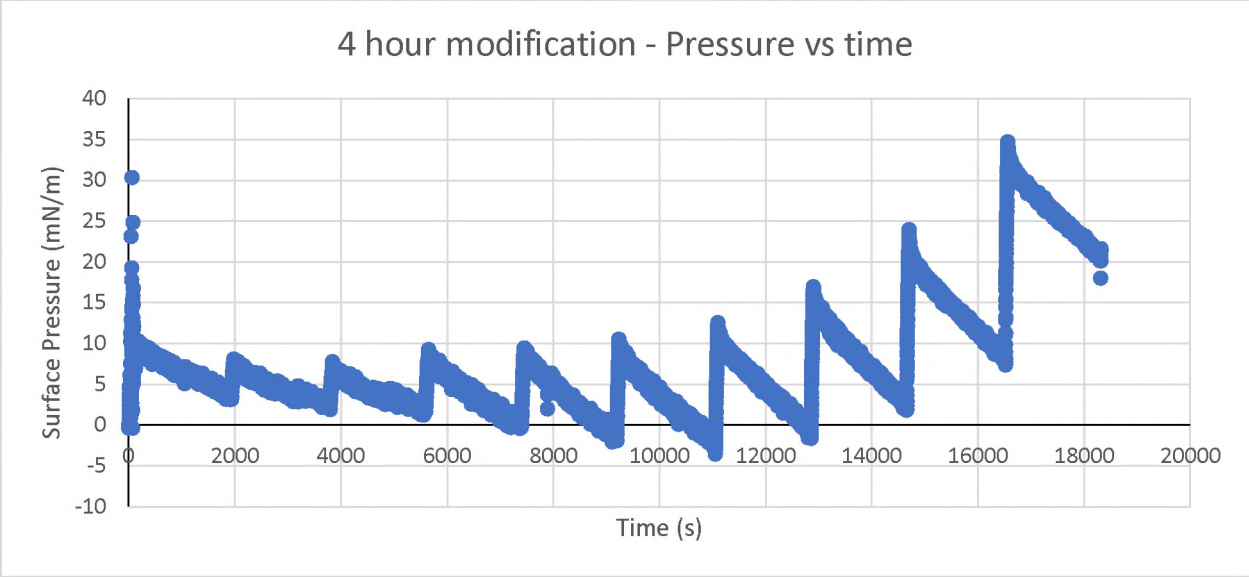

Figure 102.

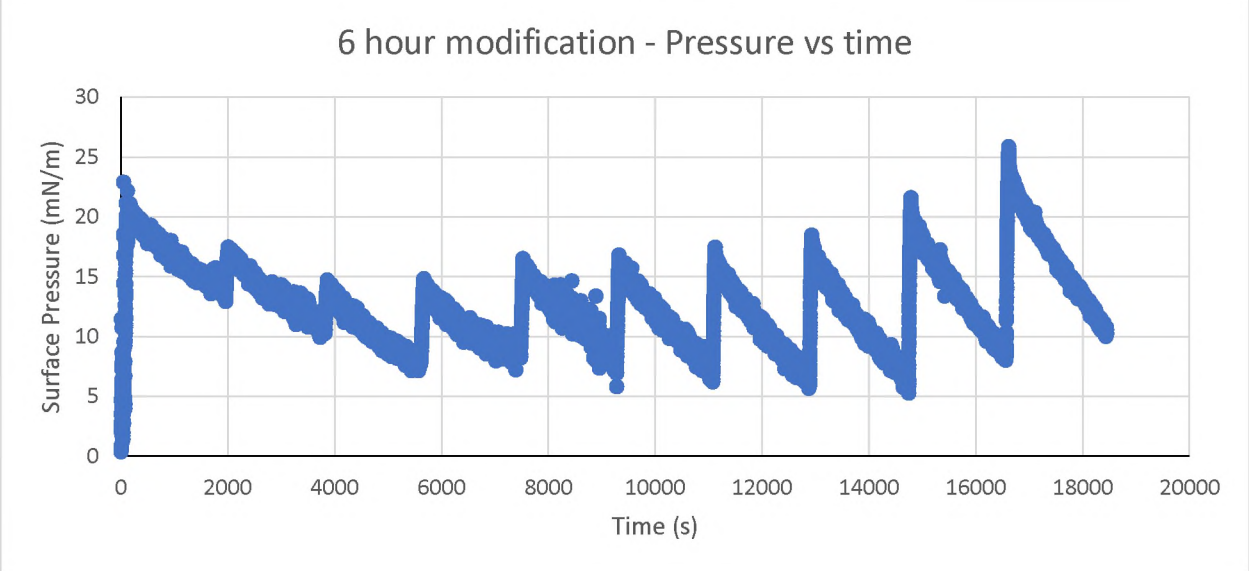

Figure 103.

APPENDIX G.

(Long relaxation durations)

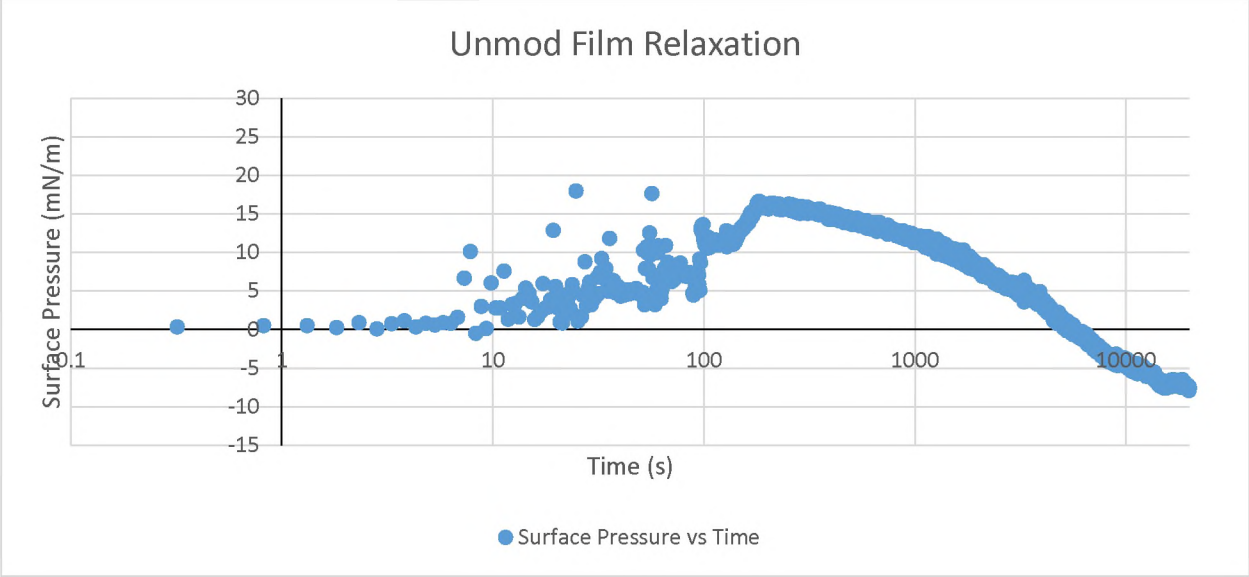

Figure 104.

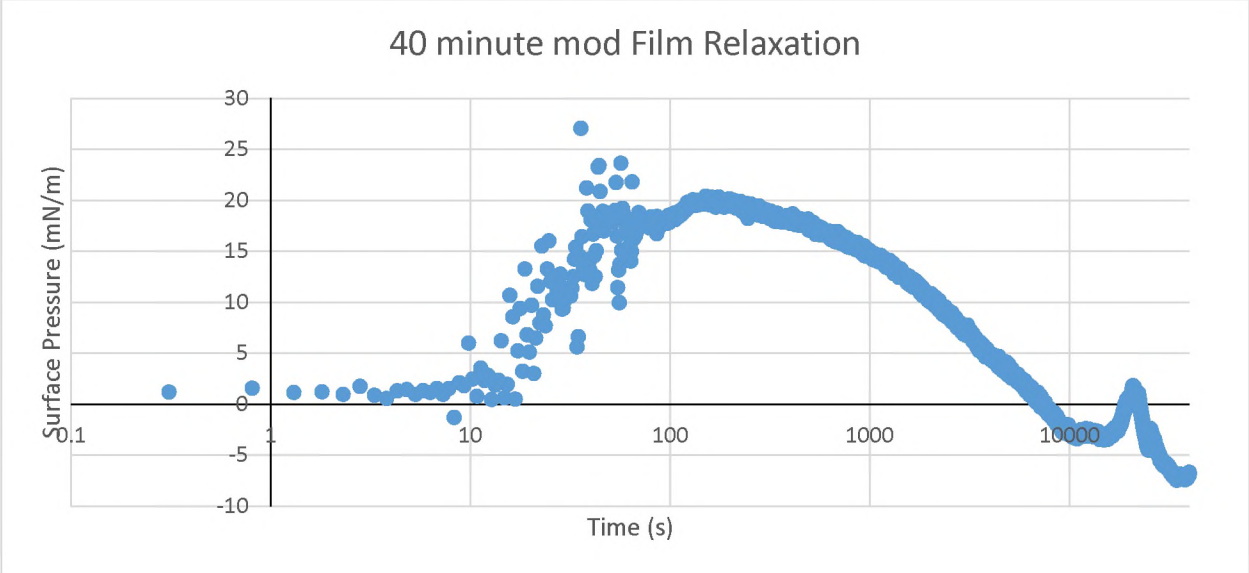

Figure 105.

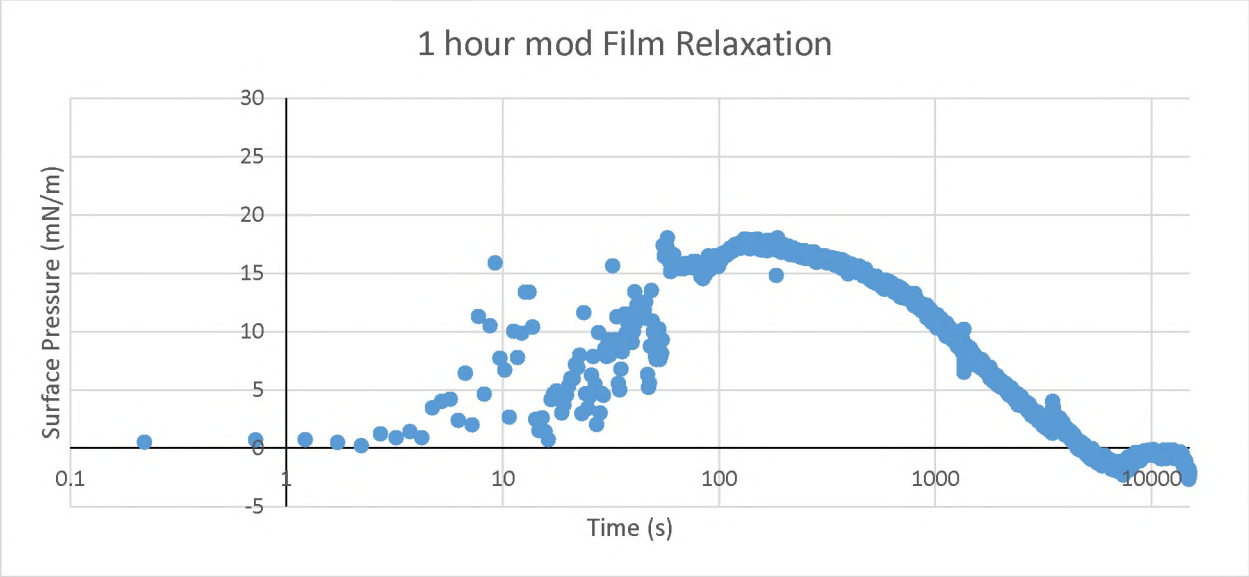

Figure 106.

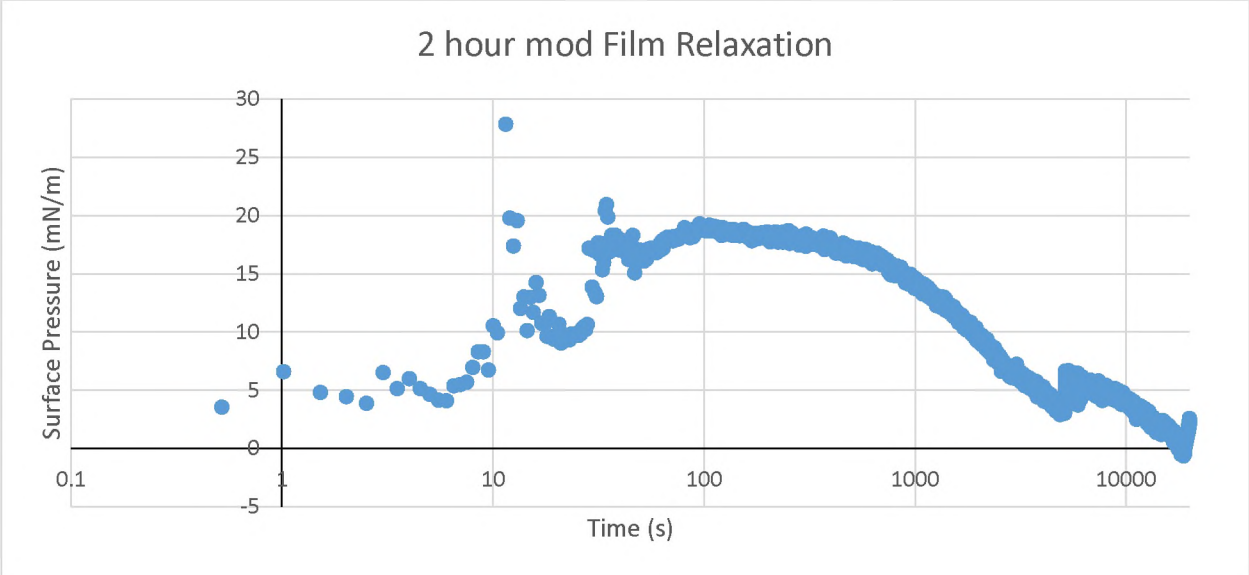

Figure 107.

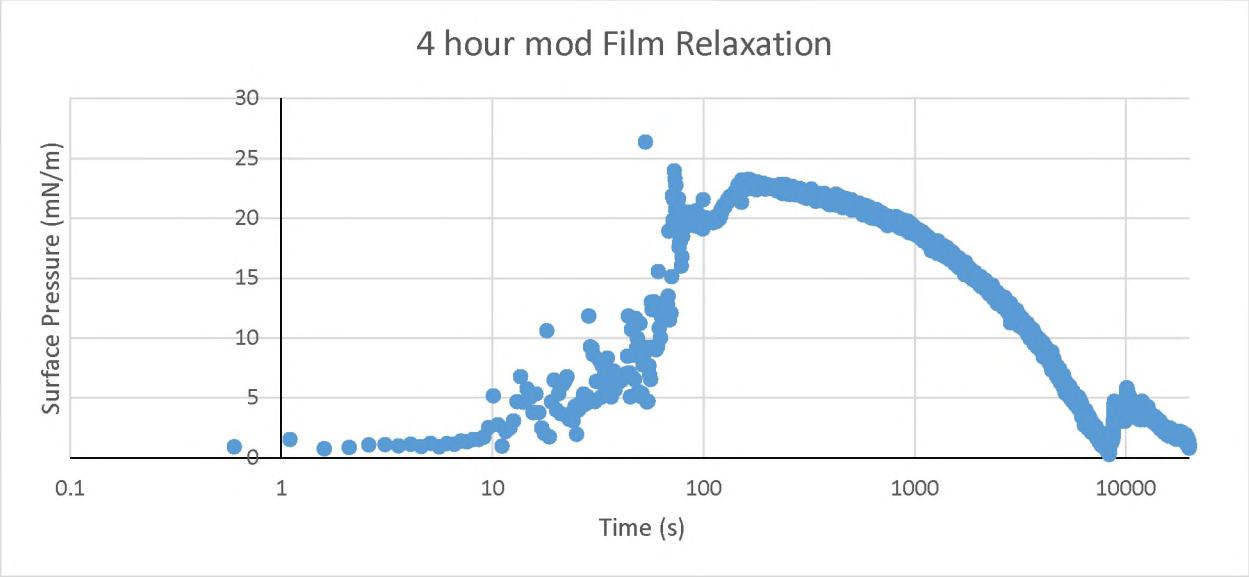

Figure 108.

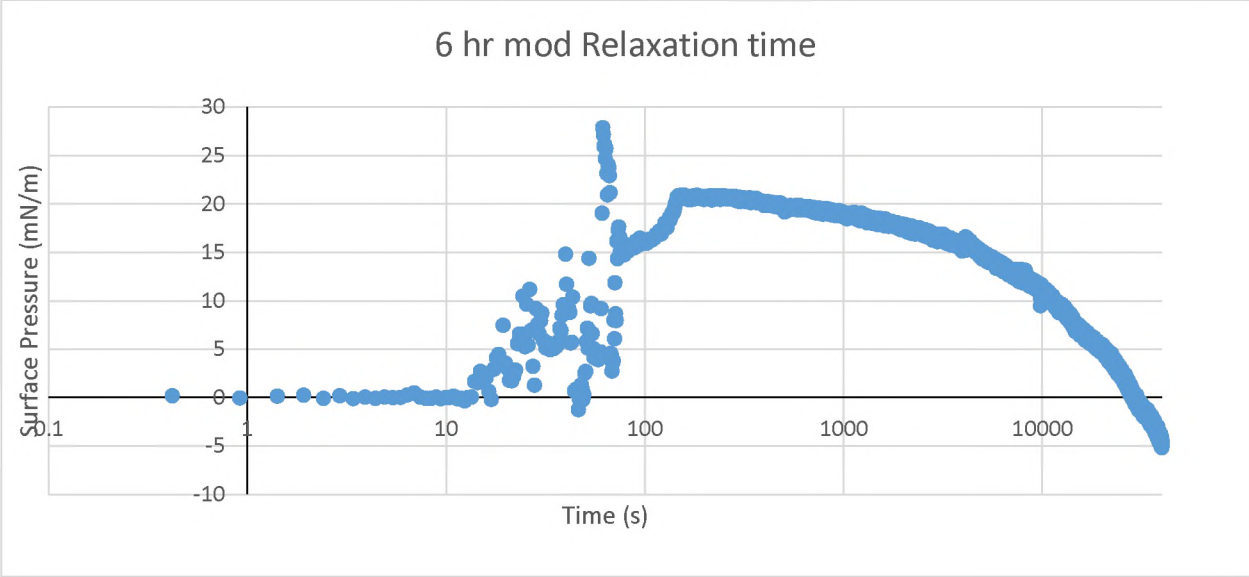

Figure 109.